SUPPORTING INFORMATION

This file includes:

1 Experimental 2

2 Crystallographic details 5

3 Syntheses of starting materials 13

4 Syntheses of biradicals 23

5 Irradiation experiments 36

6 CO_2 activation chemistry 55

7 Computational details 65

8 References 115

1 Experimental

General information. If not stated otherwise, all manipulations were carried out under oxygen- and moisture-free conditions in an inert argon atmosphere using standard Schlenk or drybox techniques. All glassware was heated three times *in vacuo* using a heat gun (650 °C) and cooled under argon atmosphere. Solvents were transferred using syringes, which were purged three times with argon prior to use. Solvents and reactants were either obtained from commercial sources or synthesized as detailed in Table S1.

Table S1. Origin and purification of solvents and reactants.

Substance	Origin	Purification
C_6H_6	local trade	dried over Na/benzophenone freshly distilled prior to use
C_6D_6	euriso-top	dried over Na freshly distilled prior to use
$Cp^*_2TiCl_2$	MCAT	used as received
$Cp^*_2ZrCl_2$	MCAT	used as received
NEt_3	Sigma Aldrich, >99%	dried over 4 Å molecular sieves, freshly distilled over Na prior to use
toluene	local trade	dried over Na/benzophenone freshly distilled prior to use
$[P(\mu\text{-NTer})]_2$	synthesized	re-crystallized as described in the literature[1]
sodium-4-isocyano-3,5-dimethylephenolate	synthesized	re-crystallized as described in the literature[2]

NMR spectra were recorded on Bruker spectrometers (AVANCE 250, AVANCE 300 or AVANCE 500) or on JEOL spectrometers (ECZL 400) and were referenced internally to the deuterated solvent (^{13}C: C_6D_6 δ_{ref} = 128.4 ppm, THF-d_8 $\delta_{ref,1}$ = 25.4 ppm, $\delta_{ref,2}$ = 67.6 ppm), to protic impurities in the deuterated solvent (^{1}H: C_6HD_5 δ_{ref} = 7.16 ppm, THF-d_7 $\delta_{ref,1}$ = 1.73 ppm, $\delta_{ref,2}$ = 3.58 ppm) or externally (^{31}P: 85% H_3PO_4 δ_{ref} = 0 ppm). All measurements were carried out at ambient temperature unless

denoted otherwise. NMR signals were assigned using experimental data (e.g., chemical shifts, coupling constants, integrals where applicable) in conjunction with computed NMR data (GIAO method, *cf*. Computational details). The signs of $^{n}J(^{31}P,^{31}P)$ coupling constants were derived from calculated values.

For NMR spectra simulation, the calculated and experimental ^{31}P NMR spectra were transferred to gNMR.[3] The full lineshape iteration procedure of gNMR was applied to match the calculated spectrum to the experimental spectrum.

IR spectra of crystalline samples were recorded on a Bruker Alpha II FT-IR spectrometer equipped with an ATR unit at ambient temperature under an argon atmosphere. Relative intensities are reported according to the following intervals: very weak (vw, 0–10%), weak (w, 10–30%), medium (m, 30–60%), strong (s, 60–90%), very strong (vs, 90–100%).

Raman spectra of crystalline samples were recorded using a LabRAM HR 800 Horiba Jobin YVON Raman spectrometer equipped with an Olympus BX41 microscope with variable lenses. The samples were excited by a red laser (633 nm, 17 mW, air-cooled HeNe laser. All measurements were carried out at ambient temperature unless stated otherwise.

Elemental analyses were obtained using an Elementar vario Micro cube CHNS analyser.

Note: All generated biradicals could not be studied by EA due to their equilibrium chemistry, which always results in mixtures.

Mass spectra were recorded on a Thermo Electron MAT 95-XP sector field mass spectrometer using solid samples or an Advion Expression L benchtop mass spectrometer (*m/z* 10–2000) equipped with an Advion Expression CMS detector using sample solutions or solid samples.

Melting points (uncorrected) were determined using a Stanford Research Systems EZ Melt at a heating rate of 5 °C/min. Clearing points are reported.

DSC analyses were carried out at a heating rate of 5 °C/min using a Mettler-Toledo DSC 823e.

UV-vis spectra were acquired on an Analytik Jena UV-vis spectrophotometer Specord s600 using a Hellma Excalibur Q Lab all-quartz immersion probe with an optical pathlength of 1 mm. The corresponding Hellma UV/NIR cuvette interface was used. The temperature of the measurement was regulated by a HAAKE C25P cooling unit with a HAAKE Phoenix II P2 regulating unit. Coolant used was SIL180.

Irradiation of solids and dissolved substances was done by using a Superlite 400 by LUMATEC with different wavelength filters. Emission spectra of the filters used are shown in section *Irradiation experiments* of this document with permission of LUMATEC.

2 Crystallographic details

ORTEP representations of the molecular structures in the cell:

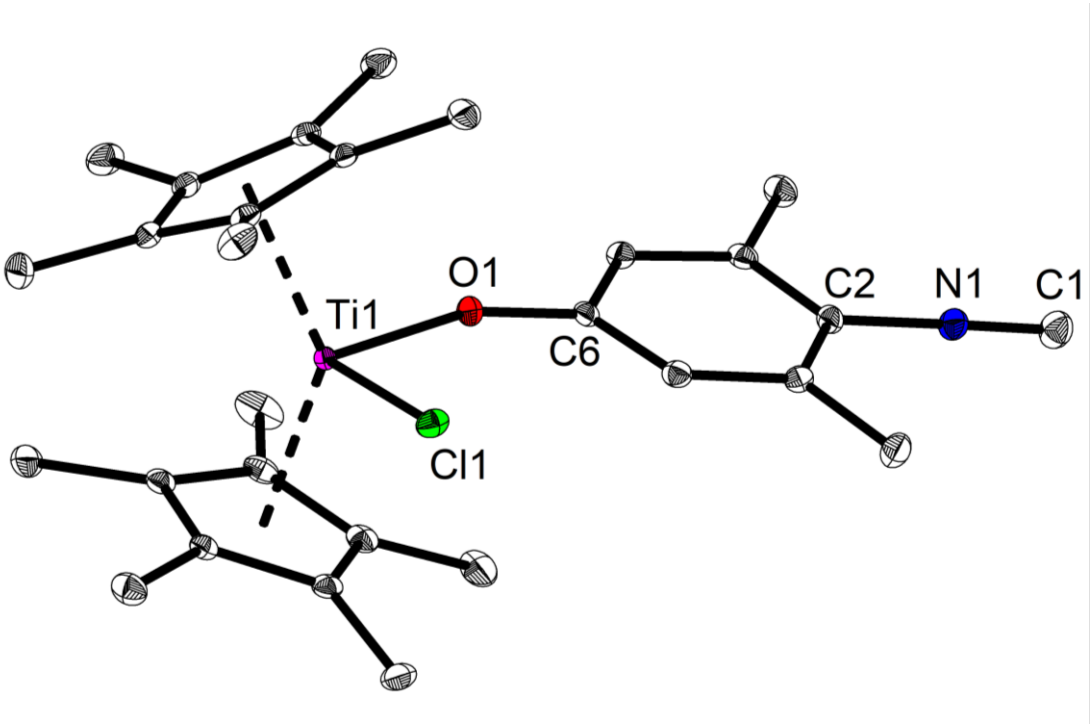

Molecular structure of complex **11Ti**. Thermal ellipsoids correspond to 30% probability at 110 K. Hydrogen atoms are omitted for clarity.

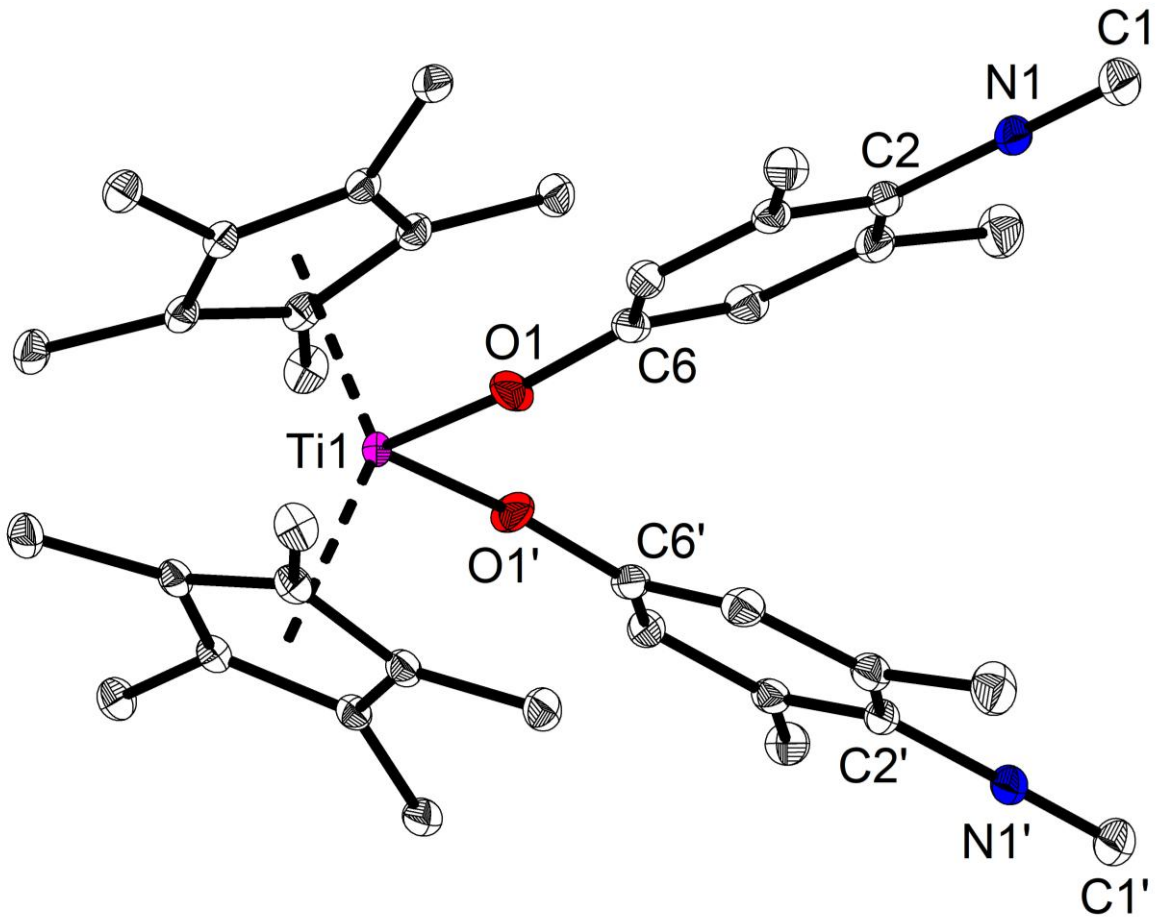

Molecular structure of complex **12Ti**. Thermal ellipsoids correspond to 30% probability at 110 K. Hydrogen atoms and co-crystallized benzene are omitted for clarity.

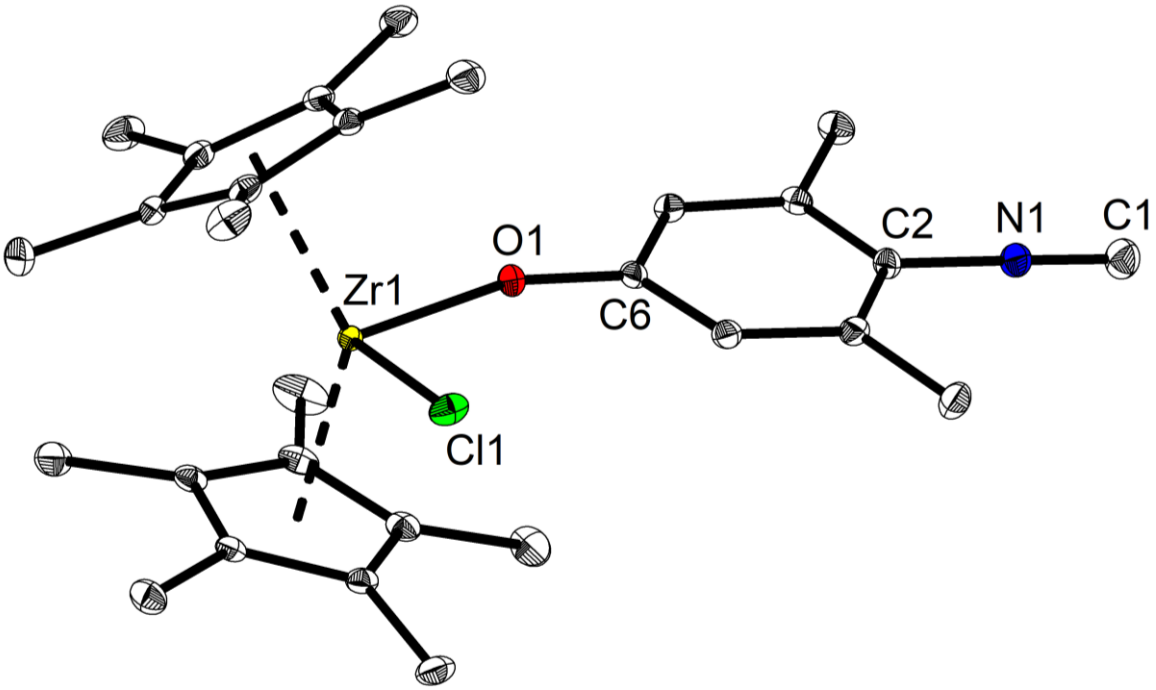

Molecular structure of complex **11Zr**. Thermal ellipsoids correspond to 30% probability at 150 K. Hydrogen atoms are omitted for clarity.

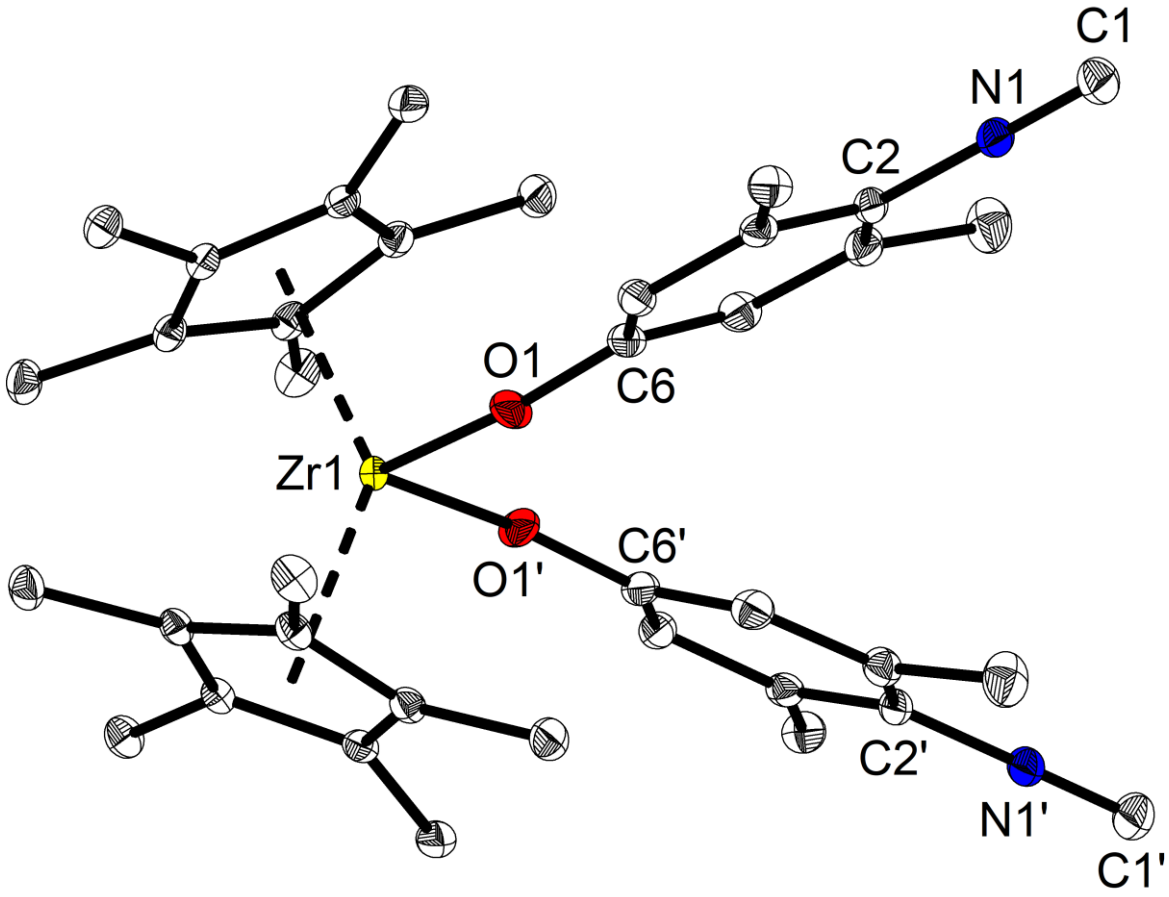

Molecular structure of complex **12Zr**. Thermal ellipsoids correspond to 30% probability at 150 K. Hydrogen atoms are omitted for clarity.

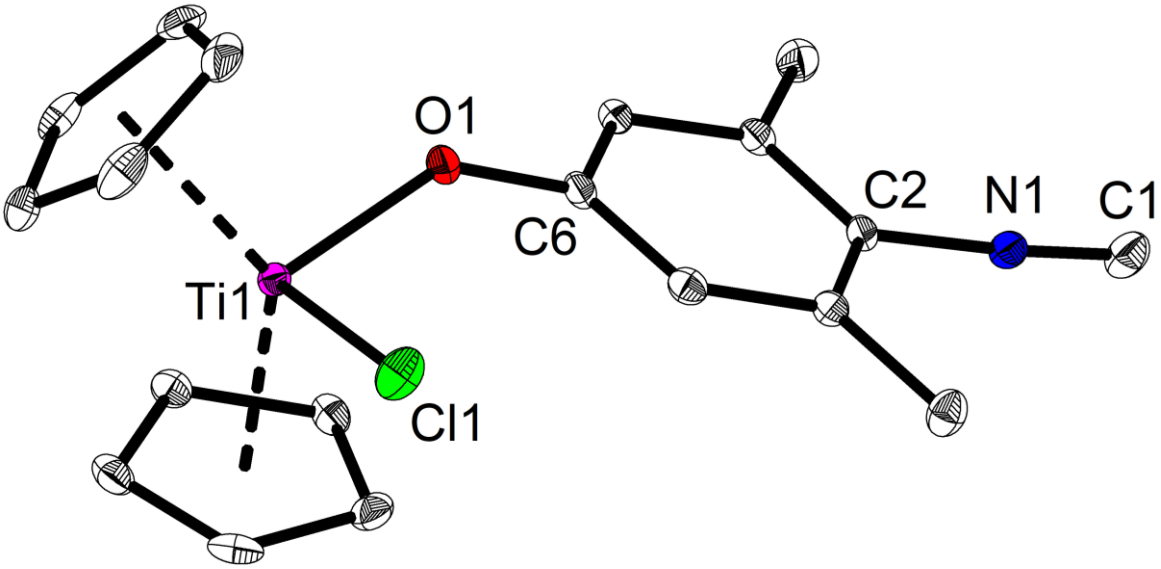

Molecular structure of complex **11Ti_cp**. Thermal ellipsoids correspond to 30% probability at 150 K. Hydrogen atoms and the second molecule of the asymmetric unit are omitted for clarity.

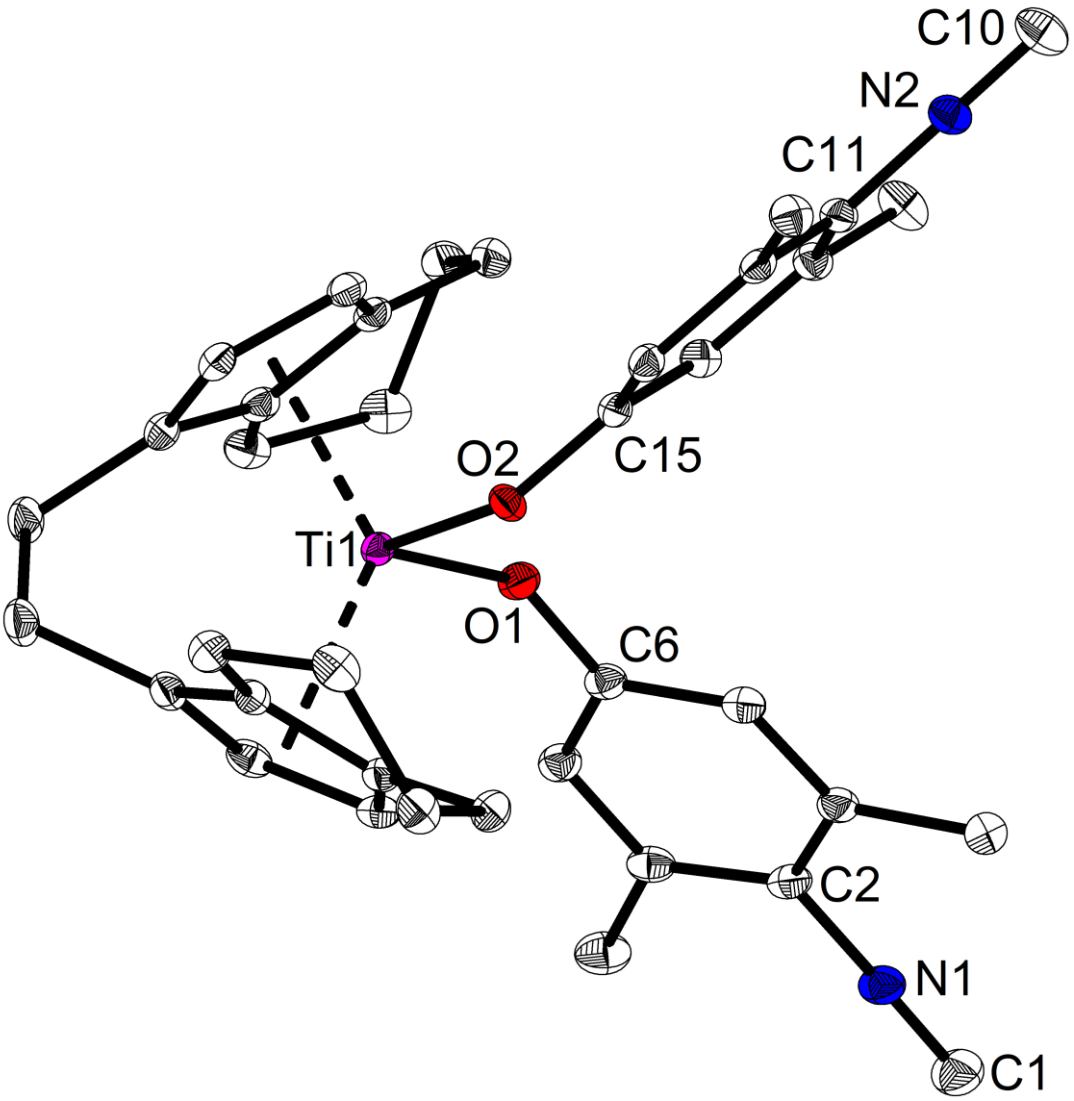

Molecular structure of complex **12Ti**_ *rac*-(ebthi). Thermal ellipsoids correspond to 30% probability at 150 K. Hydrogen atoms and co-crystallized benzene are omitted for clarity.

Table S2. Crystallographic details of complexes **11Ti**, **12Ti**, and **11Zr**.

Compound	**11Ti**	**12Ti**	**11Zr**
Chem. Formula	$C_{29}H_{38}ClNOTi$	$C_{44}H_{52}N_2O_2Ti$	$C_{29}H_{38}ClNOZr$
Formula weight [g/mol]	499.95	688.77	543.27
Colour	red	red	colourless
Crystal system	monoclinic	monoclinic	monoclinic
Space group	$P2_1/n$	$C2/c$	$P2_1/n$
a [Å]	8.4392(3)	14.4489(10)	8.4627(7)
b [Å]	23.9761(8)	12.2043(8)	24.3124(19)
c [Å]	12.8369(4)	21.5210(15)	13.0455(10)
α [°]	90	90	90
β [°]	92.8309(14)	98.178(3)	93.0372(13)
γ [°]	90	90	90
V [Å^3]	2594.24(15)	3756.4(4)	2680.3(4)
Z	4	4	4
$\rho_{calcd.}$ [g/cm^3]	1.280	1.218	1.346
μ [mm^{-1}]	3.893	2.220	0.531
T [K]	110(2)	110(2)	110(2)
Radiation type	CuKα	CuKα	MoKα
Measured reflections	22669	18333	68929
Independent reflections	4561	3333	7133
Reflections with $I > 2\sigma(I)$	4358	3248	6302
R_{int}	0.0275	0.0283	0.0354
$F(000)$	1064	1472	1136
$R_1(R[F^2>2\sigma(F^2)])$	0.0284	0.0317	0.0260
w$R_2(F^2)$	0.0784	0.0891	0.0681
GooF	1.066	1.090	1.038
No. of Parameters	310	229	310
CCDC	2505219	2505220	2505221

Table S3. Crystallographic details of complexes **12Zr**, **9Ti_cp** and **10Ti_rac-(ebthi)**.

Compound	**12Zr**	**9Ti_cp**	**10Ti_** *rac*-(ebthi)
Chem. Formula	$C_{44}H_{52}N_2O_2Zr$	$C_{19}H_{18}ClNOTi$	$C_{41}H_{43}N_2O_2Ti$
Formula weight [g/mol]	732.09	359.69	643.67
Colour	colourless	red	yellow
Crystal system	monoclinic	monoclinic	monoclinic
Space group	*C*2/*c*	$P2_1/n$	*C*2/*c*
a [Å]	14.563(3)	18.968(2)	12.9582(6)
b [Å]	12.311(2)	7.7397(9)	12.7593(6)
c [Å]	21.767(4)	24.179(3)	40.9332(18)
α [°]	90	90	90
β [°]	97.522(3)	107.465(3)	93.756(2)
γ [°]	90	90	90
V [Å^3]	3869.0(13)	3386.0(6)	6753.3(5)
Z	4	8	8
$\rho_{calcd.}$ [g/cm^3]	1.257	1.411	1.266
μ [mm^{-1}]	0.322	0.666	2.437
T [K]	110(2)	123(2)	110(2)
Radiation type	MoKα	MoKα	CuKα
Measured reflections	59923	57950	35076
Independent reflections	5127	8851	6153
Reflections with $I > 2\sigma(I)$	4724	6270	5688
R_{int}	0.0372	0.1039	0.0418
F(000)	1544	1488	2728
$R_1(R[F^2>2\sigma(F^2)])$	0.0268	0.0655	0.0326
$wR_2(F^2)$	0.0691	0.1131	0.0836
GooF	1.050	1.090	1.037
No. of Parameters	229	419	420
CCDC	2505222	2505223	2505224

3 Syntheses of starting materials

3.1 Cp*$_2$Ti(Cl)OarNC

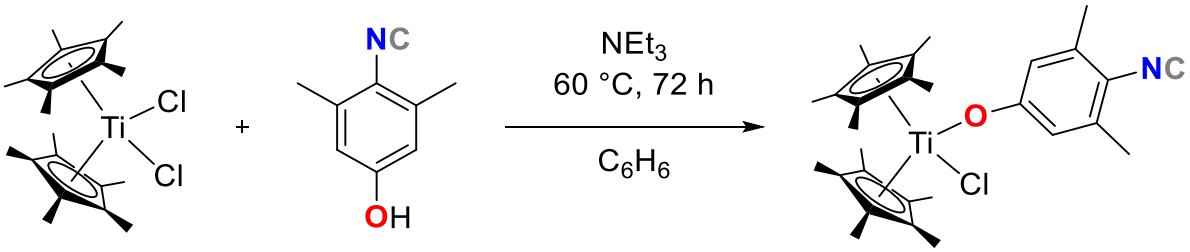

Cp*$_2$TiCl$_2$ (778.5 mg, 2.0 mmol) and 4-isocyano-3,5-dimethylephenole (323.8 mg, 2.2 mmol) were dissolved in benzene (20 mL) at 60 °C (oil bath). To the resulting dark red solution, NEt$_3$ (310 mg, 3 mmol) was added in one single portion via syringe. The system was stirred at this temperature for 72 h, resulting in a brown suspension. The supernatant was filtered off, and the remaining yellow residue was extracted with fresh benzene (3 x 10 mL). The solvent of the combined benzene extracts was removed *in vacuo* and the remaining brown-black solid was dissolved in THF (15 mL) at 60 °C (water bath). The THF solution was concentrated to approx. 5 mL and subsequently stored at –78 °C for 24 h to induce crystallization. The supernatant was filtered off, and the resulting crystals were dried *in vacuo* (1x10^{-3} mbar, 70 °C, 3 h, oil bath). The product contains Cp*$_2$TiCl$_2$ (<10%) as a non-separable impurity. Yield: 650.0 mg (1.3 mmol, 65%).

Single crystals for X-ray structure determination were obtained by overlaying a saturated THF solution at ambient temperature with Et$_2$O.

Mp. 226 °C. **CHN** calculated (found) in % (deviation due to Cp*$_2$TiCl$_2$ contamination, see above): C: 69.67 (60.02), H: 7.66 (7.59), N: 2.80 (2.11). **^{1}H NMR** (400 MHz, C$_6$D$_6$) δ = 6.54 (s, 2H, Ar-C*H*), 2.24(s, 6H, C*H*$_3$), 1.78 (s, 30 H, Cp*-*H*). **^{13}C{^{1}H} NMR** (101 MHz, C$_6$D$_6$) δ = 167.9, 127.1, 19.2, 12.6. No further signals could be detected due to poor solubility. **Raman** (633 nm, cm^{-1}) No spectra could be recorded due to decomposition of the

sample under irradiation. **MS** (CI-pos., m/z): 852 $[M+Cp^*_2TiCl]^+$, 500 $[M+H]^+$, 353 $[M-Oar^{NC}]^+$.

Figure S1. ^{1}H NMR spectrum of $Cp^*_2Ti(Cl)OarNC$.

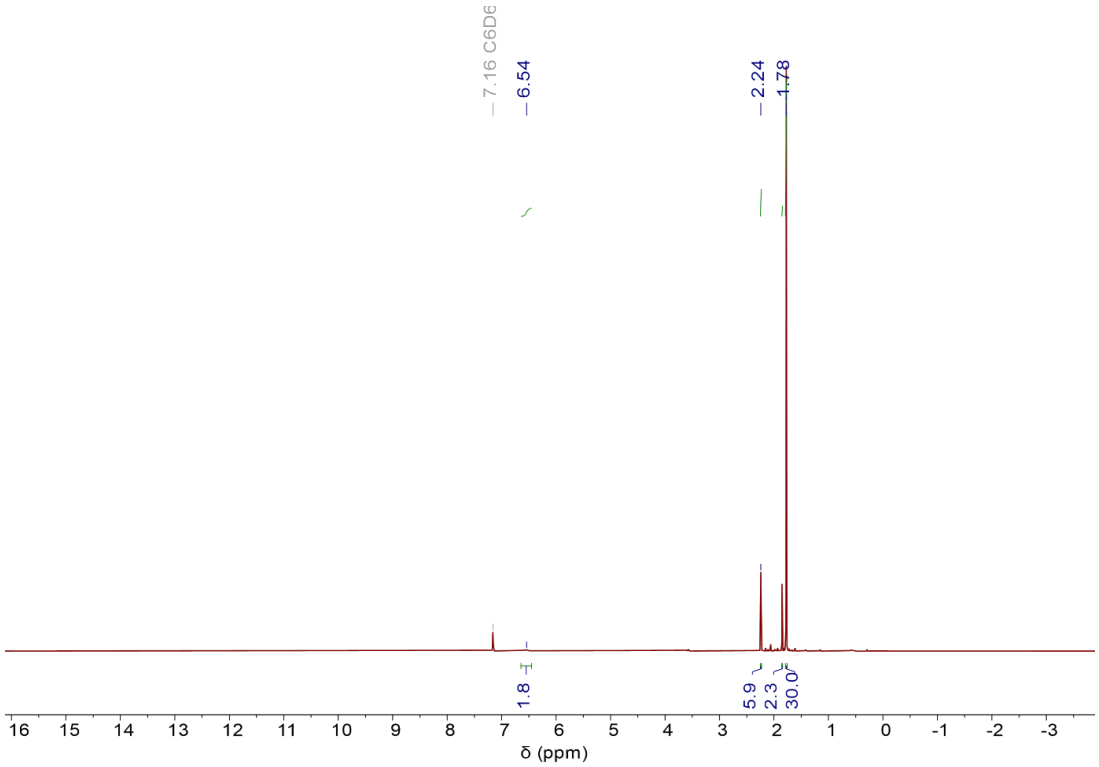

Figure S2. Section of the ^{1}H NMR spectrum of $Cp^*_2Ti(Cl)OarNC$.

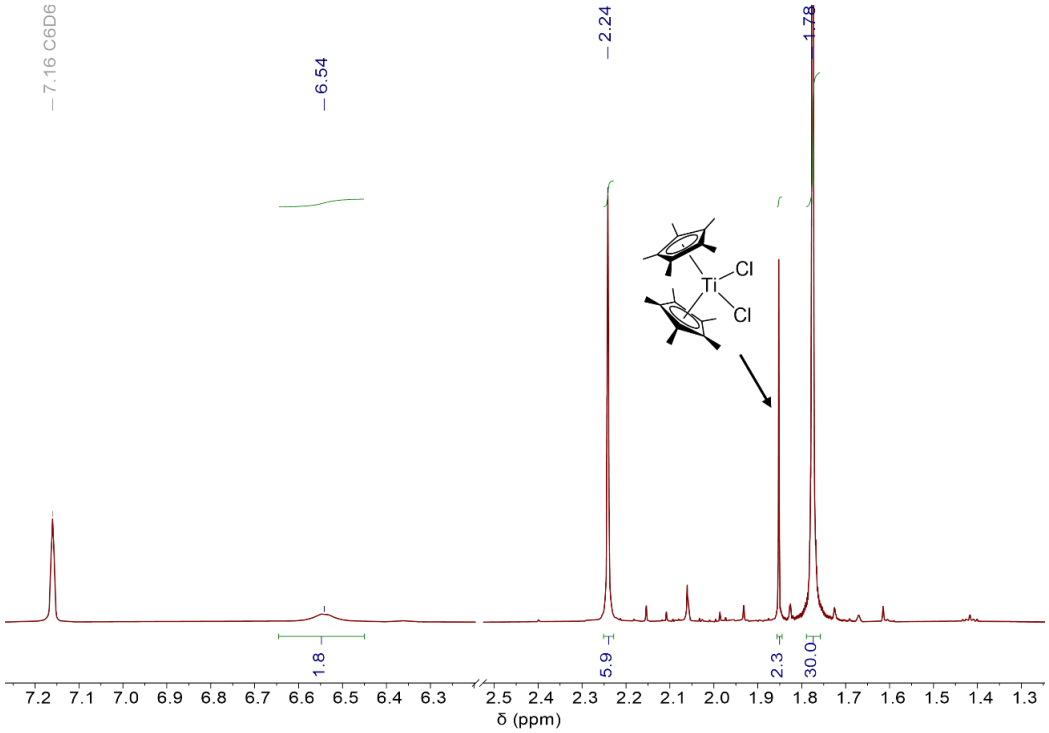

Figure S3. ^{13}C NMR spectrum of $Cp^*_2Ti(Cl)OarNC$.

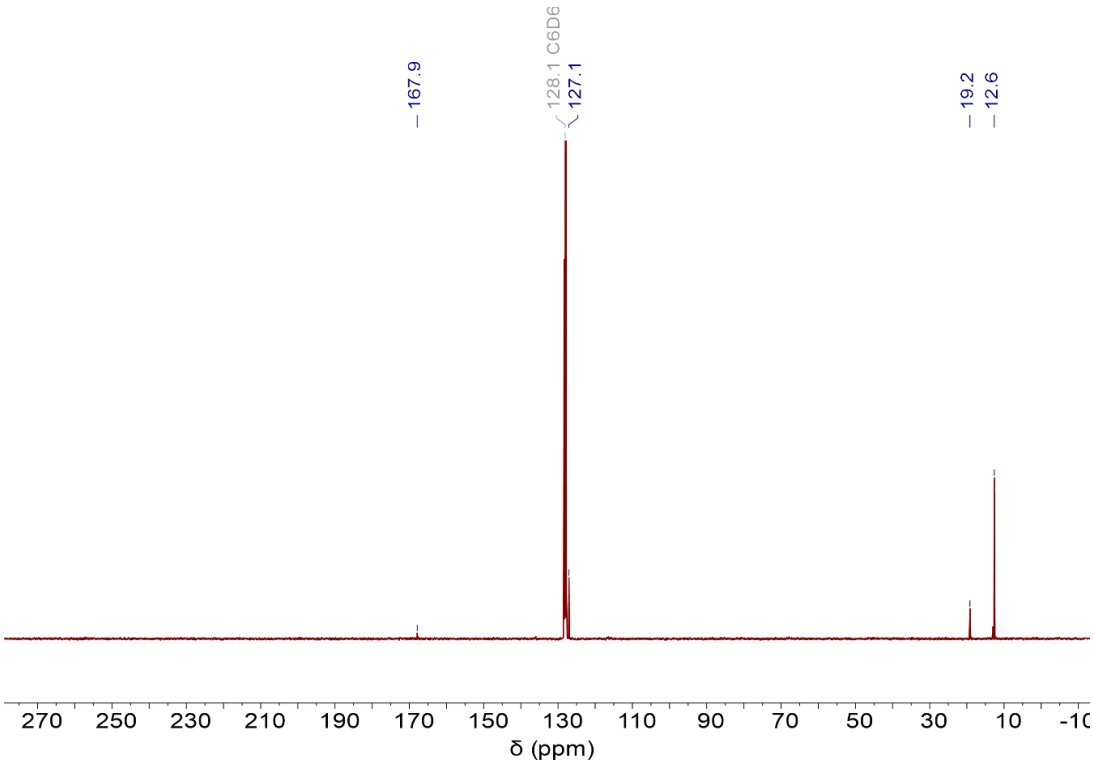

3.2 $Cp^*_2Ti(OarNC)_2$

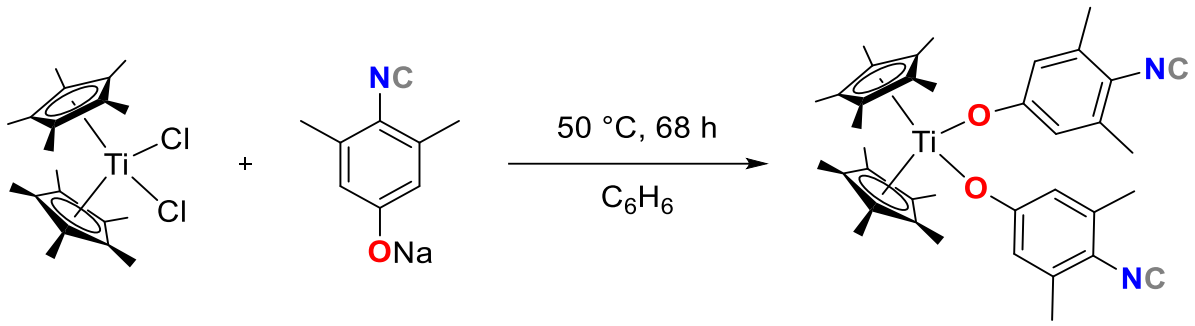

$Cp^*_2TiCl_2$ (350.3 mg, 0.9 mmol) and sodium-4-isocyano-3,5-dimethylephenolate (304.5 mg, 1.8 mmol) were suspended in benzene (10 mL) at ambient temperature. The mixture was stirred for 68 h at 50 °C (oil bath). Afterwards, the solvent was removed *in vacuo* and the dark red residue was suspended in THF (10 mL). The dark red suspension was filtered off and the remaining solid was extracted with fresh THF (2x5 mL). The combined THF solutions were concentrated to 15rradia. 7 mL, overlaid with Et_2O at ambient temperature, and the mixture was stored without vibrations for three days at

–78 °C, whereby red crystals were obtained. The supernatant was removed by syringe, and the isolated crystals were dried *in vacuo* ($1x10^{-3}$ mbar, 3 Yield: 428.7 mg (0.702 mmol, 78%).

Single crystals for X-ray structure determination were obtained by cooling a saturated benzene-d_6 solution from 60 °C to ambient temperature.

Mp. 192 °C. **CHN** calculated (found) in %: C: 74.74 (74.01), H: 7.59 (7.32), N: 4.59 (4.43). **^{1}H NMR** (THF-d_8, 400 MHz): δ = 6.41 (s, 4H, Ar-*H*), 2.27 (s, 12H, *CH*$_3$), 1.96 (s, 30H, Cp*-*H*). **^{13}C{^{1}H} NMR** (101.5 MHz, C_6D_6) δ = 166.1, 127.2, 118.9, 19.5, 12.9. No further signals could be detected due to poor solubility. **IR** (ATR, neat, cm^{-1}): 2984 (w), 2913 (w), 2859 (w), 2109 (w), 1587 (m), 1466 (m), 1381 (w), 1332 (s), 1310 (m), 1233 (s), 1190 (s), 1144 (s), 1062 (w), 1034 (m), 982 (s), 890 (w), 858 (m), 809 (w), 749 (s), 712 (m), 687 (s), 625 (m), 592 (w), 520 (w), 506 (m), 479 (m), 439 (w), 414 (m). **Raman** (633 nm, 25 s, 10 scans, cm^{-1}): $\tilde{\nu}$ = 3062 (1), 2920 (3), 2111 (10), 1591 (6), 1429 (2), 1383 (2), 1346 (5), 1162 (2), 1148 (2), 1148 (2), 991 (4), 944 (1), 634 (1), 611 (2). **MS** (CI-pos., m/z): 464 $[M-Oar^{NC}]^+$.

Figure S4. ^{1}H NMR spectrum of $Cp^*_2Ti(OarNC)_2$.

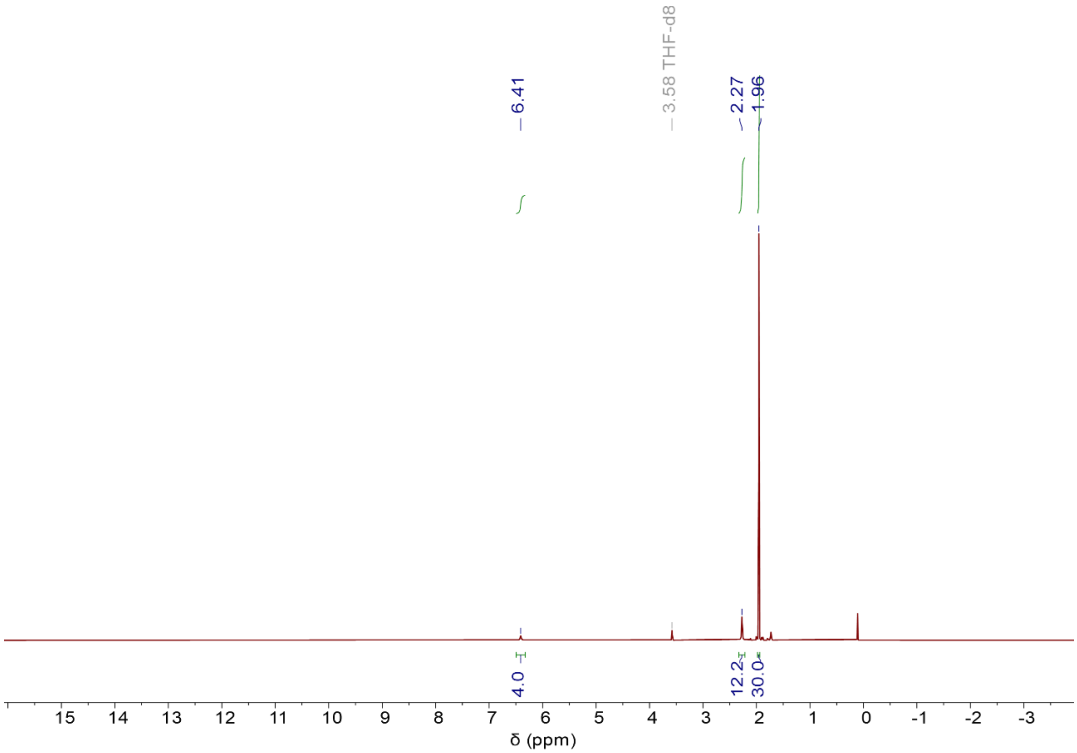

Figure S5. IR spectrum (top) and Raman spectrum (bottom) of $Cp^*_2Ti(OarNC)_2$.

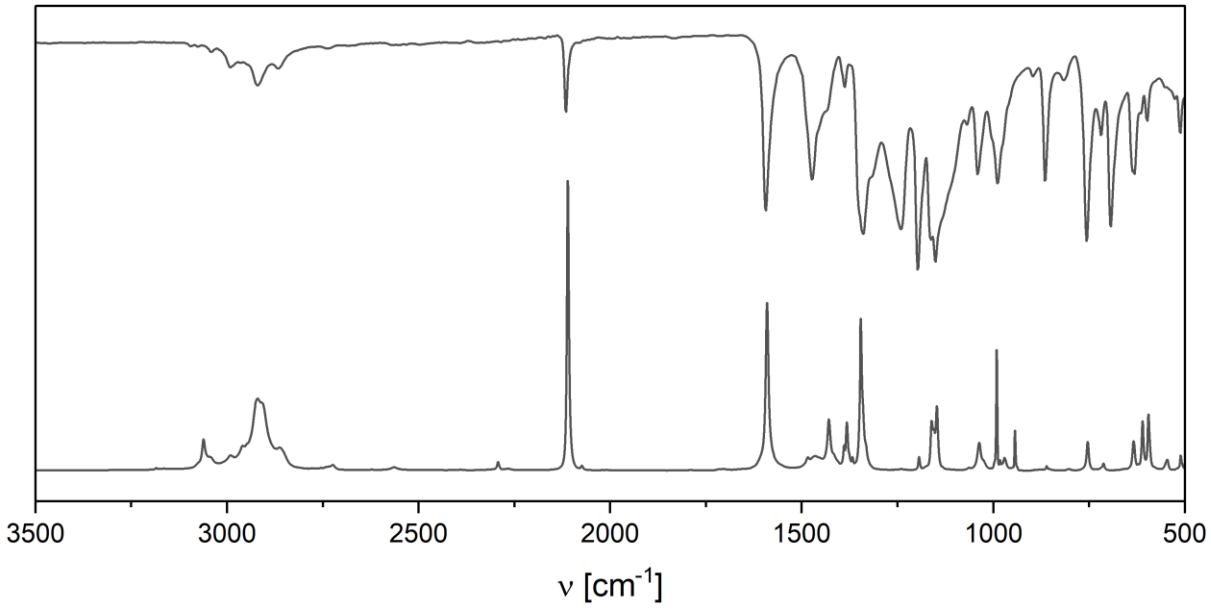

3.3 $Cp^*_2Zr(Cl)OarNC$

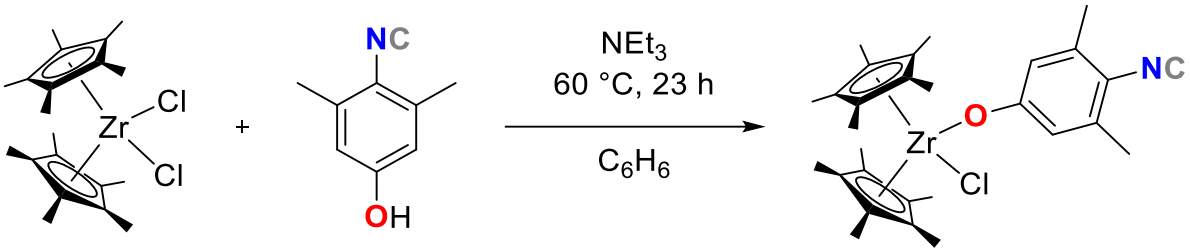

$Cp^*_2ZrCl_2$ (800.0 mg, 1.85 mmol) and 4-isocyano-3,5-dimethylephenole (271.5 mg, 1.85 mmol) were dissolved in benzene (20 mL) at 60 °C (oil bath). To the resulting clear, light-yellow solution, NEt_3 (690 mg, 6.8 mmol, 3.7 eq.) was added in one single portion via syringe. After stirring for five minutes, the mixture became cloudy, and after 23 h of reaction time, the mixture became a dark green suspension. The mixture was cooled to ambient temperature, filtered, and the resulting residue was extracted with fresh benzene (3x5 mL). The solvent was removed, and the resulting light brown residue was dissolved in toluene (20 mL) at 50 °C (water bath). The solution was concentrated to 17rradia. 15 mL at this temperature, slowly cooled to ambient temperature and subsequently to –78 °C overnight, resulting in nearly colorless (slightly yellow) crystals.

The mother liquor was removed by syringe, and the crystals were dried *in vacuo* (1×10^{-3} mbar, 70 °C, 5 h, oil bath). Yield: 721 mg (1.33 mmol, 72%).

Single crystals for X-ray structure determination were obtained by overlaying a saturated benzene solution at ambient temperature with *n*-hexane.

Mp. 297 °C. **CHN** calculated (found) in %: C: 64.11 (63.87), H: 7.05 (6.93), N: 2.58 (2.07). **^{1}H NMR** (400 MHz, C_6D_6) δ = 6.54 (s, 2H, Ar-C*H*), 2.24(s, 6H, CH_3), 1.78 (s, 30 H, Cp*-*H*). **^{13}C NMR** (101 MHz, C_6D_6) δ = 169.3, 164.1, 136.7, 129.7, 123.1, 117.7, 19.4, 12.0. **Raman** (633 nm, 10 s, 15 scans, cm^{-1}): $\tilde{\nu}$ = 2913 (8), 2873 (2), 2862 (2), 2112 (3), 1588 (2), 1483 (1), 1429 (3), 1340 (4), 1158 (2), 1145 (1), 755 (1), 631 (1), 612 (2), 596 (3), 551 (1), 484 (1), 403 (3), 390 (1), 365 (1), 334 (4), 313 (2), 245 (1), 144 (3), 129 (5), 104 (2) 77 (10). **MS** (CI-pos., m/z): 543 $[M+H]^+$.

Figure S6. ^{1}H NMR spectrum of $Cp^*_2Zr(Cl)OarNC$.

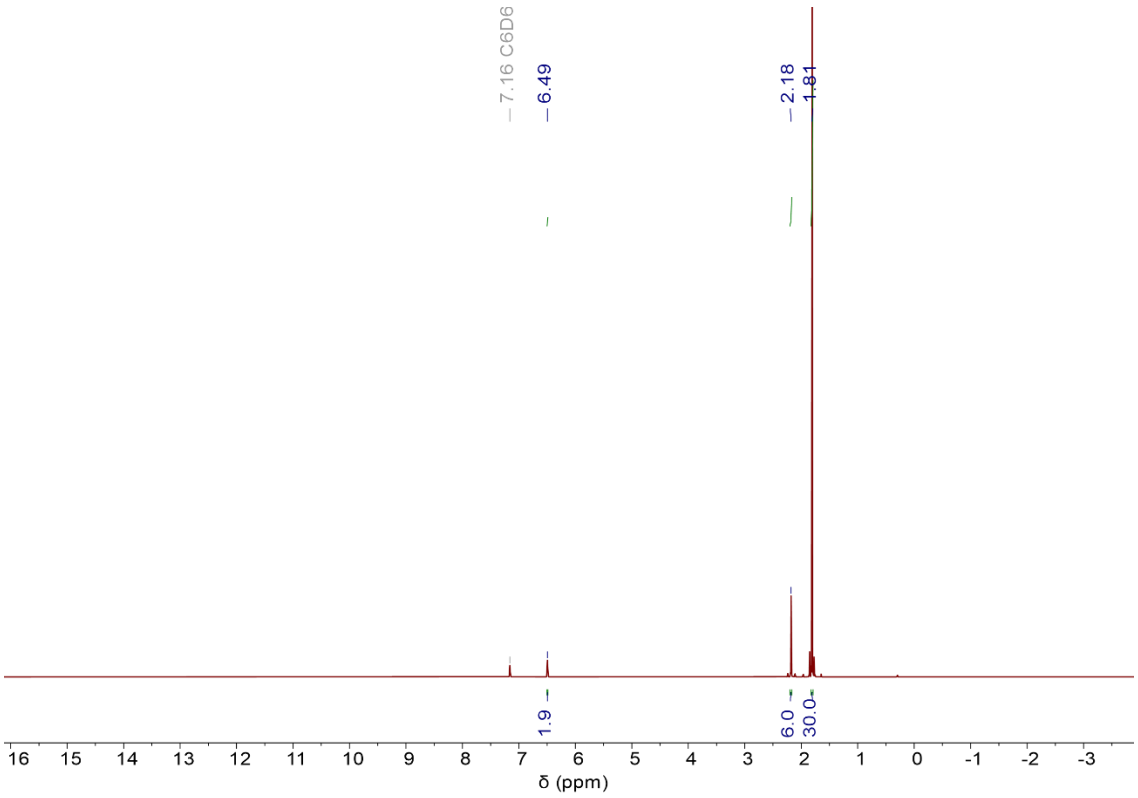

Figure S7. ^{13}C NMR spectrum of Cp*$_2$Zr(Cl)OarNC (solvent signals indicated by asterisks).

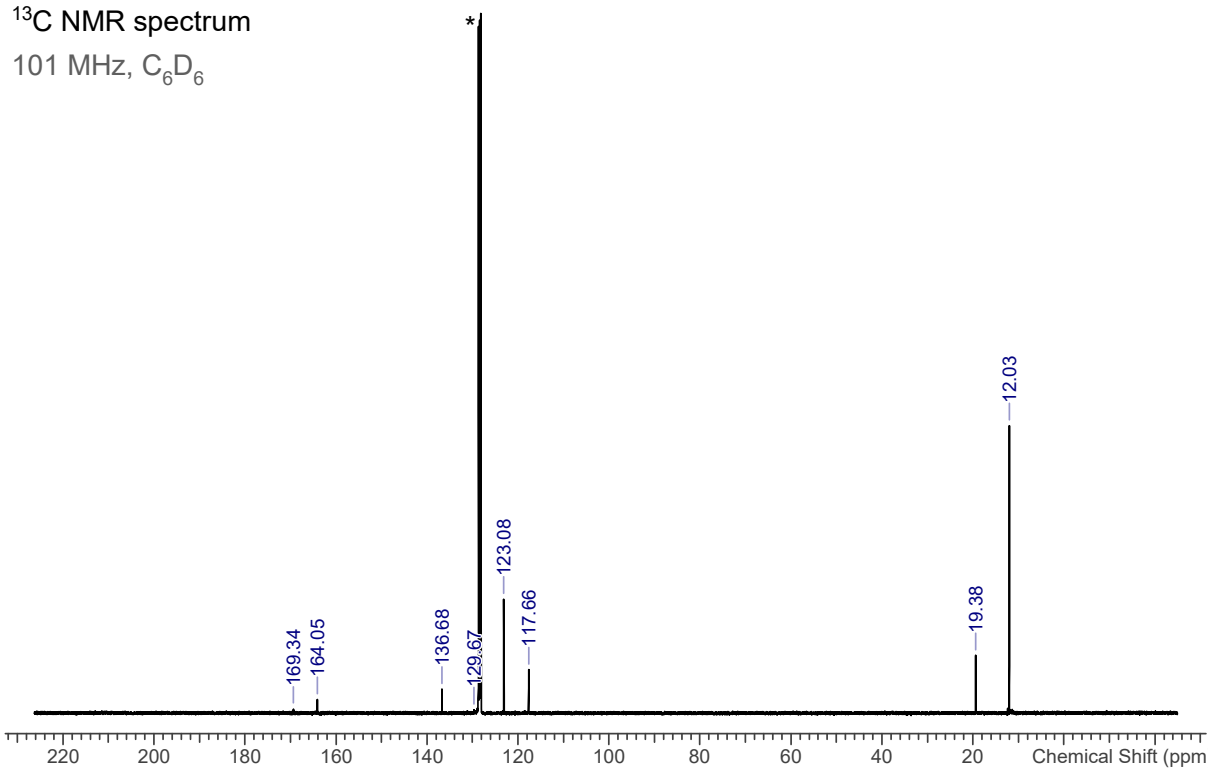

Figure S8. Raman spectrum of Cp*$_2$Zr(Cl)OarNC (baseline corrected).

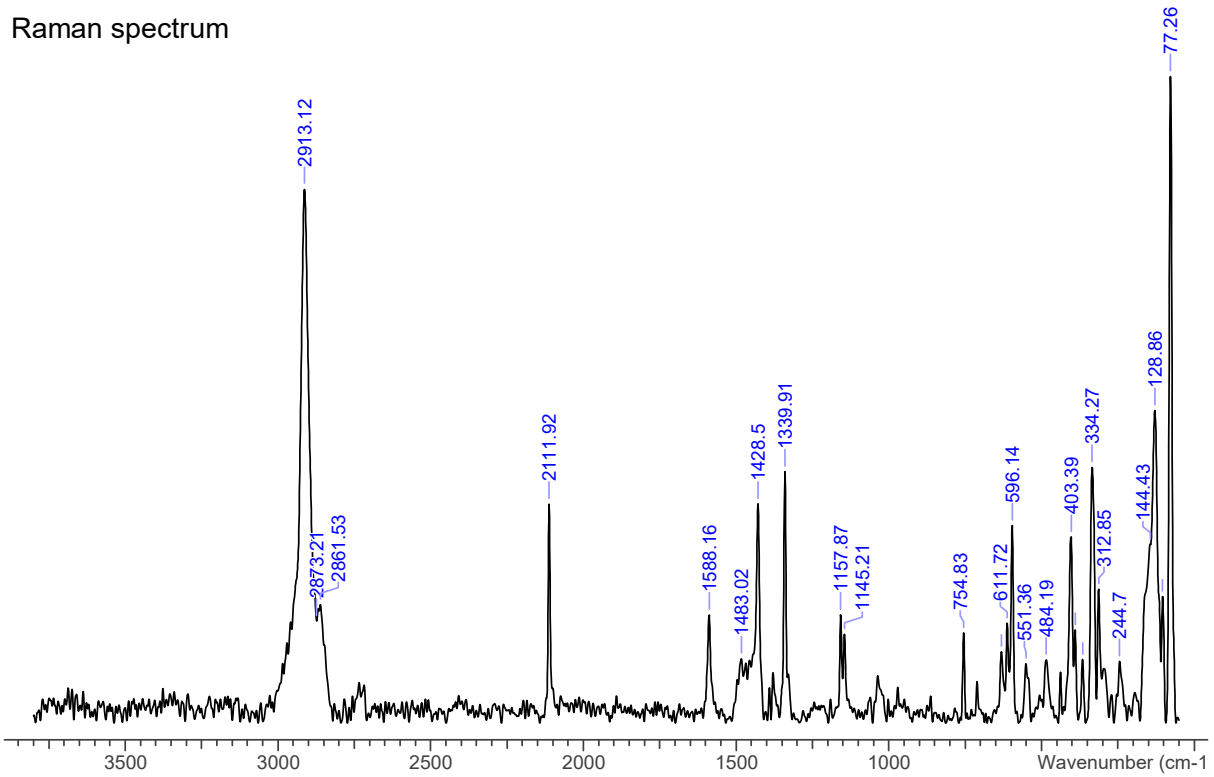

3.4 Cp*$_2$Zr(OarNC)$_2$

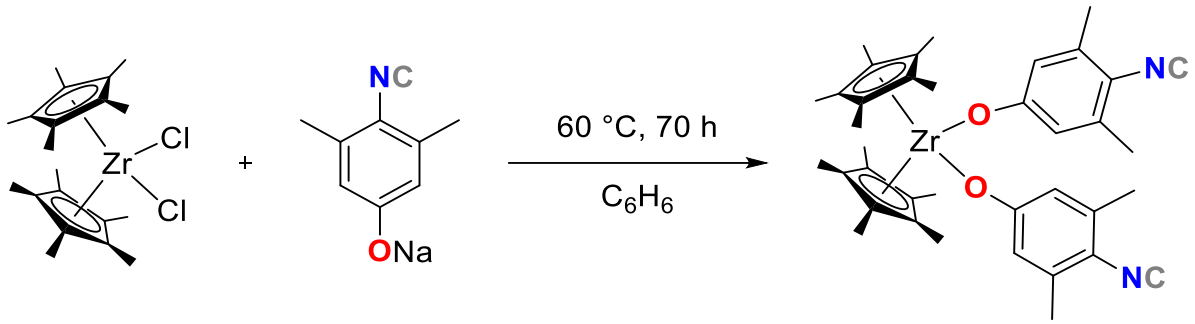

Cp*$_2$ZrCl$_2$ (700 mg, 1.6 mmol) and sodium-4-isocyano-3,5-dimethylephenolate (547.5 mg, 3.24 mmol) were suspended in benzene (20 mL) at ambient temperature. The mixture was stirred at 60 °C (oil bath) for 70 h. The light-yellow suspension was cooled to ambient temperature, filtered, and the resulting residue was extracted with fresh benzene (2x12 mL). The combined benzene solutions were concentrated to 20rradia. 10 mL at 50 °C (water bath) and subsequently cooled to ambient temperature, whereby fine colorless crystals were obtained. The supernatant was removed by syringe and further concentrated (to 20rradia. 2 mL) to obtain a second fraction of crystals. The crystals were dried *in vacuo* (1×10^{-3} mbar, 3 h, ambient temperature). Yield: 868.8 mg (1.33 mmol, 82%).

Single crystals for X-ray structure determination were obtained by cooling a saturated benzene solution from 60 °C to ambient temperature.

Mp. 304 °C. **CHN** calculated (found) in %: C: 69.79 (68.81), H: 7.09 (6.83), N: 4.28 (4.05). **^{1}H NMR** (C_6D_6, 400 MHz): δ = 6.49 (s, 4H, Ar-*H*), 2.24 (s, 12H, C*H*$_3$), 1.77 (s, 30H, Cp*-*H*). **^{13}C NMR** (C_6D_6, 101 MHz): δ = 169.3, 164.0, 136.4, 128.6, 122.3, 118.7, 118.0, 19.2, 11.6. **IR** (ATR, neat, cm^{-1}): 2988 (w), 2910 (w), 2860 (w), 2109 (m), 1587 (s), 1468 (sm), 1380 (w), 1332 (s), 1311 (m), 1231 (s), 1194 (s), 1141 (s), 1062 (w), 1033 (m), 984 (s), 891 (w), 861 (m), 807 (w), 750 (s), 711 (m), 687 (s), 623 (m), 591 (w), 520 (w), 505 (m), 481 (m), 437 (w), 414 (m). **Raman** (633 nm, 15 s, 25 scans, cm^{-1}): $\tilde{\nu}$ = 3060 (1), 2921 (2), 2113 (10), 1590 (5), 1424 (2), 1388 (1), 1341 (4), 1161 (1), 1149 (2), 1150 (2), 990 (5), 947 (2), 631 (1), 617 (2). **MS** (CI-pos., m/z): 653 [M+H]$^+$.

Figure S9. ^{1}H NMR spectrum of $Cp^*_2Zr(OarNC)_2$.

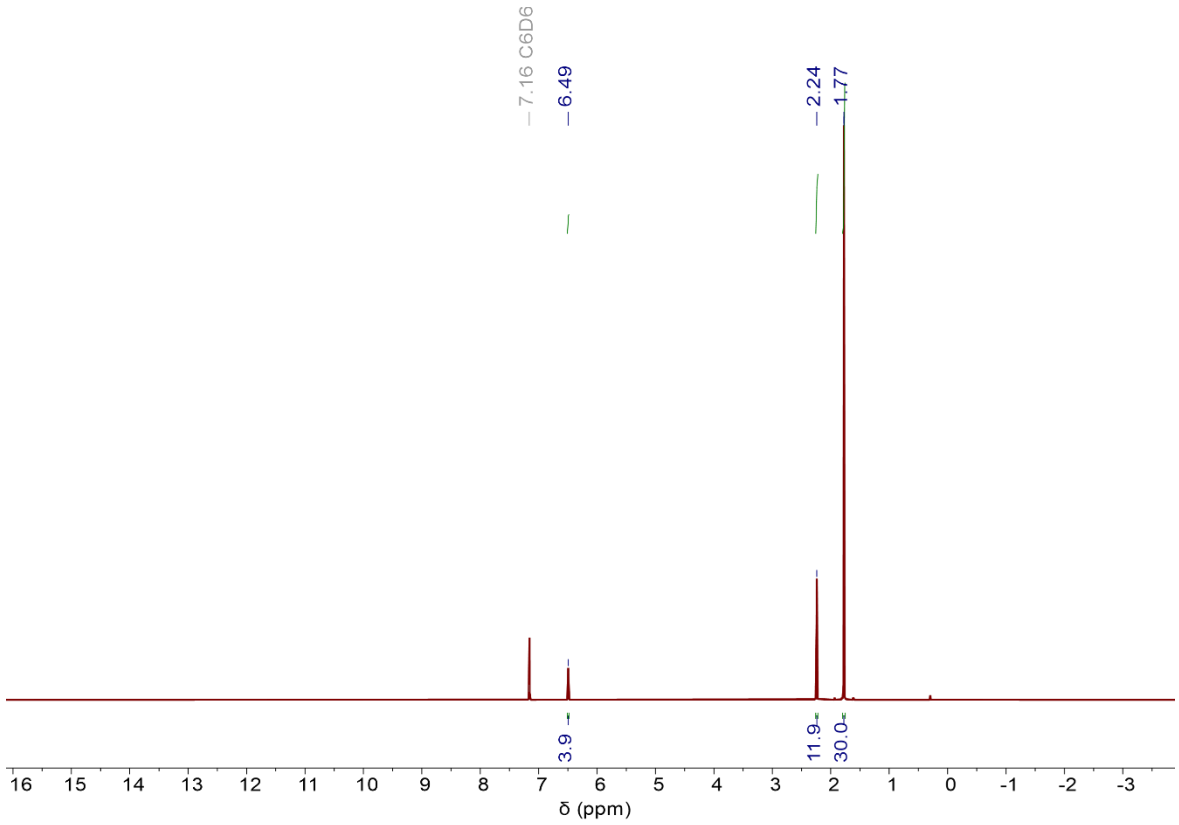

Figure S10. ^{13}C NMR spectrum of $Cp^*_2Zr(OarNC)_2$.

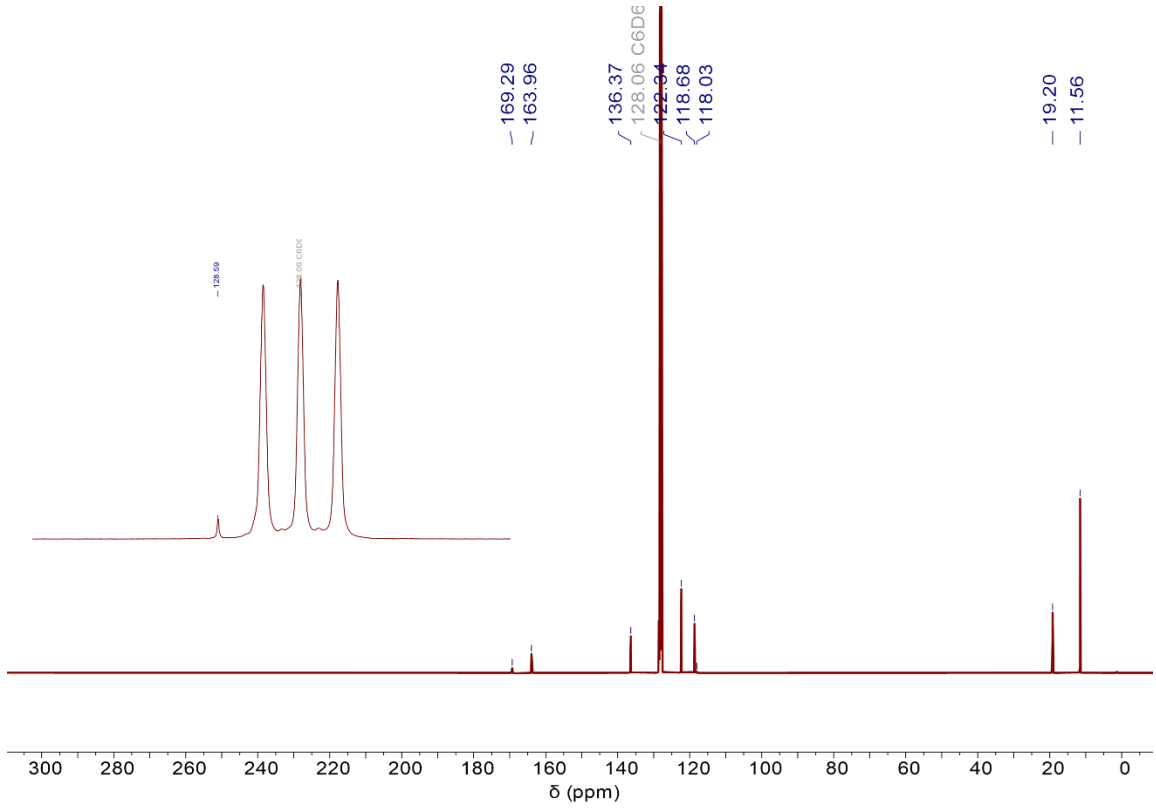

Figure S11. IR spectrum (top) and Raman spectrum (bottom) of $Cp^*_2Zr(OarNC)_2$.

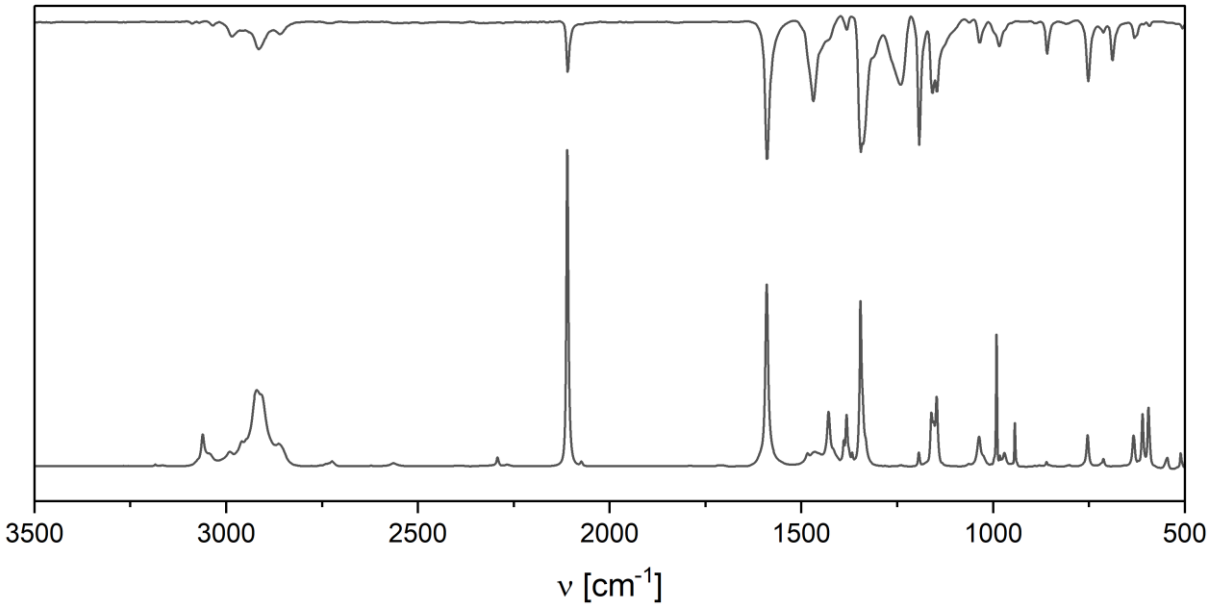

4 Syntheses of biradicals

4.1 $Cp^*_2Ti(Cl)OArNCN_2P_2$

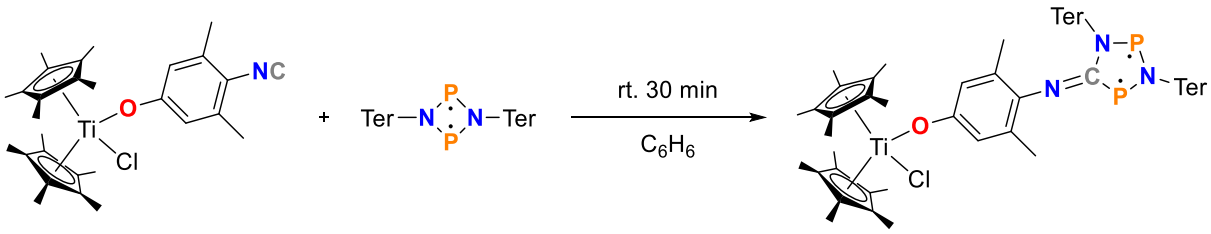

P_2N_2-Biradical (296 mg, 0.413 mmol) and $Cp_2Ti(Cl)OArNC$ (100 mg, 0.200 mmol) were combined, dissolved in benzene (10 mL), and the resulting dark green mixture was stirred at ambient temperature. After 30 minutes, the mixture was filtered via a P4-Schlenk frit. All volatile compounds were removed *in vacuo* (1×10^{-3} mbar) and the resulting dark green residue was dissolved in toluene (3 mL). The dark green solution was heated to 80 °C (oil bath), concentrated to approximately 2 mL, and cooled to ambient temperature in darkness. The solvent was removed *in vacuo* (1×10^{-3} mbar) and the remaining green product was thoroughly dried *in vacuo* (1×10^{-3} mbar) for two hours at ambient temperature (water bath). Yield: 209 mg (0,171 mmol, 85%).

^{1}H NMR (C_6D_6, 399.87 MHz): δ = 6.98 (s, 1H), 6.96 (s, 1H), 6.94 (s, 1H), 6.90 (s, 1H), 6,88 (s, 3H), 6.88 (s, 2H), 6.86 (s/m, 4H), 6.84 (s, 1H), 6.79 (s, 4H), 6,76 (s, 1H), 6.74 (s/m, 3H), 6.73 (s/d, 8H), 6,60 (s, 1H), 2.32 (s, 6H), 2.30 (s, 6H), 2.28 (s, 12H), 2.27 (s, 6H), 2.11 (s/m, 3H), 2.08 (s/m, 3H), 2.03 (s, 24H), 1.89 (s, 30H), 1.72 (s, 6H), 1.66 (s, 6H). **^{13}C NMR** (C_6D_6, 100.5 MHz): δ = 163.9, 143.6, 140.9, 138.5, 138.3, 138.0, 137.1, 136.6, 136.2, 136.1, 132.8, 132.6, 131.5, 130.4, 130.3, 129.7, 129.0, 126.2, 124.8, 117.6, 22.1, 21.8, 21.7, 21.3, 20.7, 19.2, 13.1, additional signals due to isomerization. **^{31}P{^{1}H} NMR** (C_6D_6, 161.8 MHz): δ = 276.9 (s), 261.5 (d, 148 Hz), 227.2 (d, 148 Hz); *Note*: additional signals due to CN-bridged biradical species are often observed at 246.8 (d, 48 Hz), 228.5 (d, 6 Hz), 200.2 (d, 6 Hz), 170.4 (d, 47 Hz) which disappear after re-crystallization (see ^{31}P NMR spectra below).

Figure S12. ^{1}H, ^{13}C and ^{31}P NMR spectra of $Cp^*_2Ti(Cl)OArNCN_2P_2$ (solvent signals indicated by asterisks).

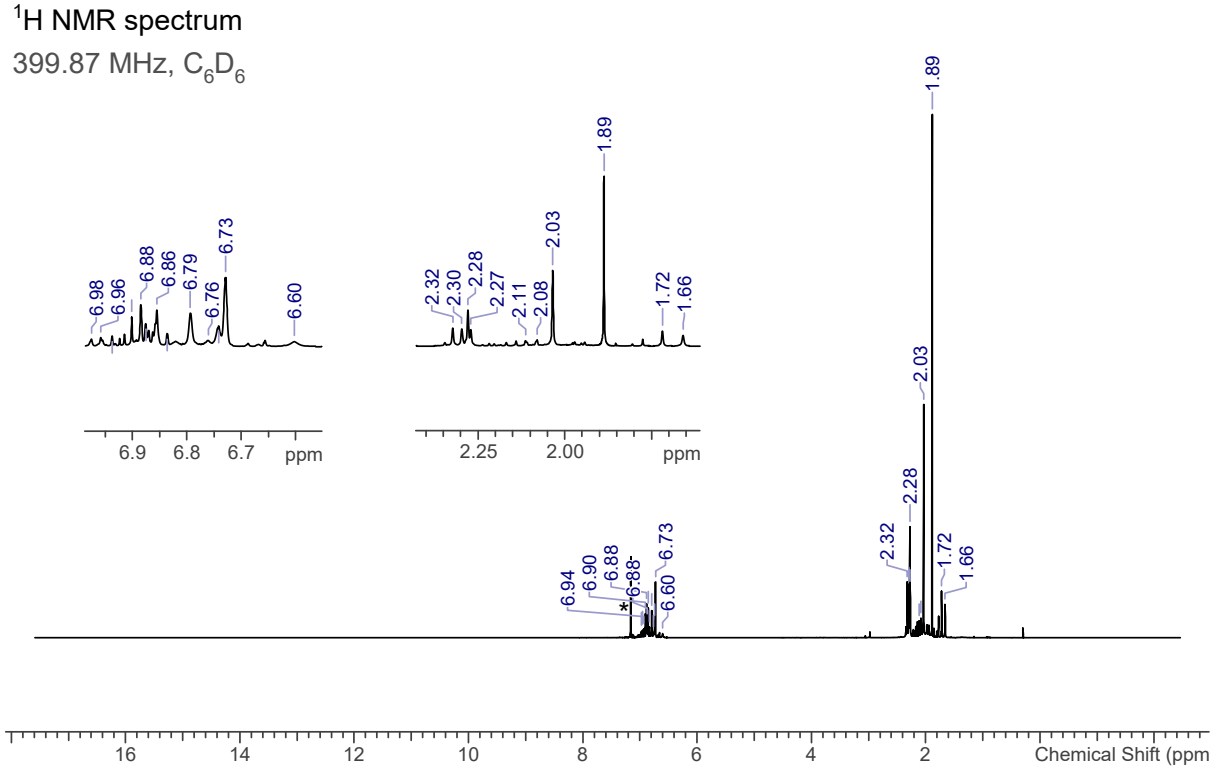

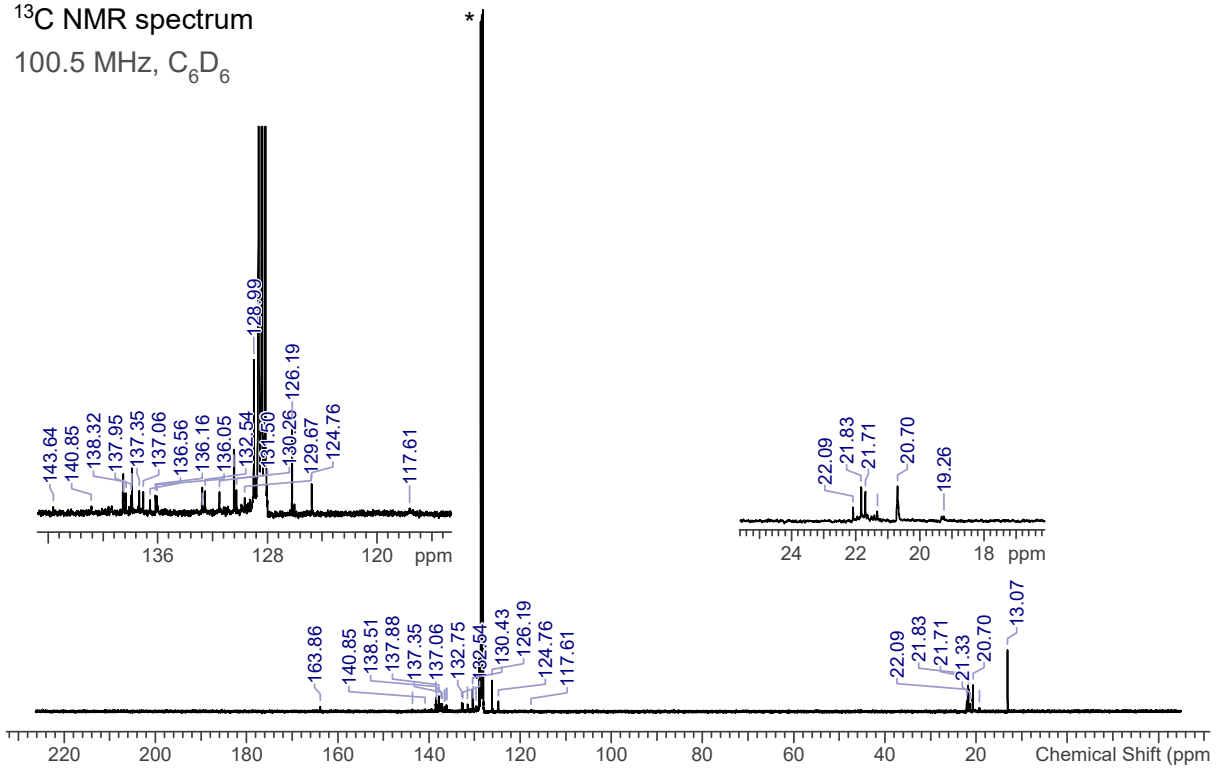

^{31}P NMR spectrum

161.8 MHz, C_6D_6

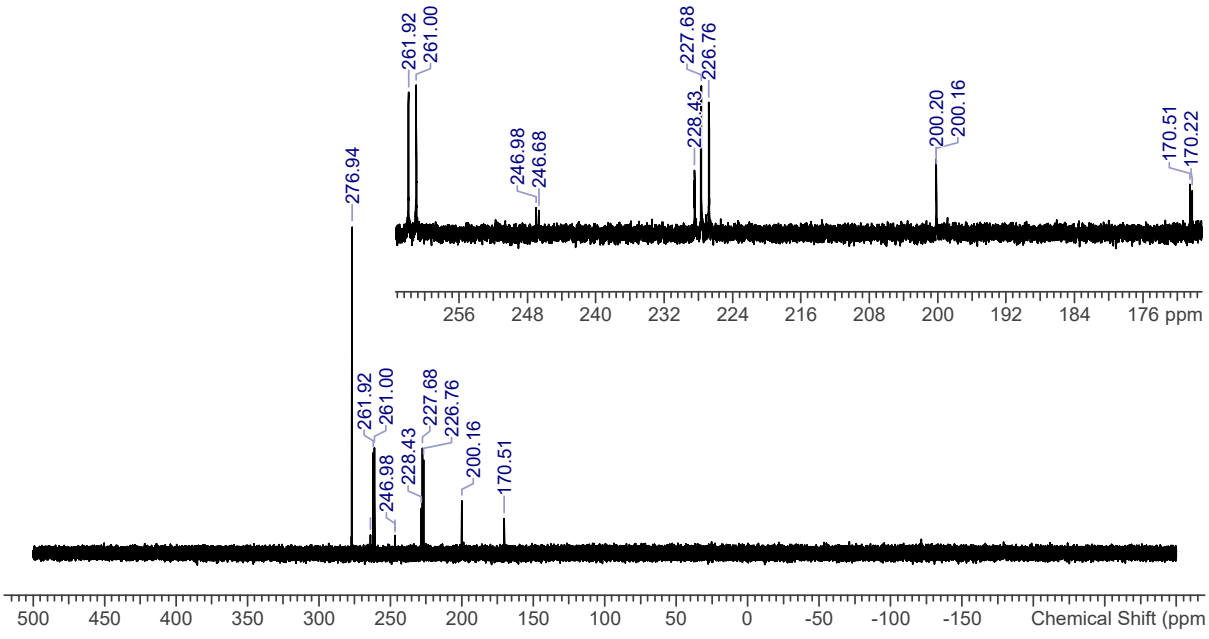

After re-crystallization:

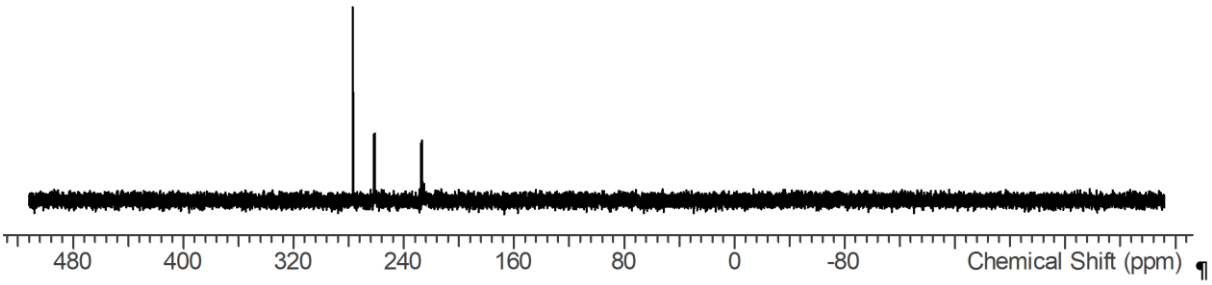

4.2 $Cp^*_2Ti(OArNCN_2P_2)_2$

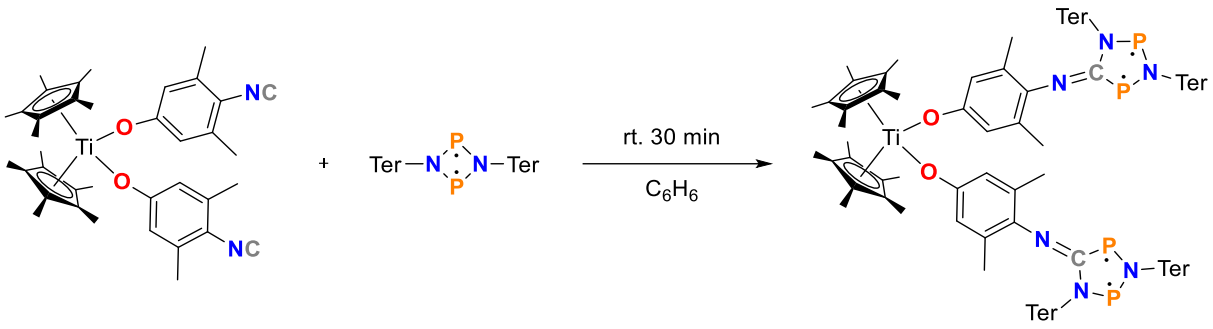

P_2N_2-Biradical (472 mg, 0.658 mmol) and $Cp_2Ti(OarNC)_2$ (100 mg, 0.164 mmol) were combined, dissolved in benzene (10 mL), and the resulting dark green-brown mixture was stirred at ambient temperature. After 30 minutes, the mixture was filtered via a P4-Schlenk frit. All volatile compounds were removed *in vacuo* (1×10^{-3} mbar) and the resulting dark green-brown residue was dissolved in toluene (3 mL). The dark green-brown solution was heated to 80 °C (oil bath), concentrated to approximately 2 mL, and cooled to ambient temperature in darkness. The solvent was removed *in vacuo* (1×10^{-3} mbar), and the remaining dark green-brown product was thoroughly dried *in vacuo* (1×10^{-3} mbar) for two hours at ambient temperature (water bath). Yield: 218 mg (0.107 mmol, 65%).

^{1}H NMR (C_6D_6, 399.87 MHz): δ = 7.13 (s/m, 1H), 7.11 (s/m, 1H), 7.02 (s/m, 1H), 7.00 (s/m, 1H), 6.92 (m, 2H), 6.90 (s, 1H), 6.90 (s, 1H), 6.88 (s, 4H), 6.87 (s, 2H), 6.85 (s, 1H), 6.83 (m, 4H), 6.77 (s/m, 3H), 6.73 (s/m, 9H), 6.65 (s, 2H), 2.36 (s, 6H), 2.32 (m, 12H), 2.28 (s, 15H), 2.11 (s, 6H), 2.04 (s, 30H), 1.94 (s, 15H), 1.85 (s, 6H), 1.74 (s, 6H), 1.70 (s, 6H). **^{13}C NMR** (C_6D_6, 100.5 MHz): δ = 163.7, 140.8, 138.5, 138.4, 138.1, 137.9, 137.3, 137.0, 136.2, 136.1, 132.8, 132.5, 131.5, 130.4, 129.7, 129.0, 128.9, 126.2, 126.0, 125.4, 124.8, 120.0, 22.2, 21.8, 21.8, 21.3, 20.7, 13.1, 12.9, additional signals due to isomerization. **^{31}P{^{1}H} NMR** (C_6D_6, 161.8 MHz): δ = 276.9 (s), 261.5 (d, 151 Hz), 260.9 (d, 143 Hz), 228.2 (d, 150 Hz), 225.7 (d, 143 Hz).

Note: additional signals due to CN-bridged biradical species are often observed at 228.5 (d, 7 Hz), 200.2 (d, 6 Hz), 170.4 (d, 47 Hz), which disappear after re-crystallization (see ^{31}P NMR spectra below).

Figure S13. ^{1}H, ^{13}C and ^{31}P NMR spectra of $Cp^*_2Ti(OArNCN_2P_2)_2$ (solvent signals indicated by asterisks).

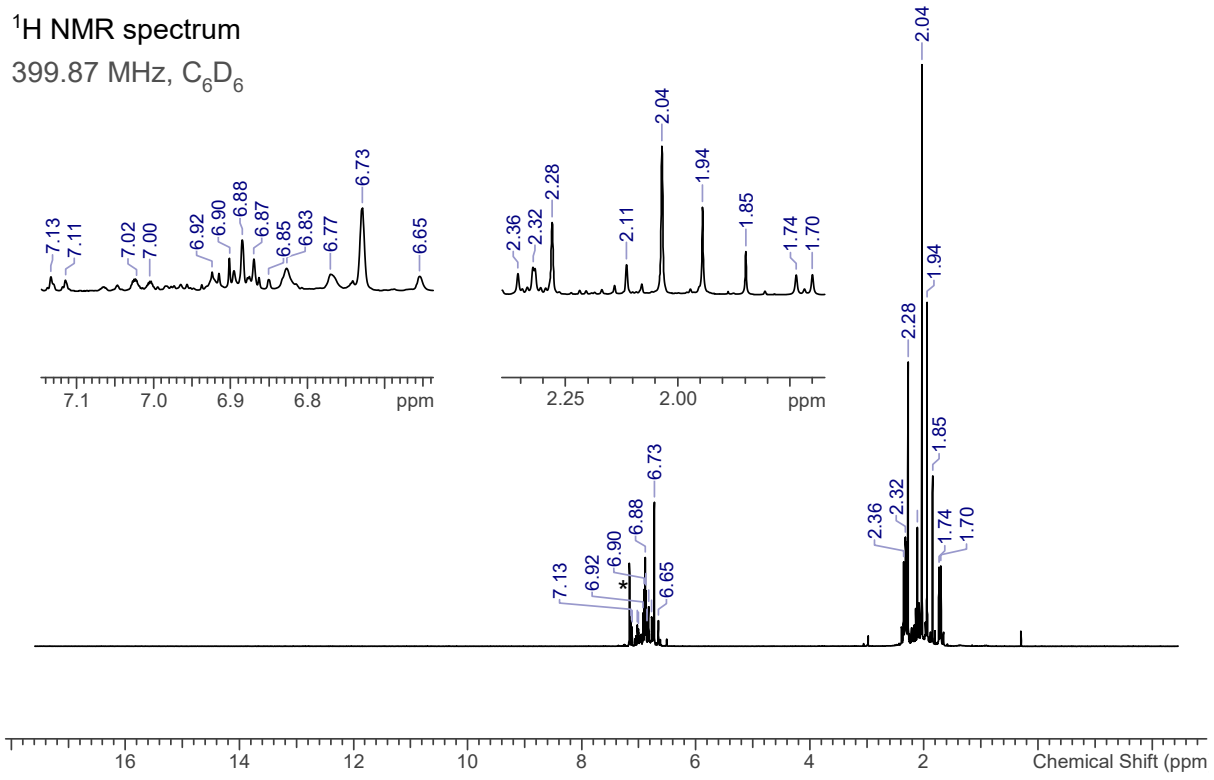

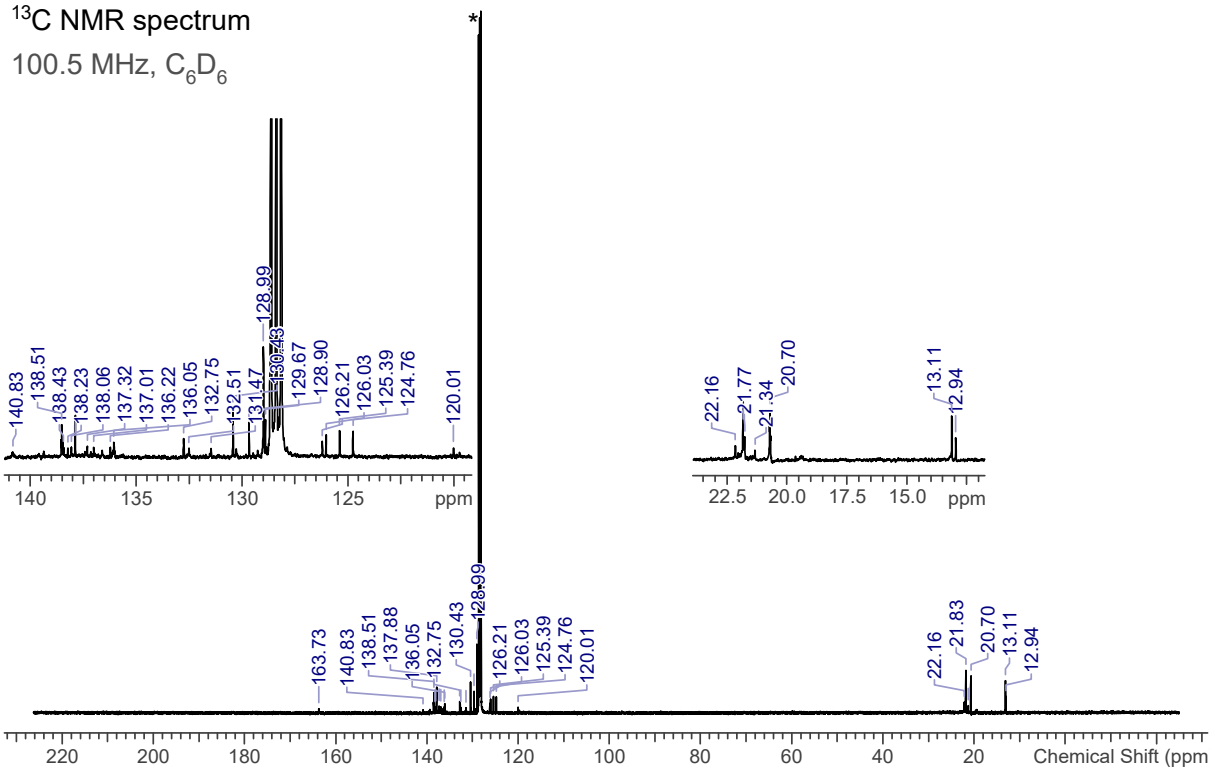

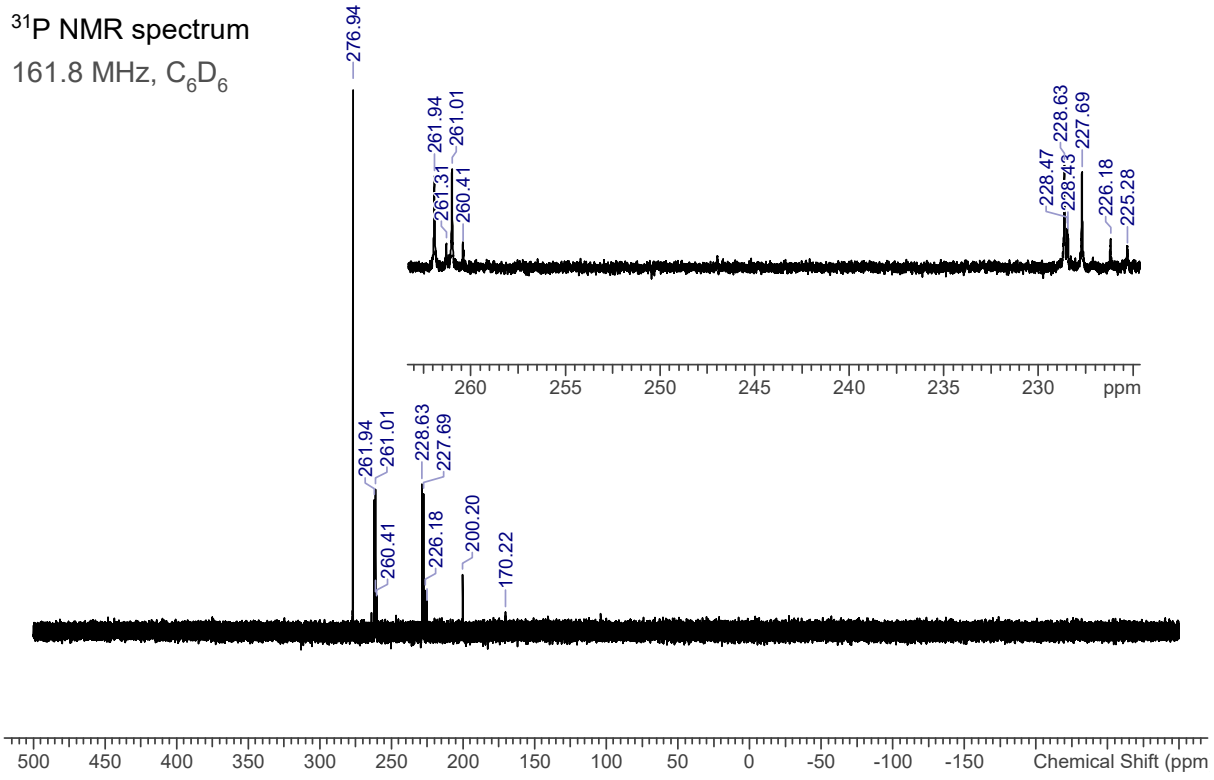

After re-crystallization

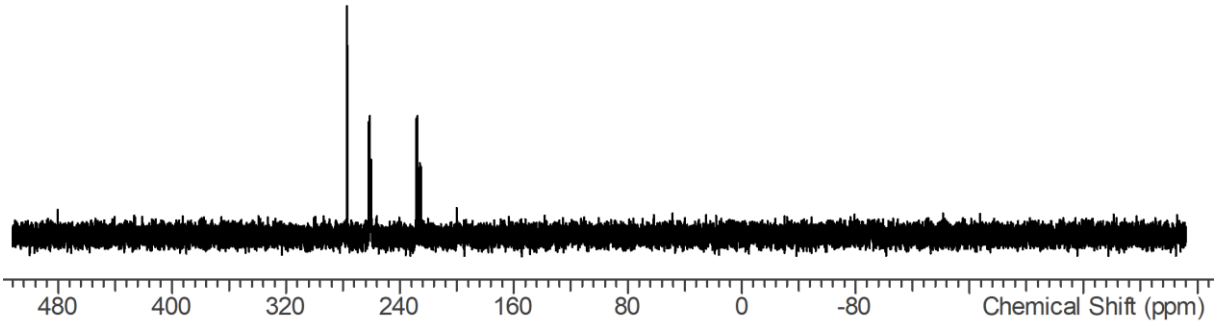
480
400
320
240
160
80
0
-80
Chemical Shift (ppm)

4.3 $Cp^*_2Zr(Cl)OArNCN_2P_2$

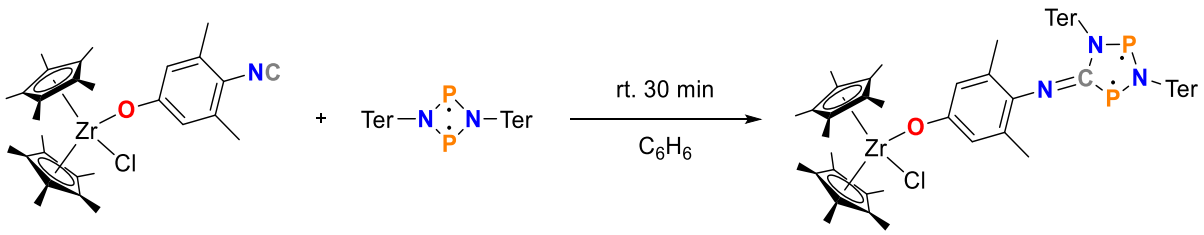

P_2N_2-Biradical (311 mg, 0.433 mmol) and $Cp_2Zr(Cl)OarNC$ (119 mg, 0.219 mmol) were combined, dissolved in benzene (10 mL), and the resulting dark green mixture was stirred at ambient temperature. After 30 minutes, the mixture was filtered via a P4-Schlenk frit. All volatile compounds were removed *in vacuo* (1×10^{-3} mbar), and the resulting green solid residue was dissolved in 3 mL toluene. The dark green solution was heated to 80 °C (oil bath), concentrated to approximately 2 mL, and cooled to ambient temperature in darkness. The solvent was removed *in vacuo* (1×10^{-3} mbar), and the remaining green product was thoroughly dried *in vacuo* (1×10^{-3} mbar) for two hours at ambient temperature (water bath). Yield: 247 mg (0,196 mmol, 71%).

^{1}H NMR (C_6D_6, 399.87 MHz): δ = 6.95 (s, 1H), 6.87 (s, 1H), 6.85 (s/m, 4H), 6.83 (s, 1H), 6.79 (s, 4H), 6.74 (s/m, 3H), 6,57 (s, 2H), 6.49 (s, 1H), 2.32 (s, 6H), 2.29 (s, 6H), 2.27 (s, 6H), 1.91 (s, 30H), 1.81 (s, 12H), 1.71 (s, 6H), 1.65 (s, 6H). **^{13}C NMR** (C_6D_6, 100.5 MHz): δ = 158.5, 138.5, 138.3, 137.9, 137.1, 136.6, 136.2, 132.6, 131.5, 130.4, 130.3, 129.0, 128.9, 124.8, 123.1, 122.4, 118.4, 117.7, 22.1, 21.7, 20.7, 12.2, 12.0, additional signals due to isomerization. **^{31}P{^{1}H} NMR** (C_6D_6, 161.8 MHz): δ = 276.9 (s), 261.8 (d, 148 Hz), 226.5 (d, 146 Hz).

Figure S14. ^{1}H, ^{13}C and ^{31}P NMR spectra of $Cp^*_2Zr(Cl)OArNCN_2P_2$ (solvent signals indicated by asterisks).

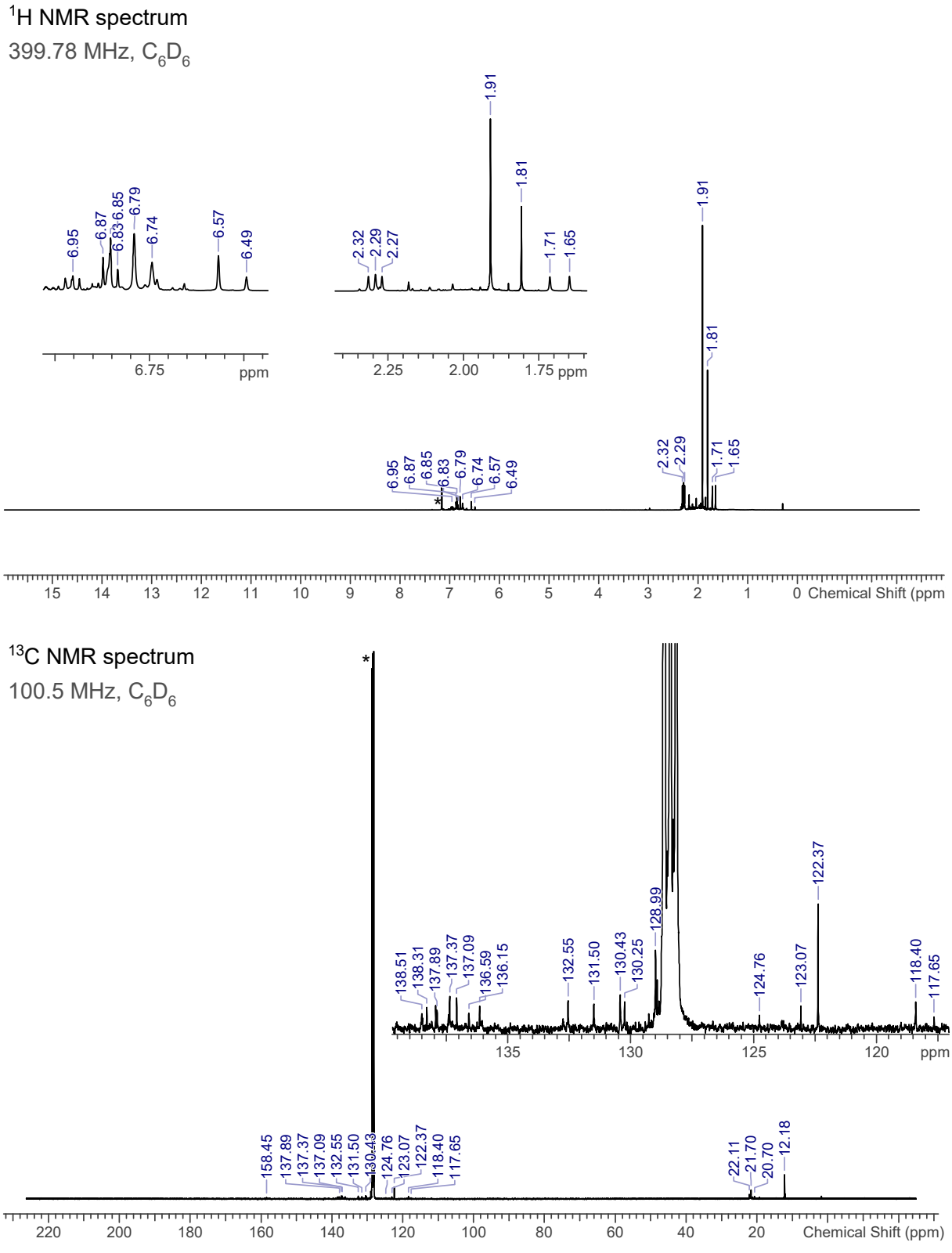

^{31}P NMR spectrum

161.8 MHz, C_6D_6

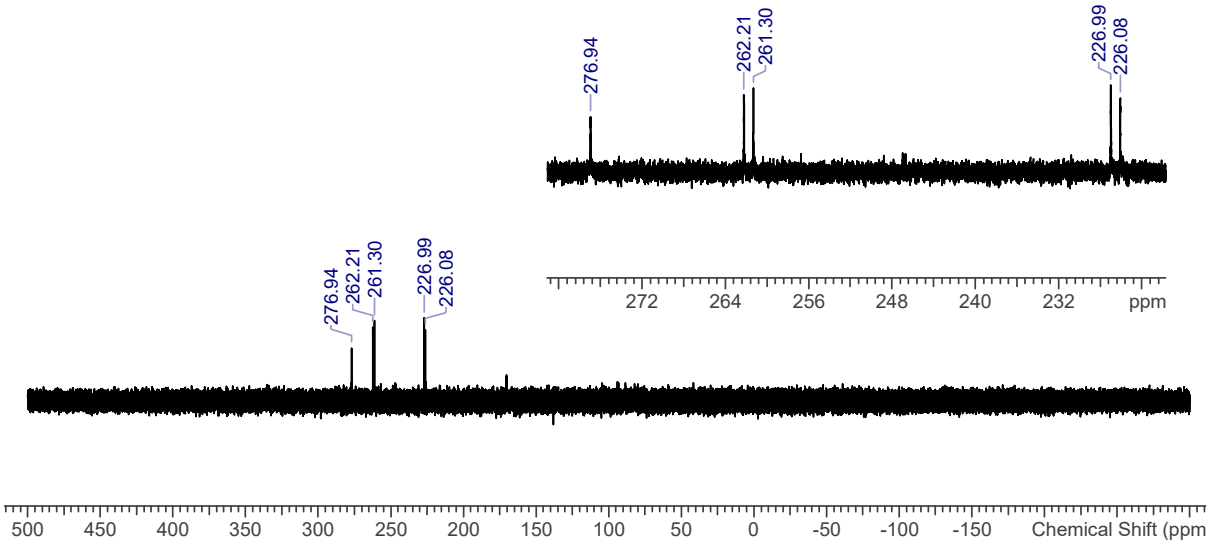

4.4 $Cp^*_2Zr(OArNCN_2P_2)_2$

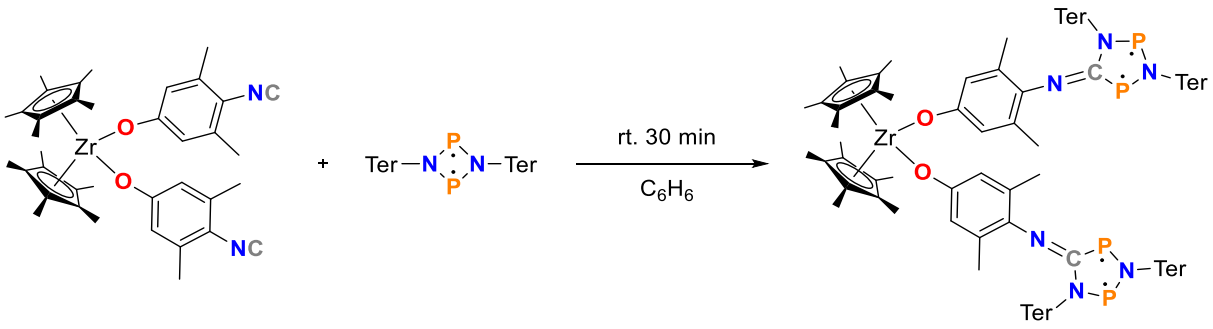

P_2N_2-Biradical (546 mg, 0.764 mmol) and $Cp_2Zr(OarNC)2$ (125 mg, 0.191 mmol) were combined, dissolved in benzene (10 mL), and the resulting dark green mixture was stirred at ambient temperature. After 30 minutes, the mixture was filtered via a P4-Schlenk frit. All volatile compounds were removed *in vacuo* (1×10^{-3} mbar) and the resulting green solid residue was dissolved in 3 mL toluene. The dark green solution was heated to 80 °C (oil bath), concentrated to approximately 2 mL, and cooled to ambient temperature in darkness. The solvent was removed *in vacuo* (1×10^{-3} mbar), and the remaining green product was thoroughly dried *in vacuo* (1×10^{-3} mbar) for two hours at ambient temperature (water bath). Yield: 336 mg (0,161 mmol, 70%).

^{1}H NMR (C_6D_6, 399.87 MHz): δ = 7.13 (s/m, 2H), 7.11 (s/m, 2H), 7.06 (s, 1H), 7.05 (s, 1H), 7.02 (s/m, 3H), 7.00 (s/m, 3H), 6.91 (m, 4H), 6.87-6.91 (m, 13H), 6.85 (s, 2H), 6.83 (m, 8H), 6.78 (s/m, 5H), 6.73 (s, 6H), 6.72 (s, 3H), 6.67 (s, 1H), 6.58 (s, 1H), 2.36 (s, 9H), 2.35 (m, 6H), 2.33 (d, 21H), 2.29 (m, 5H), 2.28 (s, 9H), 2.14 (s, 3H), 2.11 (s, 12H), 2.08 (s, 3H), 2.04 (s, 21H), 1.96 (s, 30H), 1.88 (s, 12H), 1.74 (d, 18H), 1.71 (d, 6H). **^{13}C NMR** (C_6D_6, 100.5 MHz): δ = 159.1, 138.5, 138.4, 138.1, 137.9, 137.4, 137.1, 136.2, 132.6, 131.5, 130.4, 129.7, 129.0, 128.9, 126.0, 124.8, 122.1, 121.5, 119.9, 22.2, 21.8, 21.8, 20.7, 12.2, 12.0, additional signals due to isomerization. **^{31}P{^{1}H} NMR** (C_6D_6, 161.8 MHz): δ = 276.9 (s), 262.0 (d, 150 Hz), 261.5 (d, 146 Hz), 227.7 (d, 149 Hz), 225.6 (d, 143 Hz).

Figure S15. ^{1}H, ^{13}C and ^{31}P NMR spectra of $Cp^*_2Zr(OArNCN_2P_2)_2$ (solvent signals indicated by asterisks).

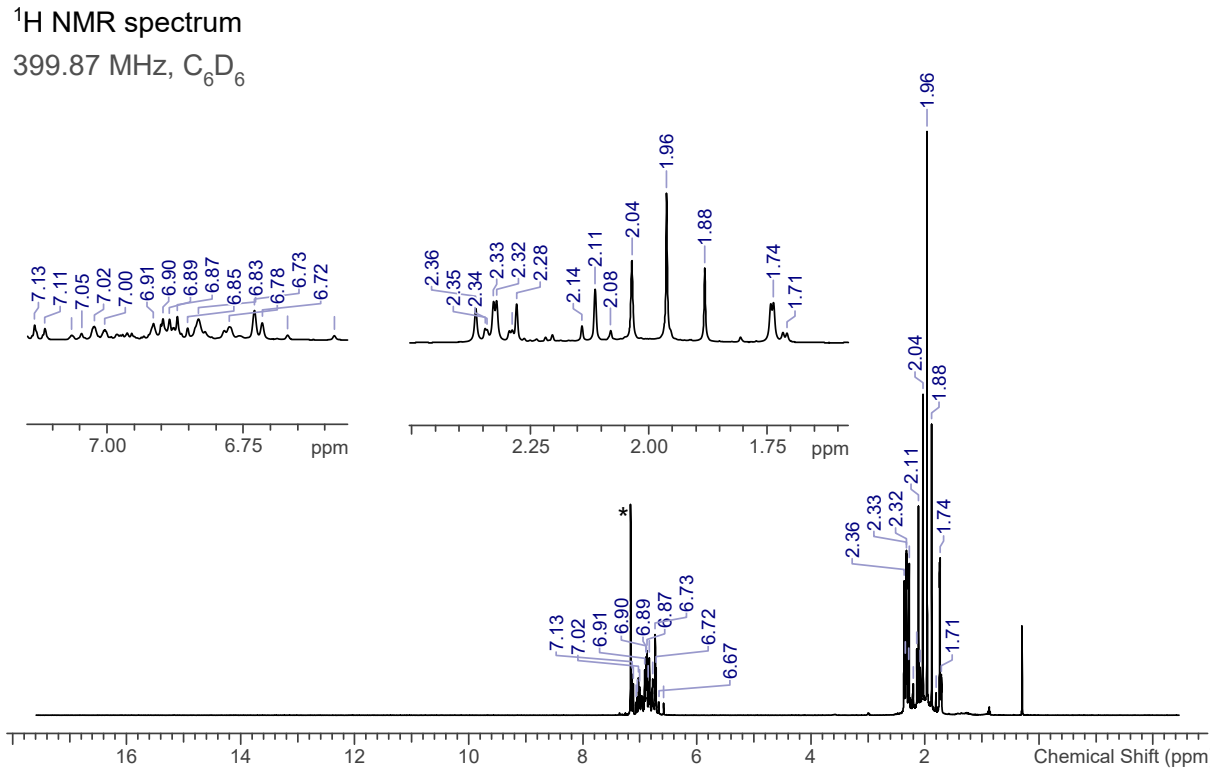

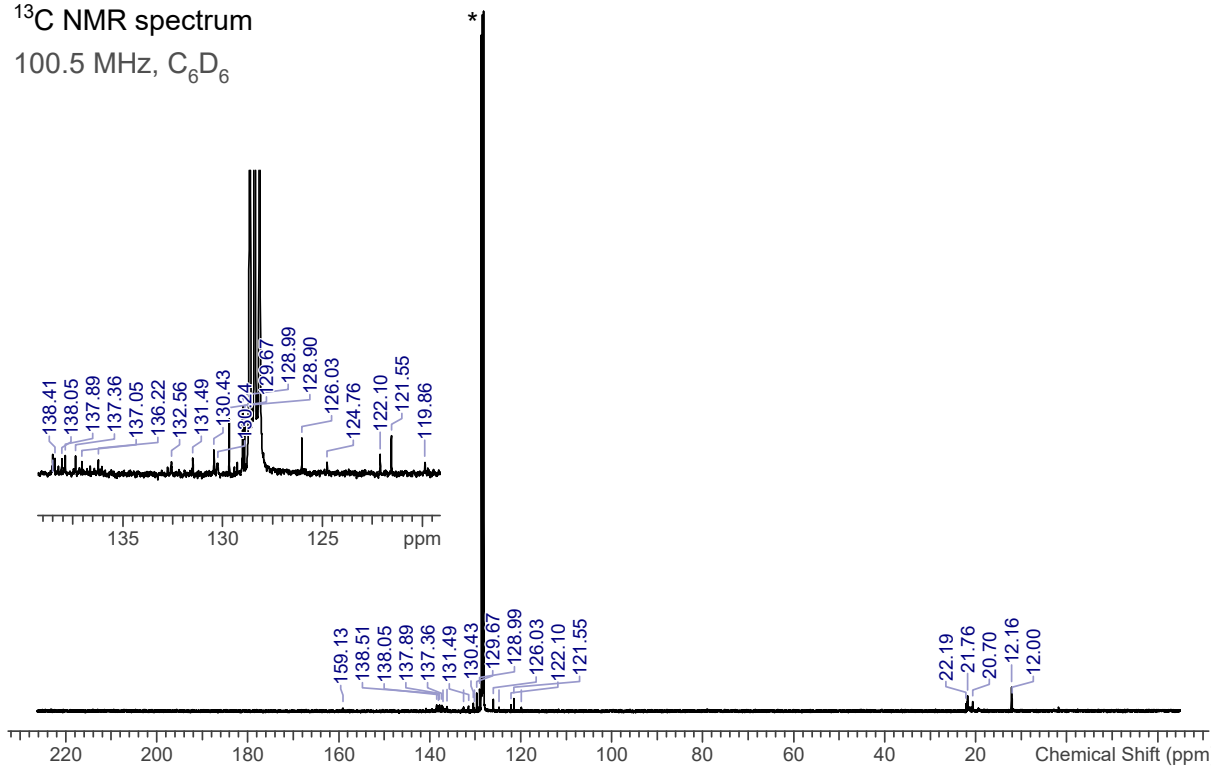

^{31}P NMR spectrum

161.8 MHz, C_6D_6

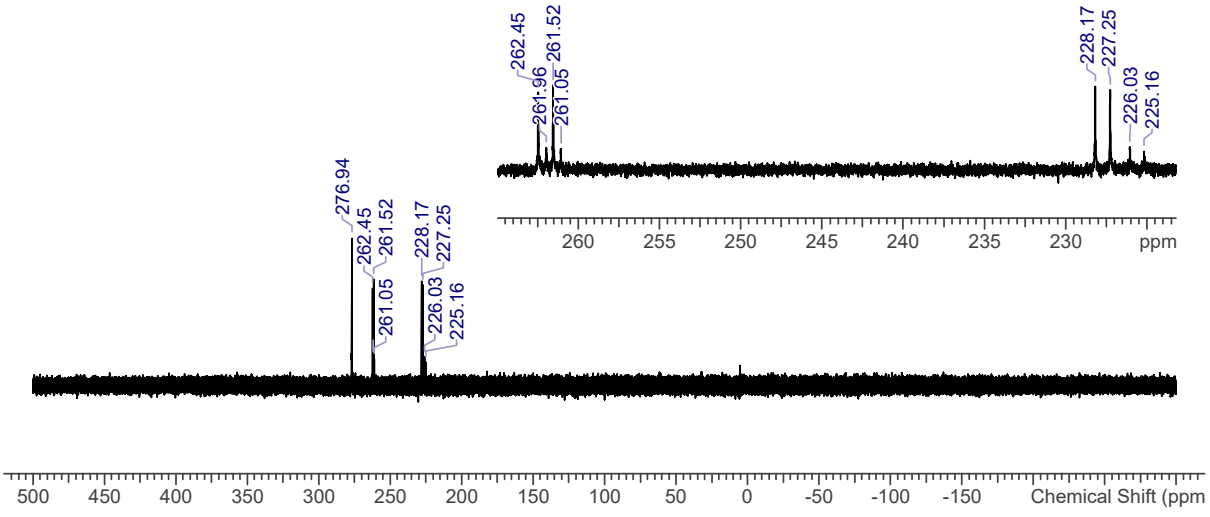

5 Irradiation experiments

5.1 UV/Vis experiments

5.1.1 Setup

To further study the behaviour of the herein investigated compounds under irradiation, we devised a setup for UV-vis measurements that fulfils the following parameters: The use of an inert atmosphere, setting constant, defined temperatures, and the possibility to irradiate the solution before and/or during measurements. We anticipated that the possibility of adding additional substrate or reagents via syringe might also prove advantageous.

Figure S16. Assembled setup for UV-vis experiments under irradiation at defined temperatures.

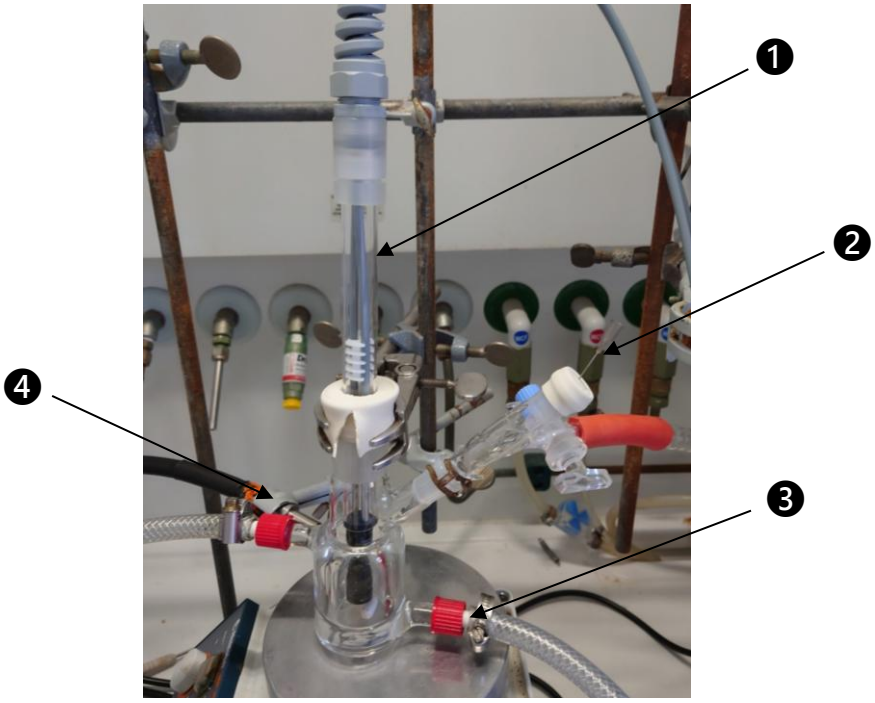

UV-vis experiments were carried out in a 2-necked measurement cell using an immersion probe (1). Before each experiment, the glassware was dried over night at 80 °C (drying oven) and while hot flushed with argon for 10 minutes. Afterwards, the optic element was put inside (fitted through the NS29 rubber septum), and the system

was flushed for a further 10 minutes with argon. A short venting cannula (2) was then placed on the side of the neck to ensure a constant stream of argon without exerting an overpressure on the system so as not to pop out the immersion probe. Housing for Temperature control (HAAKE C25P cooling unit, silicon oil SIL180 as coolant) was attached (3) and for irradiation experiments, a Ø8 mm light guide was placed perpendicular to the cell in no more than 5 mm distance (4).

Toluene was used as a solvent due to the solubility of the complex and slow evaporation in a stream of argon. The disadvantage of strong absorption in the UV region was accepted since the terphenyl substituents overcrowd this region anyways and we were more interested in the bands of the biradicaloid functionality (>350 nm).

NOTE: Unfortunately, the present experiments revealed that the species investigated were not stable over long periods of time in the apparatus described here. As a result, the measurements presented here only provide a rough insight into the thermal reversibility of the housane species into the respective biradicaloid species. For this reason, no kinetic data can be obtained from the time-resolved spectra.

5.1.2 UV-Vis measurements with and without irradiation

This chapter presents the UV-Vis spectra of the four complexes investigated. Furthermore, the biradicaloid species in the measuring cell were irradiated with light at a wavelength of 570 nm to convert them into their corresponding housane species. The UV-Vis spectrum of the respective housane species was then recorded from this sample. It should be noted here that, due to the equilibrium between the four-membered $Ter_2N_2P_2$ biradicaloid and the five-membered biradicaloid species presented here, additional absorption bands of the $Ter_2N_2P_2$ species (493 and 463 nm) can be found. Therefore, only the main absorption bands of the five-membered biradicaloid species around 655 nm can be evaluated with certainty.

Figure S17. Representation of the experimental irradiation experiments. Top: shows the investigated photoswitch (570 nm filter) from the $Cp^*_2Ti(Cl)OArNCN_2P_2$ to [Ti] mono-biradicaloid to the corresponding [Ti] mono-housane type complex. Middle: Representation of the individual component UV-Vis spectra of [Ti] mono-biradicaloid (maxima: 658, 444 nm) and [Ti] mono-housane (maxima: 600, 429 nm). Bottom: The thermal reverse reaction was examined at 20 °C. First, a sample was irradiated with light at a wavelength of 570 nm, converting the biradicaloid species into the housane structure. Then, a blank measurement was performed and a series of UV-Vis spectra were recorded over a period of time. The spectra shown here represent only a selection of the recorded data. The main band of the biradicaloid species at 658 nm increases over time, providing direct proof of the thermal reverse reaction. Unfortunately, due to the poor solubility and stability of this complex, the recorded spectra are not of a high enough quality to allow for a detailed examination of the data.

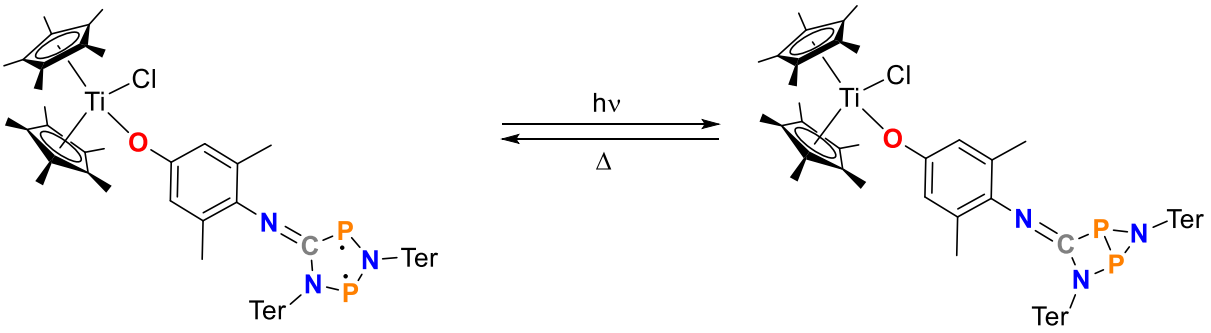

[Ti] mono-biradicaloid [Ti] mono-housane

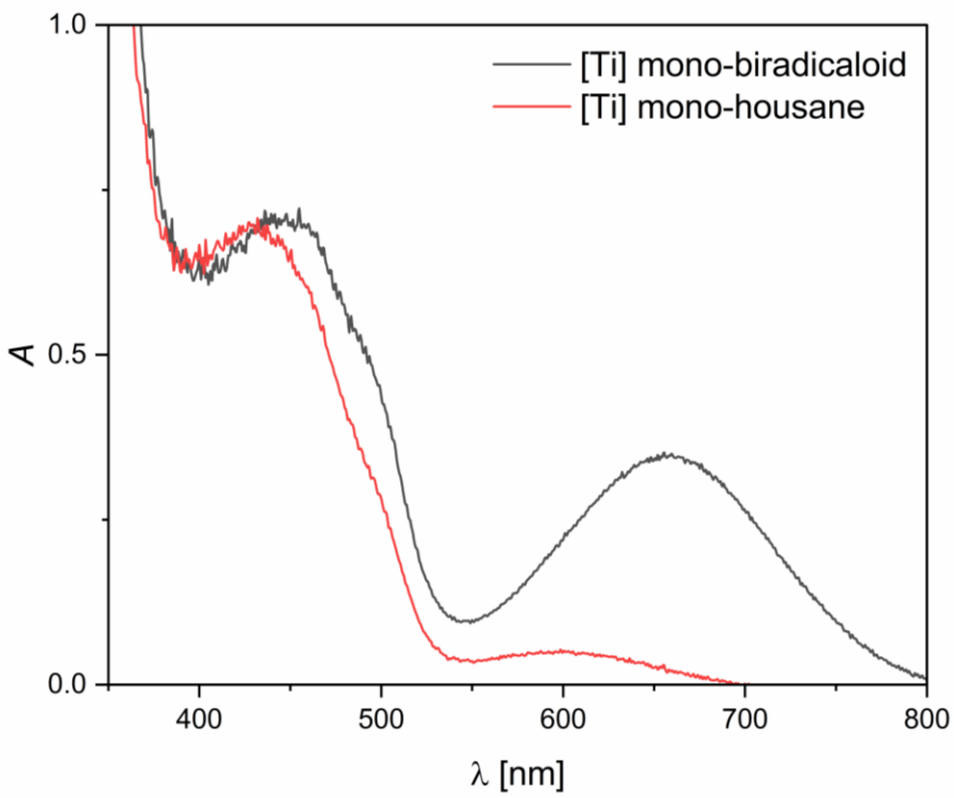
1.0
0.5
0.0
A
400
500
600
700
800
λ [nm]
[Ti] mono-biradicaloid
[Ti] mono-housane

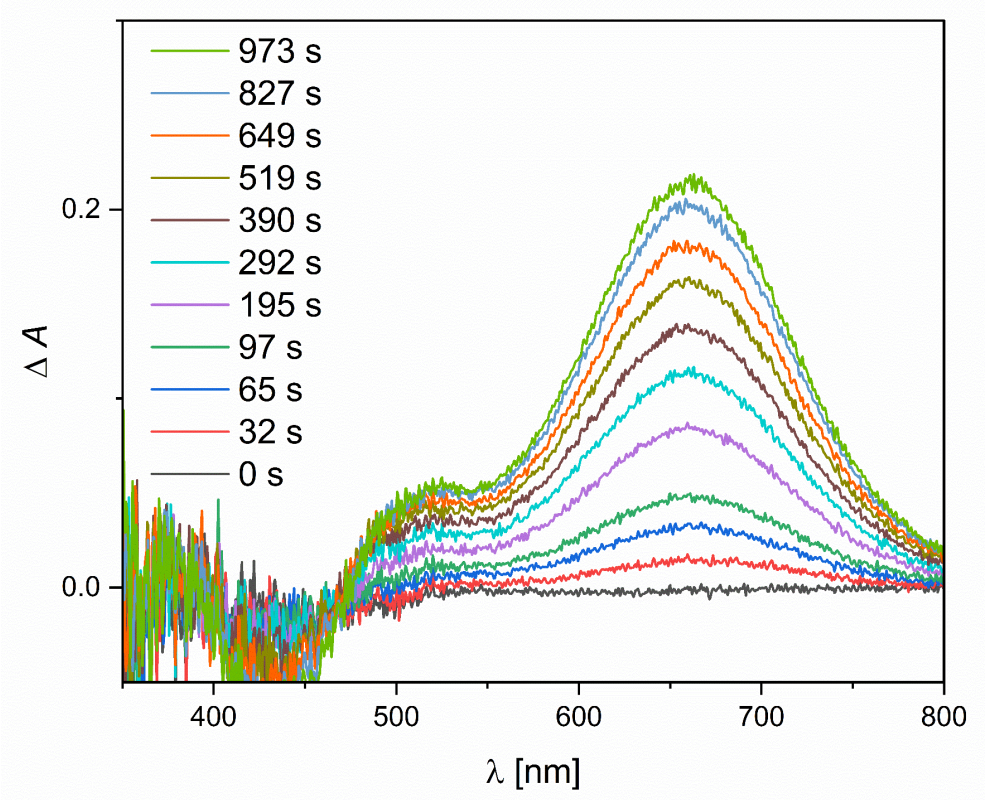
973 s
827 s
649 s
519 s
390 s
292 s
195 s
97 s
65 s
32 s
0 s
0.2
0.0
Δ A
400
500
600
700
800
λ [nm]

Figure S18. Representation of the experimental irradiation experiments. Top: shows the investigated photoswitch (570 nm filter) from the $Cp^*_2Ti(OArNCN_2P_2)_2$ to [Ti] bis-biradicaloid to the corresponding [Ti] bis-housane type complex. Middle: Representation of the individual component UV-Vis spectra of [Ti] bis-biradicaloid (maximum: 654 nm, the absorbance bands at 491 and 461 nm belong to $Ter_2N_2P_2$ biradicaloid) and [Ti] bis-housane (maxima: tailing between 550 and 650, the absorbance bands at 491 and 461 nm belong to Ter_2N_2P). Bottom: The thermal reverse reaction was examined at 20 °C. First, a sample was irradiated with light at a wavelength of 570 nm, converting the bis-biradicaloid species into the bis-housane structure. Then, a blank measurement was performed and a series of UV-Vis spectra were recorded over a period of time. The spectra shown here represent only a selection of the recorded data. The main band of the biradicaloid species at 654 nm increases over time, providing direct proof of the thermal reverse reaction. Unfortunately, due to the poor solubility and stability of this complex, the recorded spectra are not of a high enough quality to allow for a detailed examination of the data.

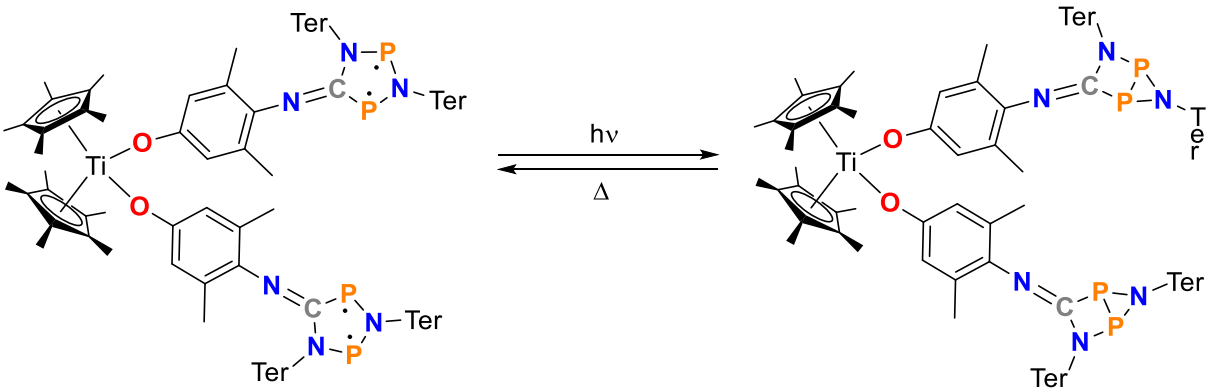

[Ti] bis-biradicaloid [Ti] bis-housane

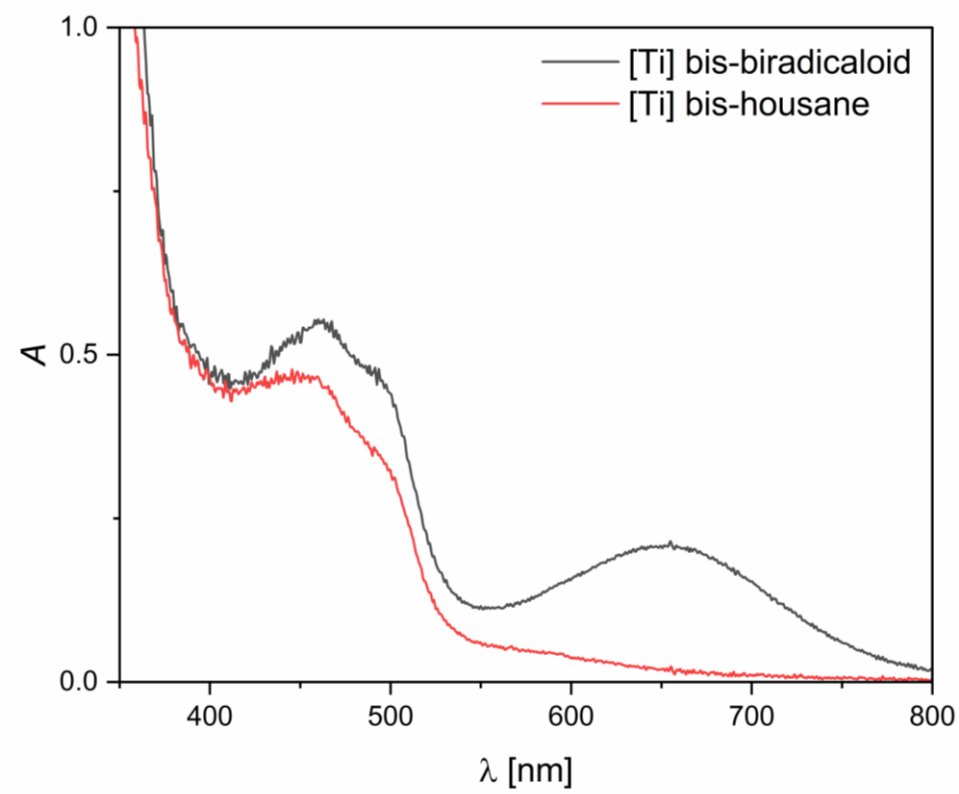
1.0
0.5
0.0
A
400
500
600
700
800
λ [nm]
[Ti] bis-biradicaloid
[Ti] bis-housane

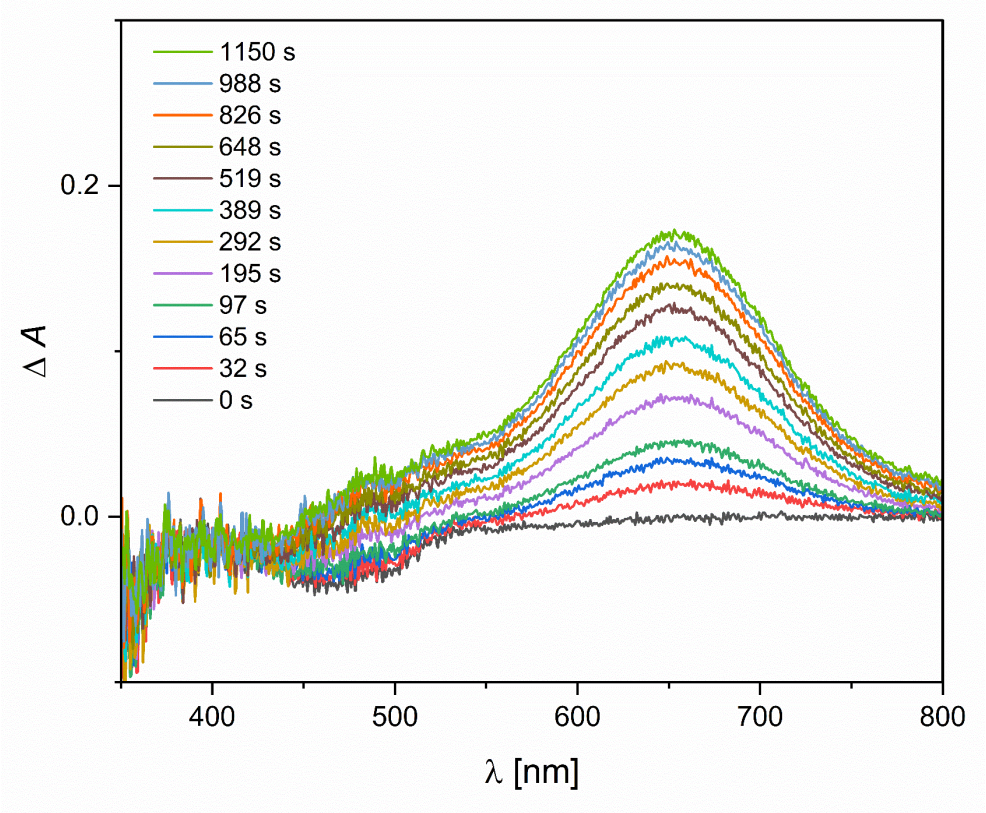
0.2
0.0
Δ A
400
500
600
700
800
λ [nm]
1150 s
988 s
826 s
648 s
519 s
389 s
292 s
195 s
97 s
65 s
32 s
0 s

Figure S19. Representation of the experimental irradiation experiments. Top: shows the investigated photoswitch (570 nm filter) from the $Cp^*_2Zr(Cl)OArNCN_2P_2$ to [Zr] mono-biradicaloid to the corresponding [Zr] mono-housane type complex. Middle: Representation of the individual component UV-Vis spectra of [Zr] mono-biradicaloid (maximum: 657, overlap of broad bands between 530 and 400 nm might belong to the absorbance bands of Ter_2N_2P at 493 and 463 nm) and [Zr] mono-housane (tailing between 550 and 350 nm). Bottom: The thermal reverse reaction was examined at 20 °C. First, a sample was irradiated with light at a wavelength of 570 nm, converting the biradicaloid species into the housane structure. Then, a blank measurement was performed and a series of UV-Vis spectra were recorded over a period of time. The spectra shown here represent only a selection of the recorded data. The main band of the biradicaloid species at 657 nm increases over time, providing direct proof of the thermal reverse reaction. Unfortunately, due to the poor solubility and stability of this complex, the recorded spectra are not of a high enough quality to allow for a detailed examination of the data.

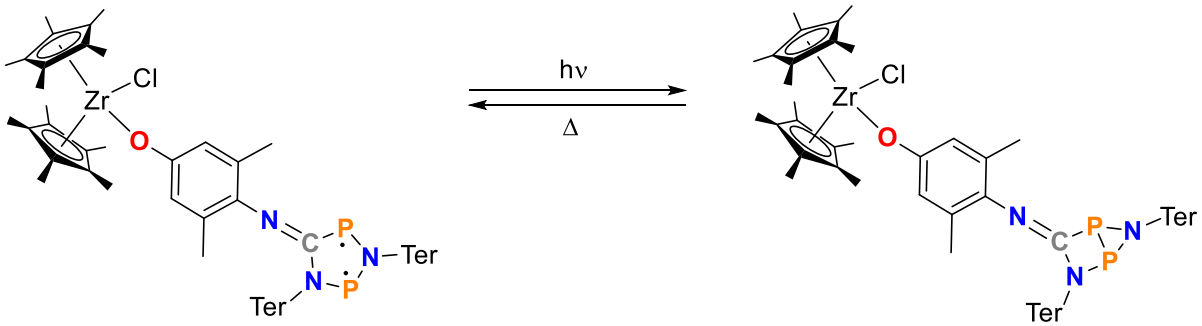

[Zr] mono-biradicaloid [Zr] mono-housane

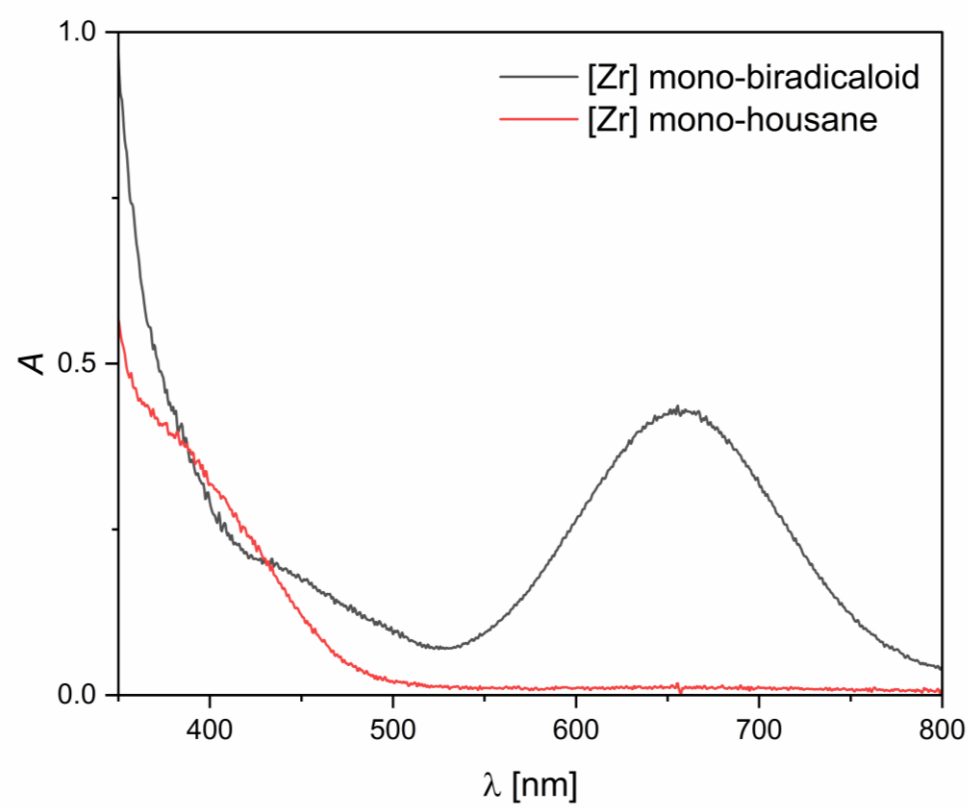
[Zr] mono-biradicaloid
[Zr] mono-housane
A
λ [nm]

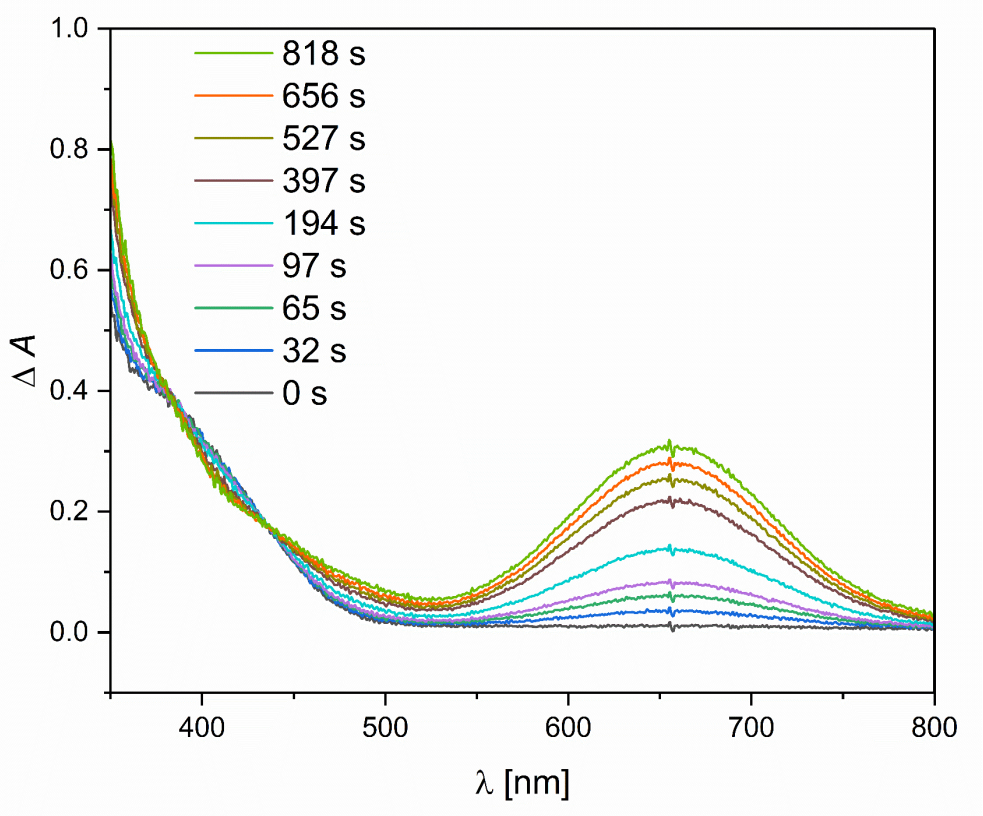
818 s
656 s
527 s
397 s
194 s
97 s
65 s
32 s
0 s
Δ A
λ [nm]

Figure S20. Representation of the experimental irradiation experiments. Top: shows the investigated photoswitch (570 nm filter) from the $Cp^*_2Zr(OArNCN_2P_2)_2$ to [Zr] bis-biradicaloid to the corresponding [Zr] bis-housane type complex. Middle: Representation of the individual component UV-Vis spectra of [Zr] bis-biradicaloid (maximum: 656, the absorbance bands at 493 and 463 nm belong to Ter_2N_2P) and [Zr] bis-housane (tailing between 550 and 400 nm might belong to the absorbance bands of Ter_2N_2P at 493 and 463 nm). Bottom: The thermal reverse reaction was examined at 20 °C. First, a sample was irradiated with light at a wavelength of 570 nm, converting the bis-biradicaloid species into the bis-housane structure. Then, a blank measurement was performed and a series of UV-Vis spectra were recorded over a period of time. The spectra shown here represent only a selection of the recorded data. The main band of the biradicaloid species at 658 nm increases over time, providing direct proof of the thermal reverse reaction. Unfortunately, due to the poor solubility and stability of this complex, the recorded spectra are not of a high enough quality to allow for a detailed examination of the data.

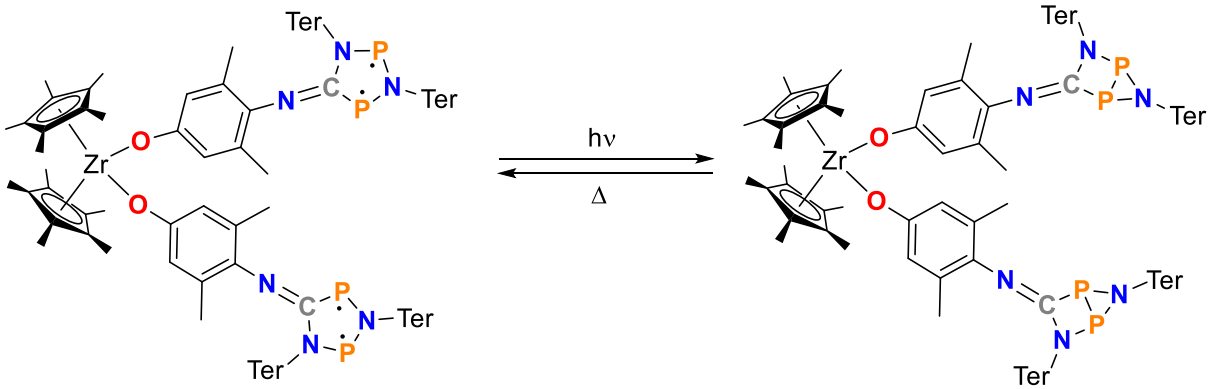

[Zr] bis-biradicaloid [Zr] bis-housane

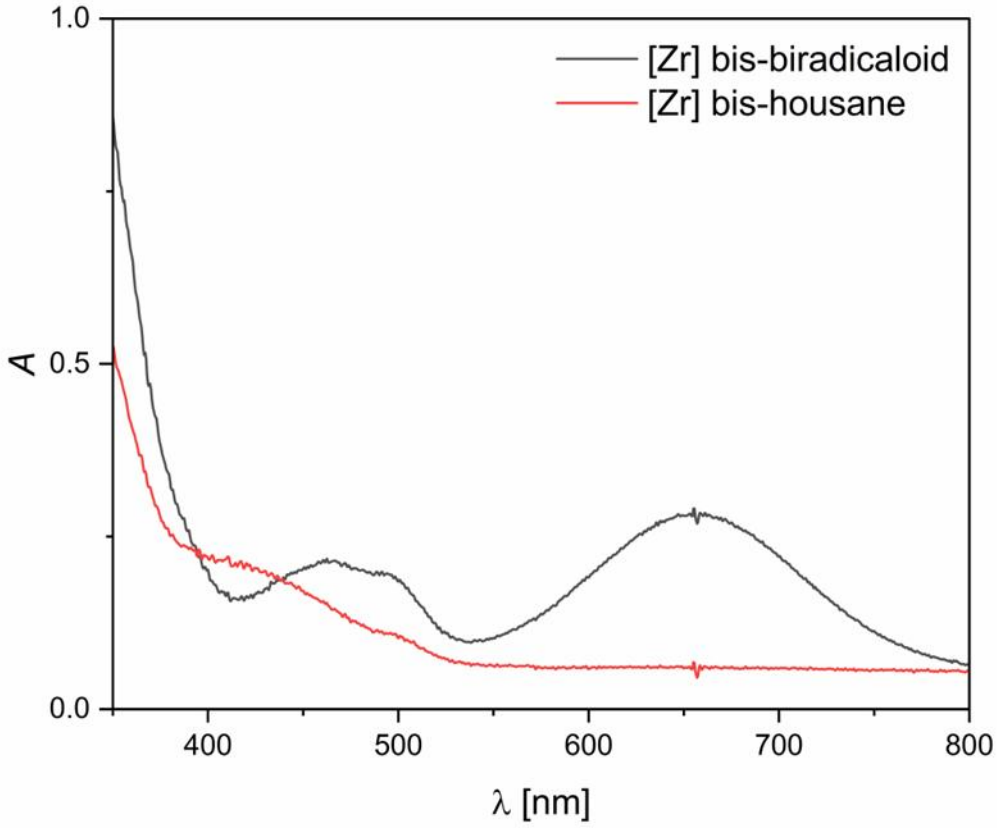
1.0
0.5
0.0
A
400
500
600
700
800
λ [nm]
[Zr] bis-biradicaloid
[Zr] bis-housane

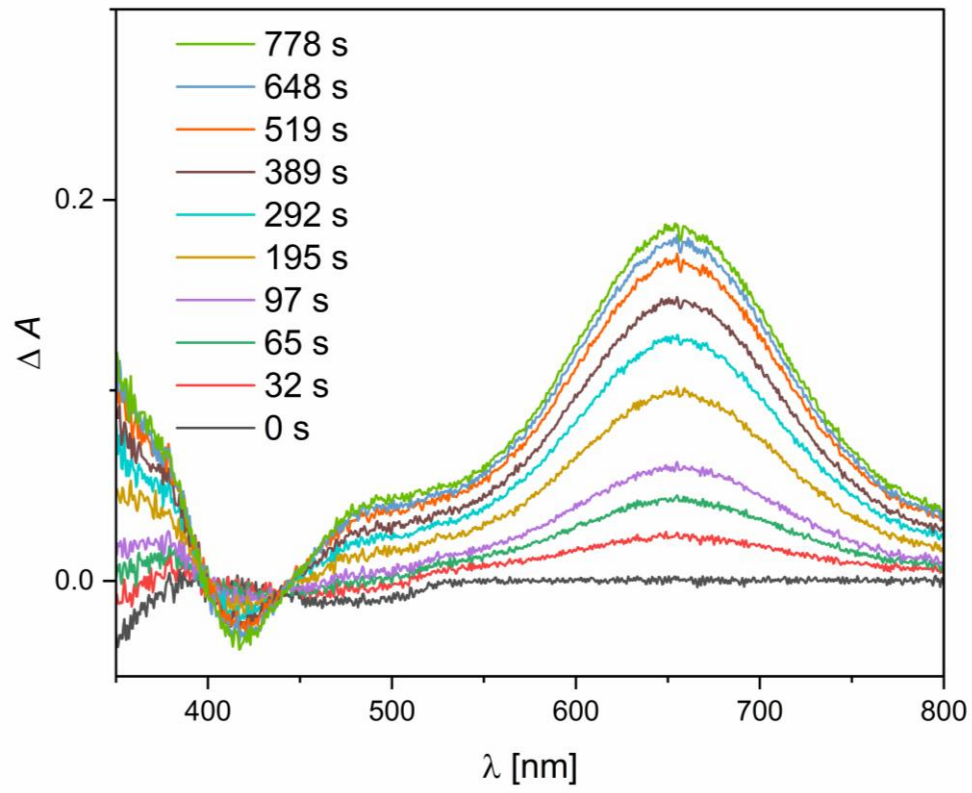
0.2
0.0
Δ A
400
500
600
700
800
λ [nm]
778 s
648 s
519 s
389 s
292 s
195 s
97 s
65 s
32 s
0 s

5.2 NMR experiment

5.2.1 Titanocene mono-switch

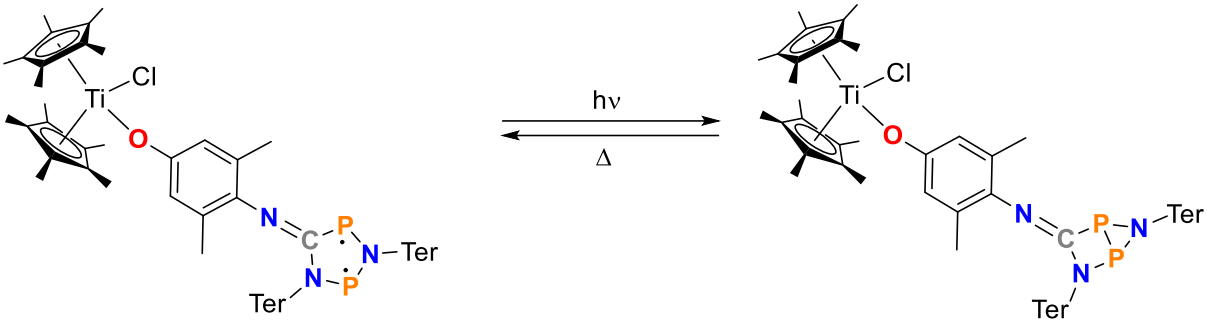

11.0 mg (0.015 mmol) of four-membered biradical $[TerNP]_2$ + 6.1 mg (0.012 mmol) of titanocene-mono-linker were mixed as solids in an NMR tube suitable for irradiation. Then 0.3 mL of C_6D_6 was added, and the solution was left in the NMR tube in the glovebox for 12 h for better solubility of starting materials. An irradiation experiment was conducted at 161.3 MHz at room temperature with a red laser diode (638 nm).

Figure S21. $^{31}P\{^1H\}$ NMR spectra before (bottom), during (middle), and 30min after irradiation (top).

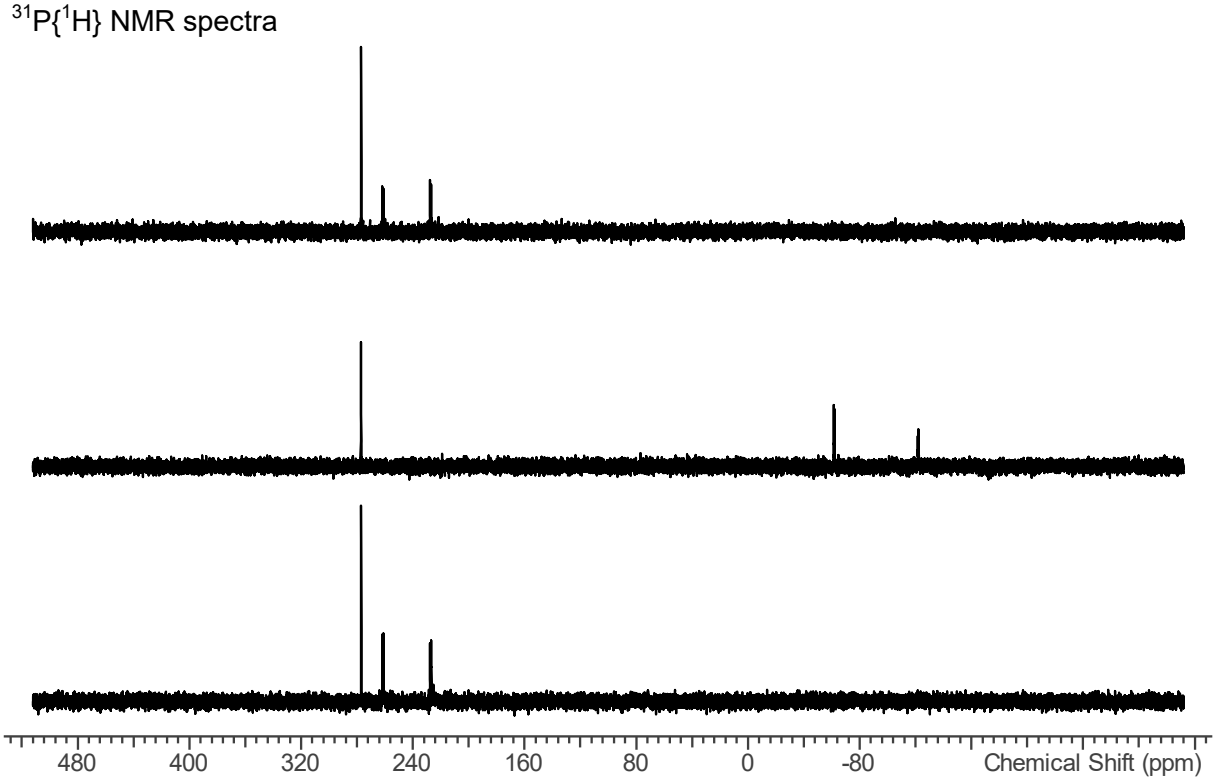

$^{31}P\{^{1}H\}$ NMR spectra: - br. S. at 276.95 ppm ($[TerNP]_2$)

- br. D. at 261.47 ppm (five-membered biradical) J = 149 Hz

- br. D. at 227.23 ppm (five-membered biradical) J = 149 Hz

- br. D. at −61.62 ppm (housane) J = 70 Hz

- br. D. at −121.87 ppm (housane) J = 70 Hz

δ = 276.9 (s), 261.5 (d, 148 Hz), 227.2 (d, 148 Hz); additional signals due to CN-bridged biradical species: 246.8 (d, 48 Hz), 228.5 (d, 6 Hz), 200.2 (d, 6 Hz), 170.4 (d, 47 Hz).

Figure S22. ^{1}H NMR spectra before (bottom), during (middle), and after irradiation (top). Solvent signals indicated by asterisks.

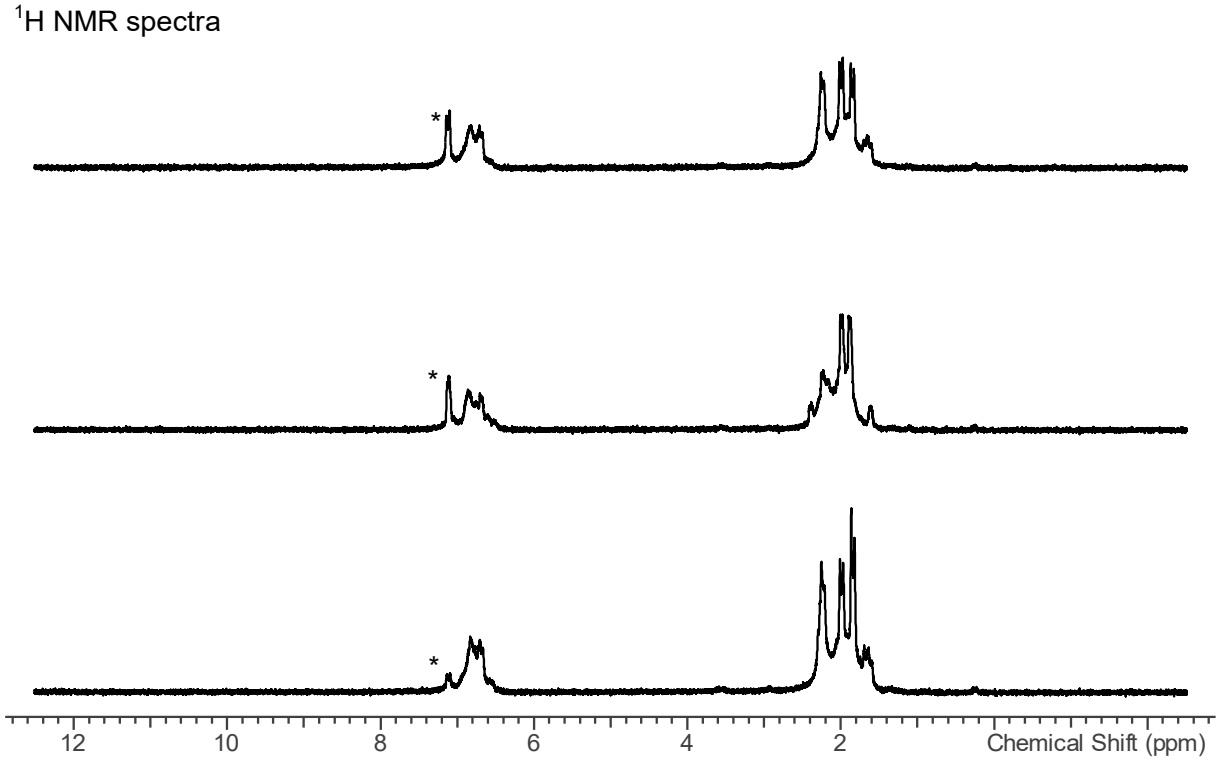

5.2.2 Titanocene double-switch

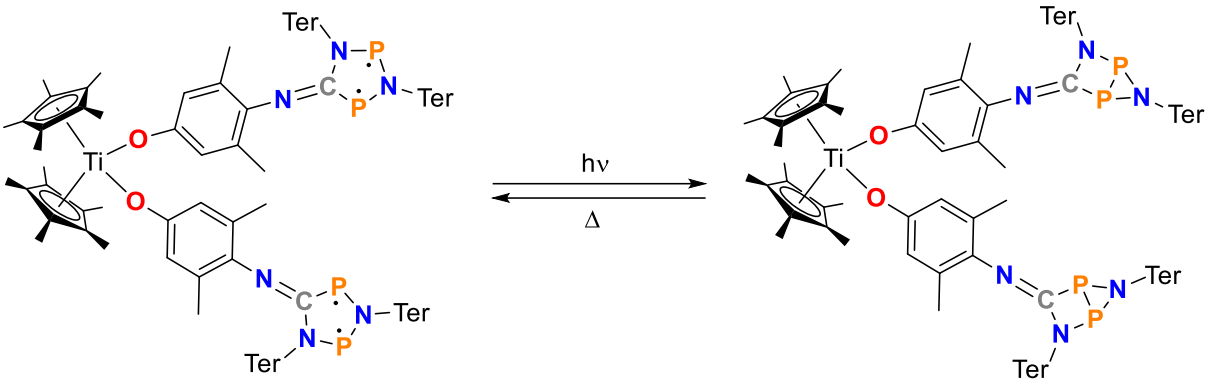

11.7 mg (0.0164 mmol) of four-membered biradical $[TerNP]_2$ + 5.0 mg (0.0082 mmol) of titanocene-double-linker were mixed as solids in an NMR tube suitable for irradiation. Then 0.3 mL of C_6D_6 was added, and the solution was left in the NMR tube in the glovebox for 12 h for better solubility of starting materials. Irradiation experiment conducted at 161.3 MHz at room temperature with a red laser diode (638 nm).

Figure S23. $^{31}P\{^1H\}$ NMR spectra before (bottom), during (middle), and after irradiation (top).

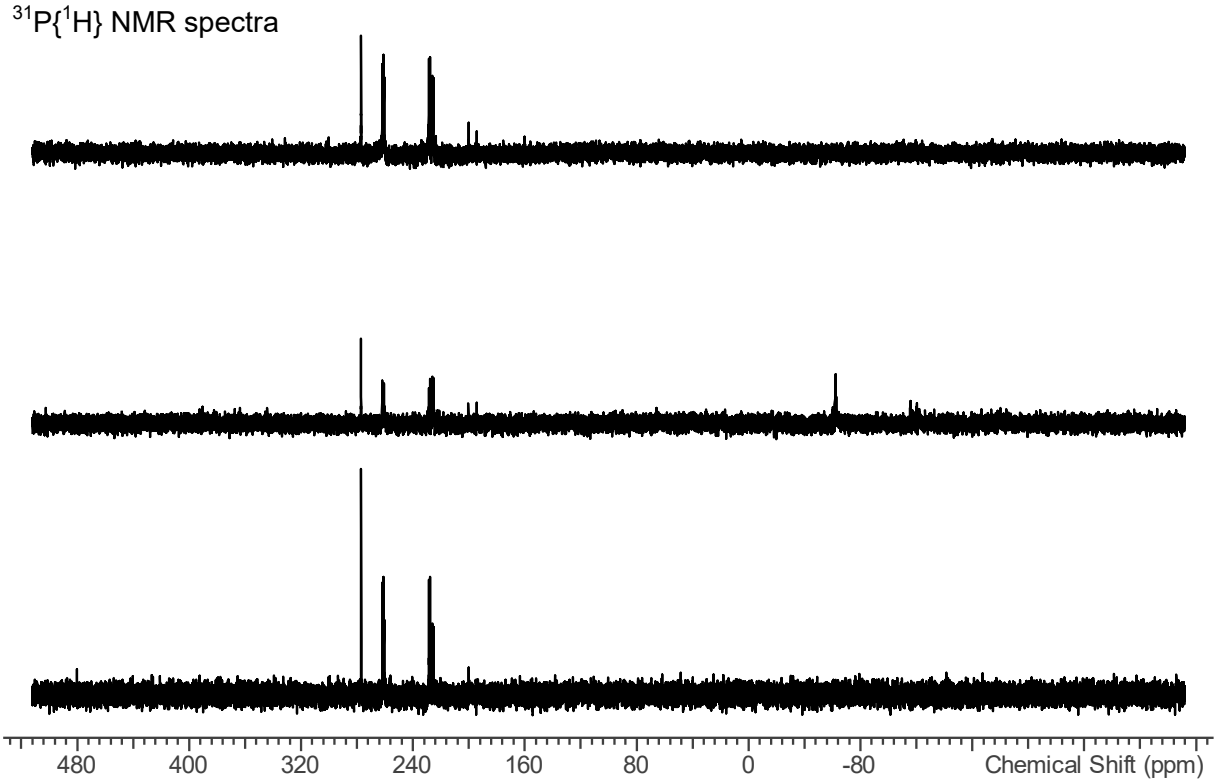

$^{31}P\{^{1}H\}$ NMR spectra: - br. S. at 276.95 ppm ($[TerNP]_2$)

- br. D. at 261.43 ppm (five-membered biradical, ring 1) J = 150 Hz

- br. D. at 260.91 ppm (five-membered biradical, ring 2) J = 145 Hz

- br. D. at 228.15 ppm (five-membered biradical, ring 1) J = 150 Hz

- br. D. at 225.71 ppm (five-membered biradical, ring 2) J = 145 Hz

- multiplet at −62.28 ppm (housane)

- multiplet at −117.95 ppm (housane)

After irradiation, more of the five-membered biradical in solution than before the irradiation. Shift of the equilibrium. During and after irradiation, additional signals (200.09 ppm and 194.40 ppm), probably due to slight impurities in the starting material or decomposition.

Figure S24. ^{1}H NMR spectra before (bottom), during (middle), and after irradiation (top). Solvent signals indicated by asterisks.

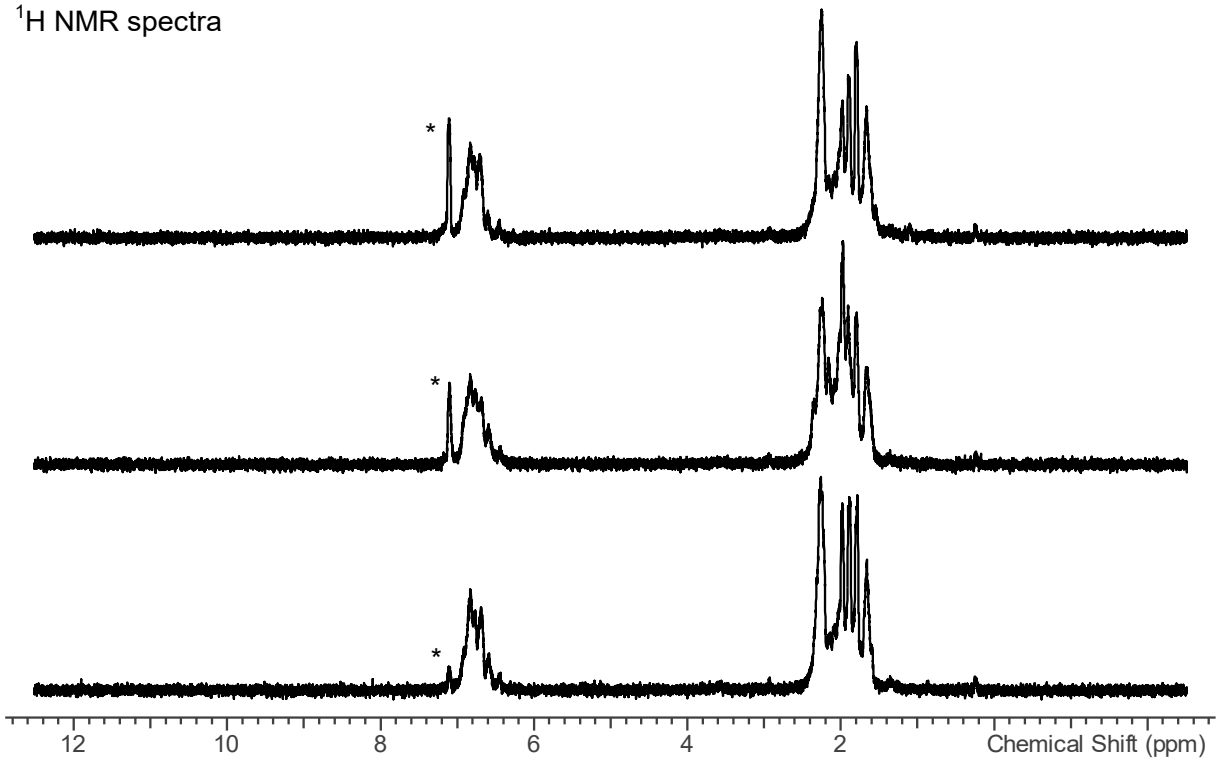

5.2.3 Zirconocene mono-switch

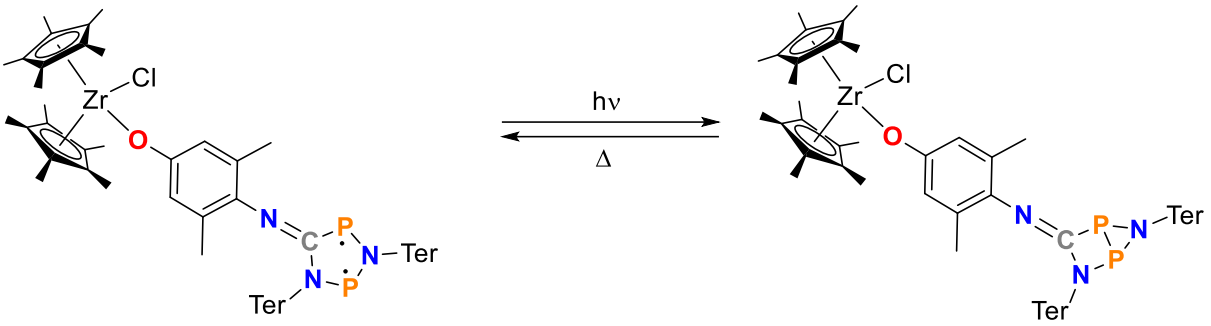

3.89 mg (0.0054 mmol) of four-membered biradical $[TerNP]_2$ + 2.95 mg (0.0054 mmol) of zirconocene-mono-linker were mixed as solids in an NMR tube suitable for irradiation. Then 0.3 mL of C_6D_6 was added. Irradiation experiment conducted at 161.3 MHz at room temperature with a red laser diode (638 nm).

Figure S25. $^{31}P\{^1H\}$ NMR spectra before (bottom), during (middle), and after irradiation (top).

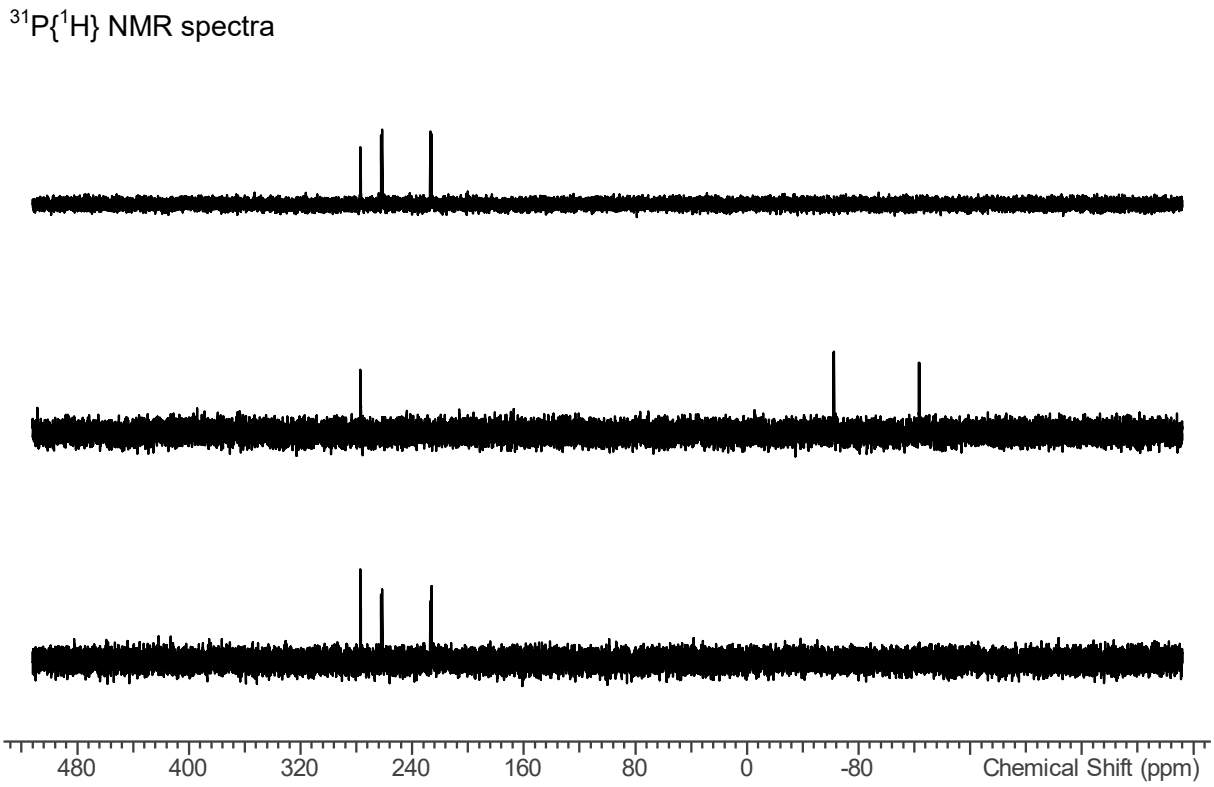

$^{31}P\{^{1}H\}$ NMR spectra: - br. S. at 276.95 ppm ($[TerNP]_2$)

- br. D. at 261.76 ppm (five-membered biradical) J = 145 Hz

- br. D. at 226.54 ppm (five-membered biradical) J = 146 Hz

- br. D. at −62.27 ppm (housane) J = 71 Hz

- br. D. at −123.55 ppm (housane) J = 71 Hz

After irradiation, more of the five-membered biradical in solution than before the irradiation. Shift of the equilibrium.

Figure S26. ^{1}H NMR spectra before (bottom), during (middle), and after irradiation (top). Solvent signals indicated by asterisks.

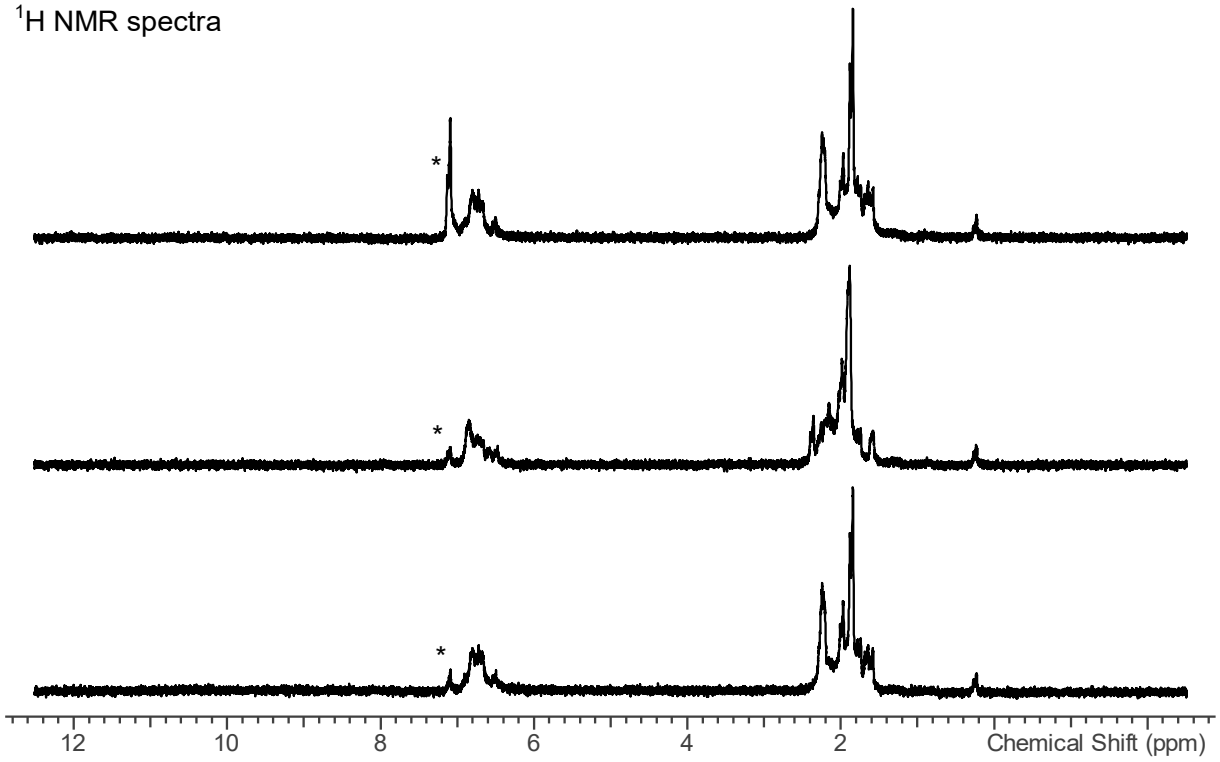

5.2.4 Zirconocene double-switch

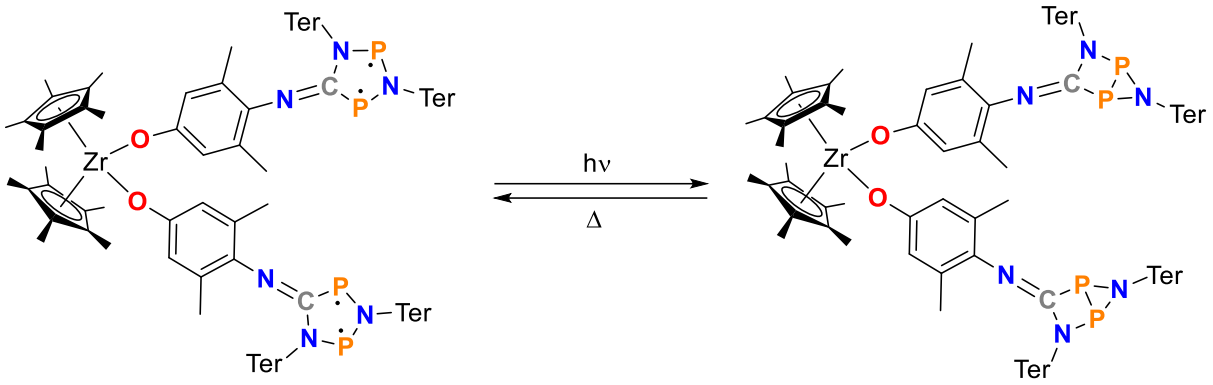

20.93 mg (0.029 mmol) of four-membered biradical $[TerNP]_2$ + 9.55 mg (0.015 mmol) of zirconocene-double-linker were mixed as solids in an NMR tube suitable for irradiation. Then, 0.3 mL of C_6D_6 added. An irradiation experiment was conducted at 161.3 MHz at room temperature with red laser diode (638 nm).

Figure S27. $^{31}P\{^1H\}$ NMR spectra before (bottom), during (middle) and after irradiation (top).

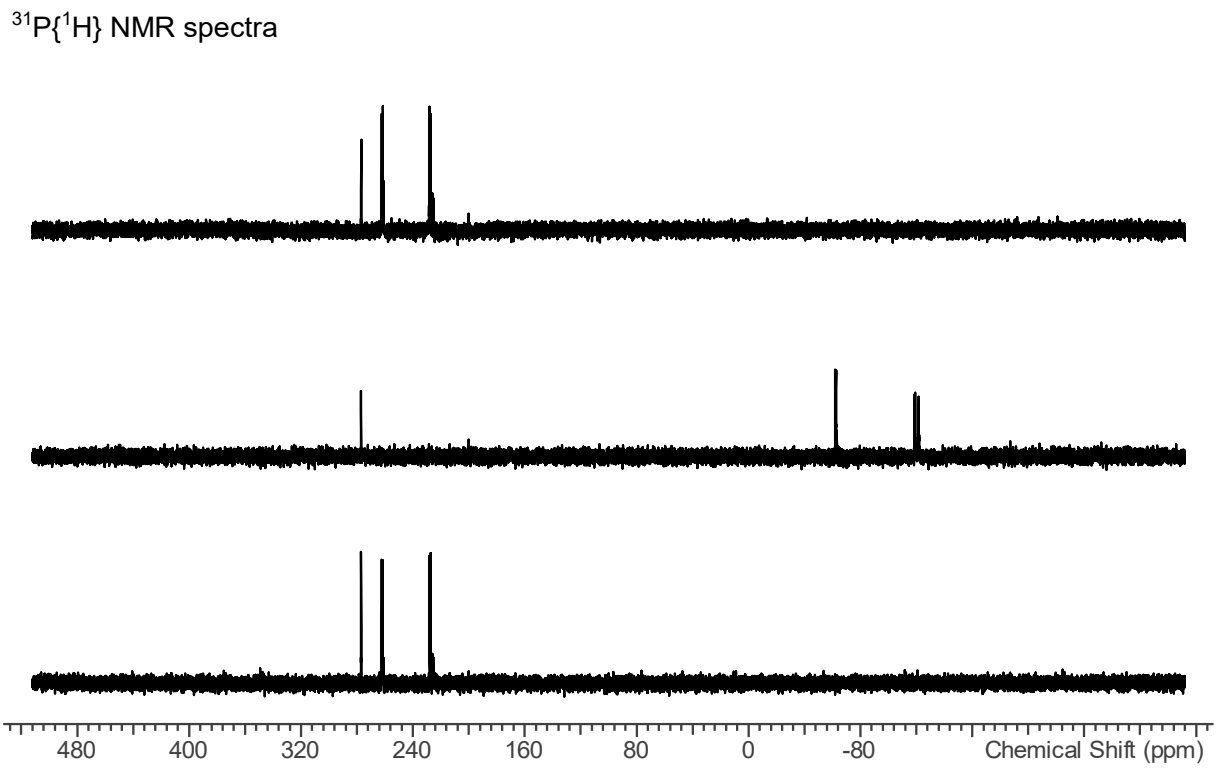

$^{31}P\{^{1}H\}$ NMR spectra: - br. S. at 276.95 ppm ($[TerNP]_2$)

- br. D. at 261.99 ppm (five-membered biradical, ring 1) J = 150 Hz

- br. D. at 261.51 ppm (five-membered biradical, ring 2) J = 145 Hz

- br. D. at 227.70 ppm (five-membered biradical, ring 1) J = 150 Hz

- br. D. at 225.55 ppm (five-membered biradical, ring 2) J = 145 Hz

- br. D. at −62.33 ppm (housane 1) J = 72 Hz

- br. D. at −62.42 ppm (housane 2) J = 70 Hz

- br. D. at −119.02 ppm (housane 1) J = 71 Hz

- br. D. at −121.35 ppm (housane 2) J = 71 Hz

After irradiation, more of the five-membered biradical in solution than before the irradiation. Shift of the equilibrium. During and after irradiation, additional signals (200.21 ppm), probably due to slight impurities in the starting material or decomposition.

Figure S28. ^{1}H NMR spectra before (bottom), during (middle), and after irradiation (top). Solvent signals indicated by asterisks.

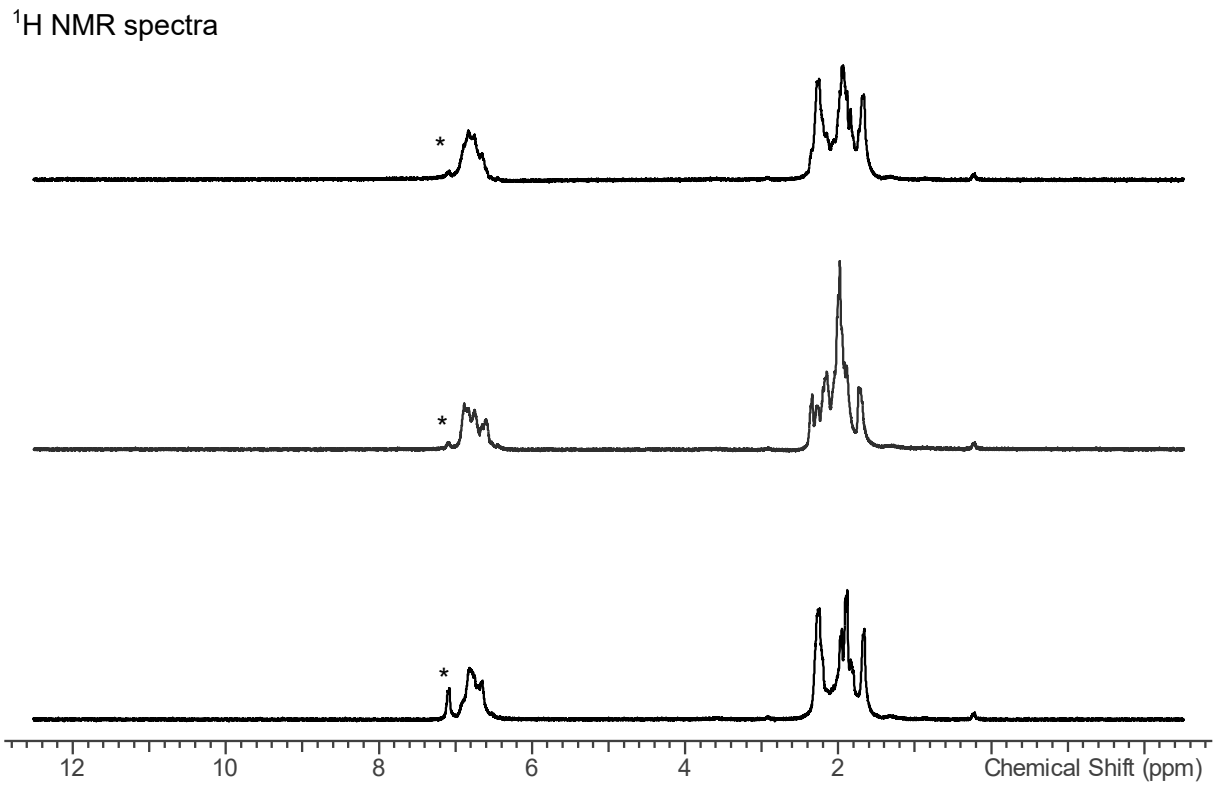

6 CO_2 activation chemistry

6.1 Zirconocene tetraradical + CO_2 (without irradiation)

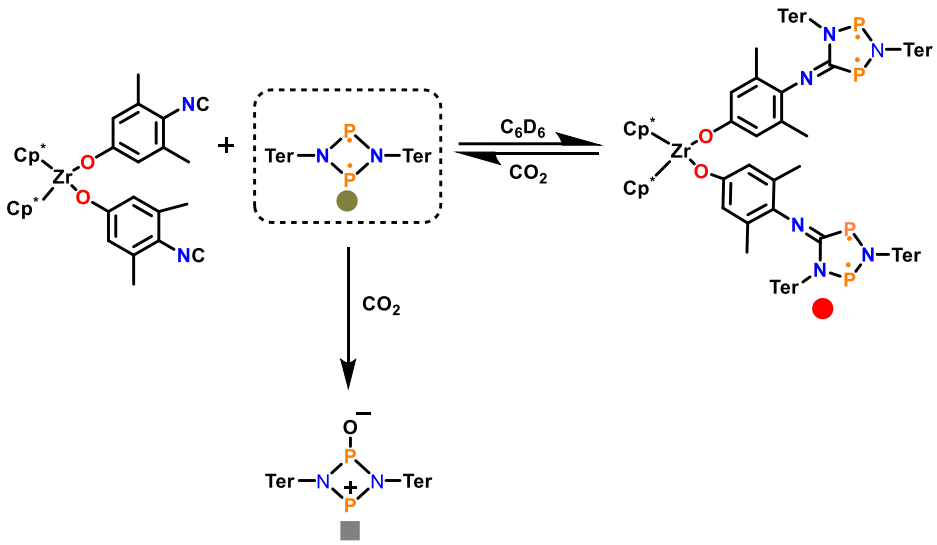

10.97 mg (0.015 mmol) of 4-membered biradical $[TerNP]_2$ + 5 mg (0.0076 mmol) of Zirconocene-monolinker were mixed as solids in a Young NMR tube. Then, 0.5 mL of C_6D_6 was added to the NMR tube in the glove box, and the solution was shaken for better solubility, and ^{31}P NMR was recorded.

Later the solution was degassed once, and CO_2 was added under constant flow for 9-10 seconds in the CO_2 Schlenk line. And ^{31}P NMR spectra at room temperature were recorded subsequently, as shown.

Figure S29. $^{31}P\{H\}$ NMR spectra, 161.83 MHz, C_6D_6, 128 scans, 25 °C

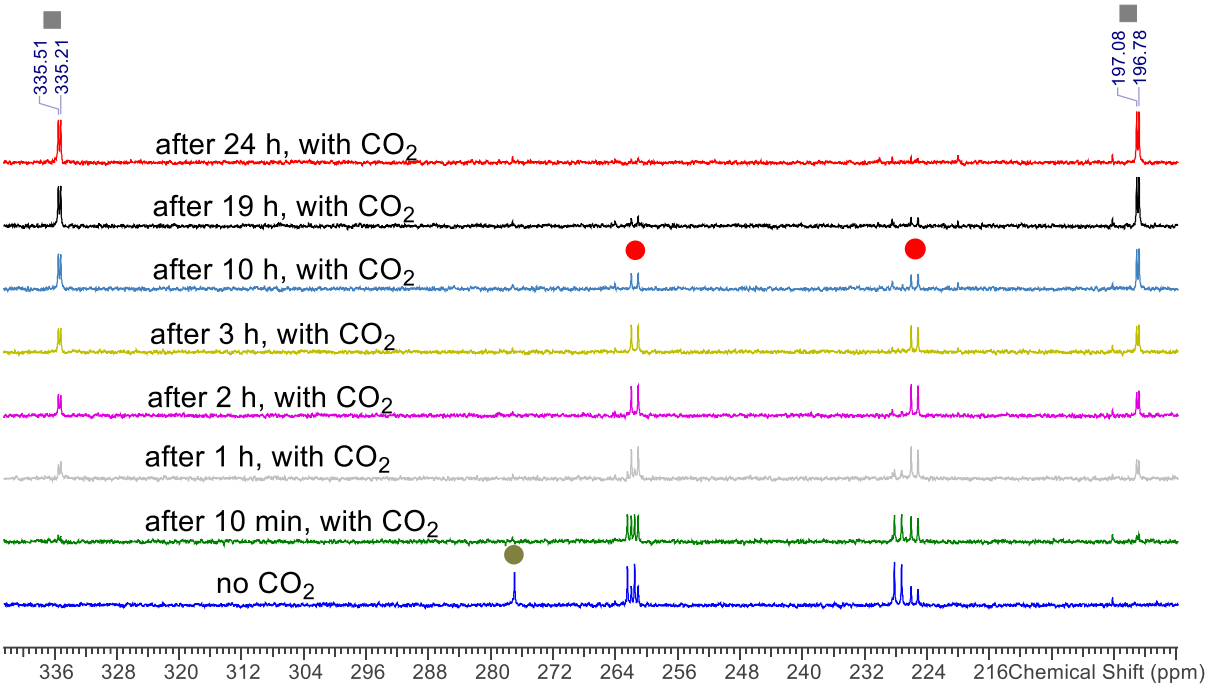

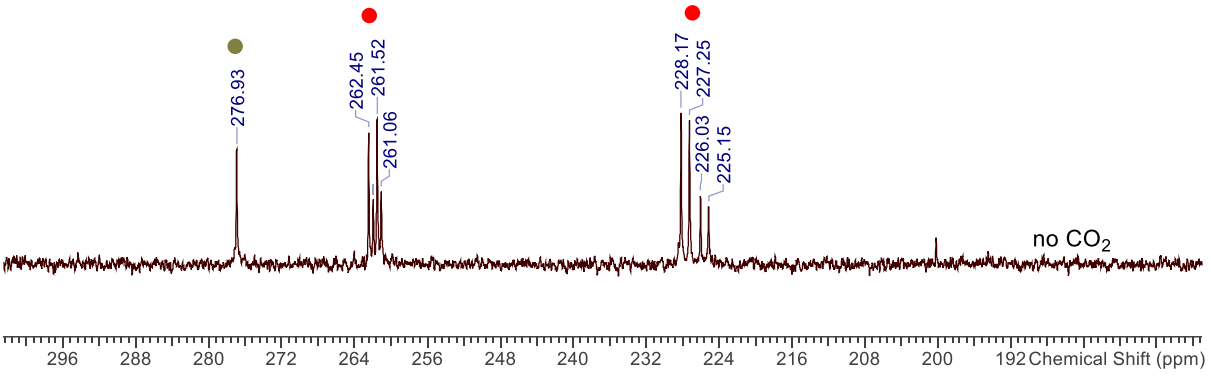

Figure S30. CO_2 activation (data fitted using a pseudo-first-order model)

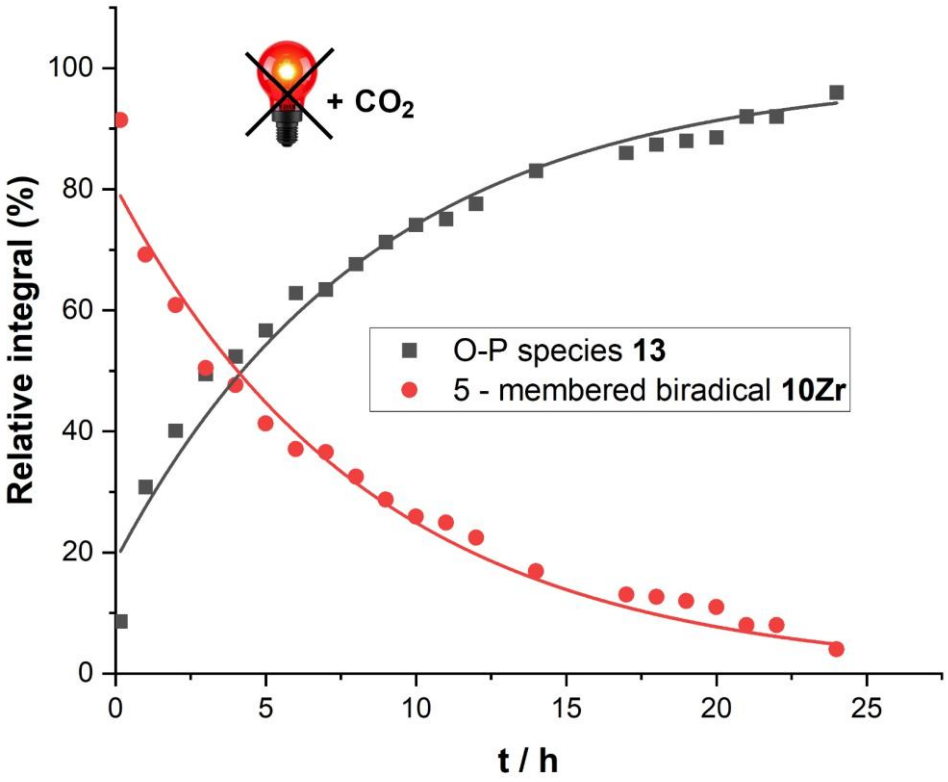

6.2 Titanocene biradical + CO_2 (without irradiation)

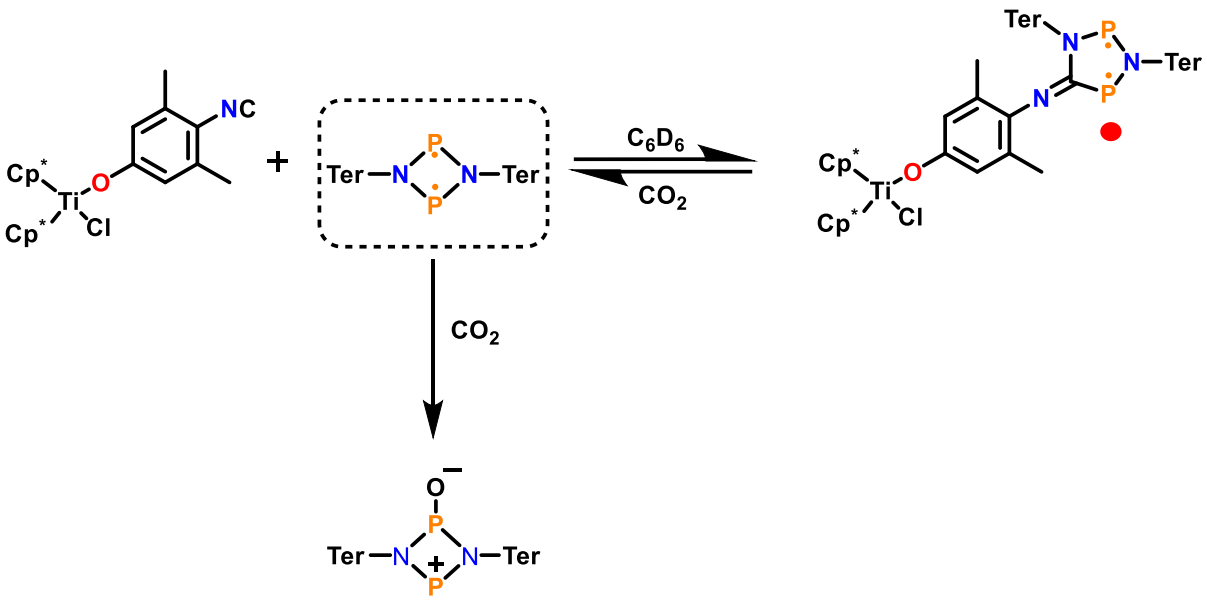

7.18 mg (0.01 mmol) of 4-membered biradical $[TerNP]_2$ + 7.5 mg (0.015 mmol) of Titanocene-mono-linker were mixed as solids in a Young NMR tube. **Note:** Titanocene-monolinker was taken in slight excess in order to get rid of all the four-membered biradicals from the system to delay the equilibrium. Then, 0.5 mL of C_6D_6 was added to the NMR tube in the glove box. ^{31}P NMR was recorded to ensure that no 4-membered biradical is present in the solution.

Later the solution was degassed once, and CO_2 was added under constant flow for 9-10 seconds in the CO_2 Schlenk line. And ^{31}P NMR spectra at room temperature were recorded subsequently, as shown.

Figure S31. $^{31}P\{H\}$ NMR spectra, 161.83 MHz, C_6D_6, 128 scans, 25 °C

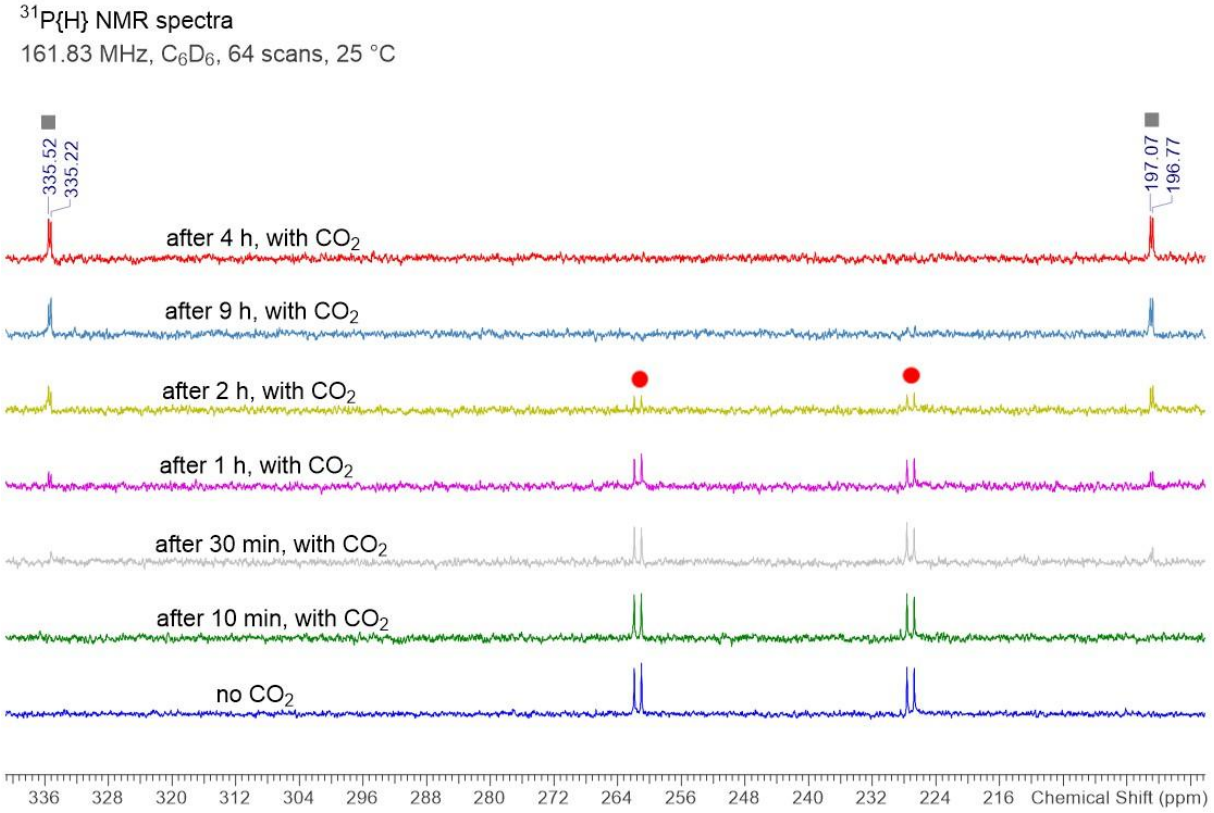

Figure S32. CO_2 activation (data fitted using a pseudo-first-order model)

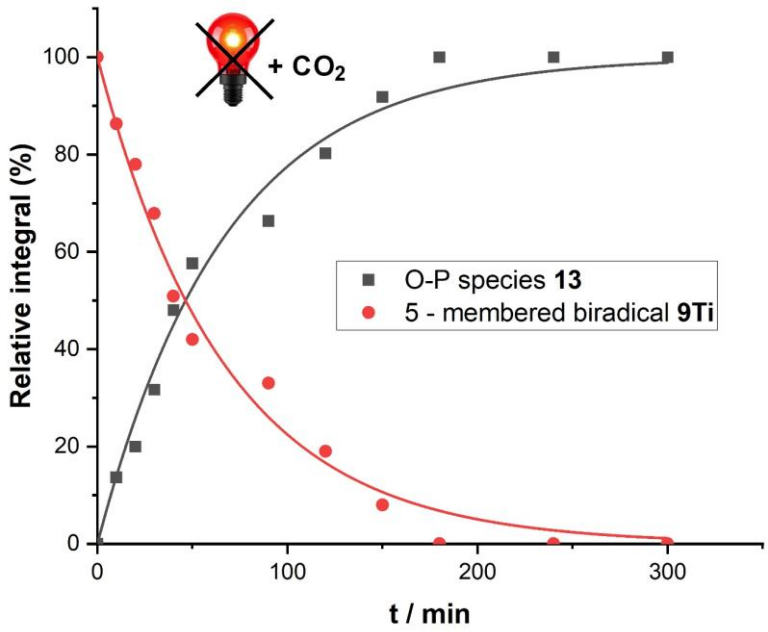

6.3 Titanocene biradical + CO_2 under Irradiation

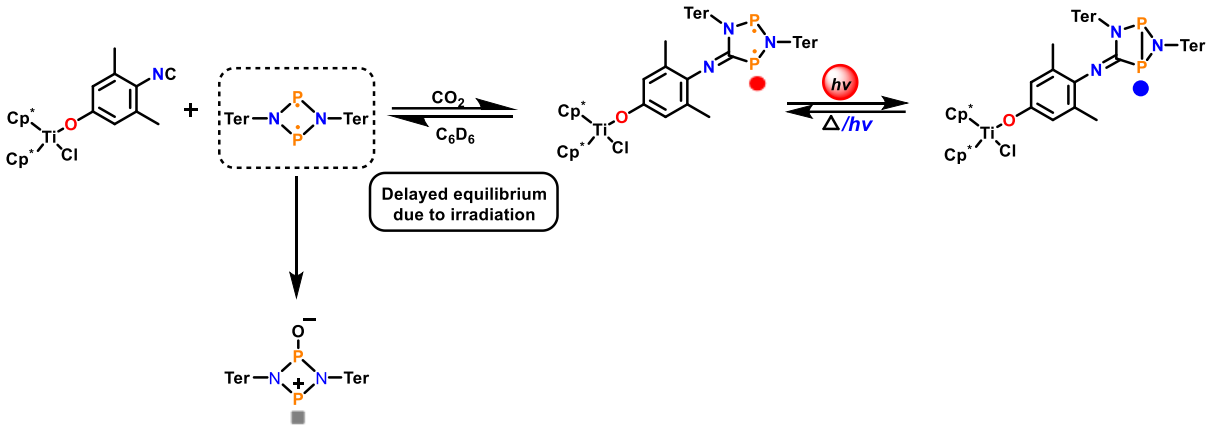

7.18 mg (0.01 mmol) of 4-membered biradical $[TerNP]_2$ + 7.5 mg (0.015 mmol) of Titanocene-mono-linker were mixed as solids in an NMR tube suitable for irradiation. **Note:** Titanocene-mono-linker was taken in slight excess to get rid of all the four-membered biradicals from the system to delay the equilibrium. Then, 0.4 mL of C_6D_6 was added to the NMR tube, and the solution was shaken to enhance the solubility. Then, a coaxial glass insert was fixed inside the NMR tube (which is suitable for irradiation) and sealed properly in the glove box. ^{31}P NMR was recorded to ensure that no 4-membered biradical is present in the solution.

Then, ^{31}P NMR was recorded under irradiation (**irradiation source:** 638 nm red laser diode), and it was observed that it took 20 minutes to get the housane completely.

After its full conversion to housane, 60 mL syringe was filled with CO_2 and with the help of long needle 30 mL of CO_2 was bubbled through the solution for 5-6 seconds.

Then, the solution was subsequently irradiated under the same conditions for 2 hours, during which no CO_2 activation products were observed. After stopping the laser, ^{31}P NMR spectra were recorded over time to monitor the system in the absence of irradiation.

Figure S33. $^{31}P\{H\}$ NMR spectrum, 161.83 MHz, C_6D_6

$^{31}P\{H\}$ NMR spectra

161.83 MHz, C_6D_6, 25 °C

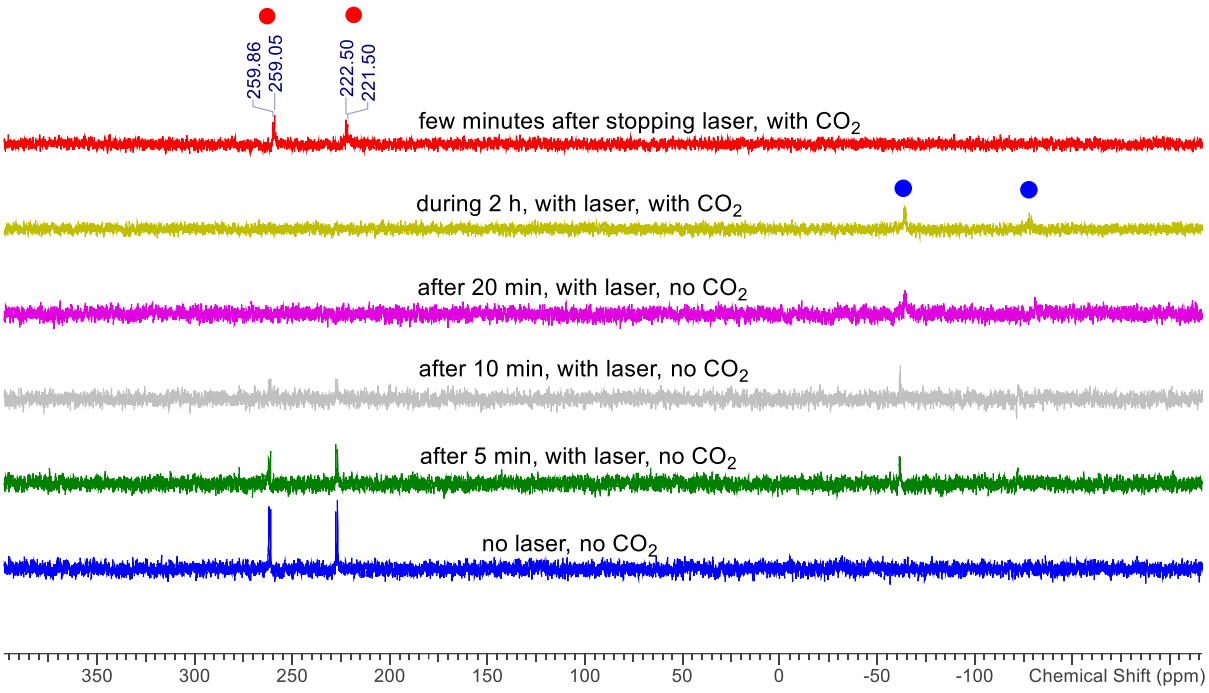

Note – The top two spectra were recorded with 128 scans and the rest with 64 scans

Figure S34. $^{31}P\{H\}$ NMR spectrum, 161.83 MHz, C_6D_6

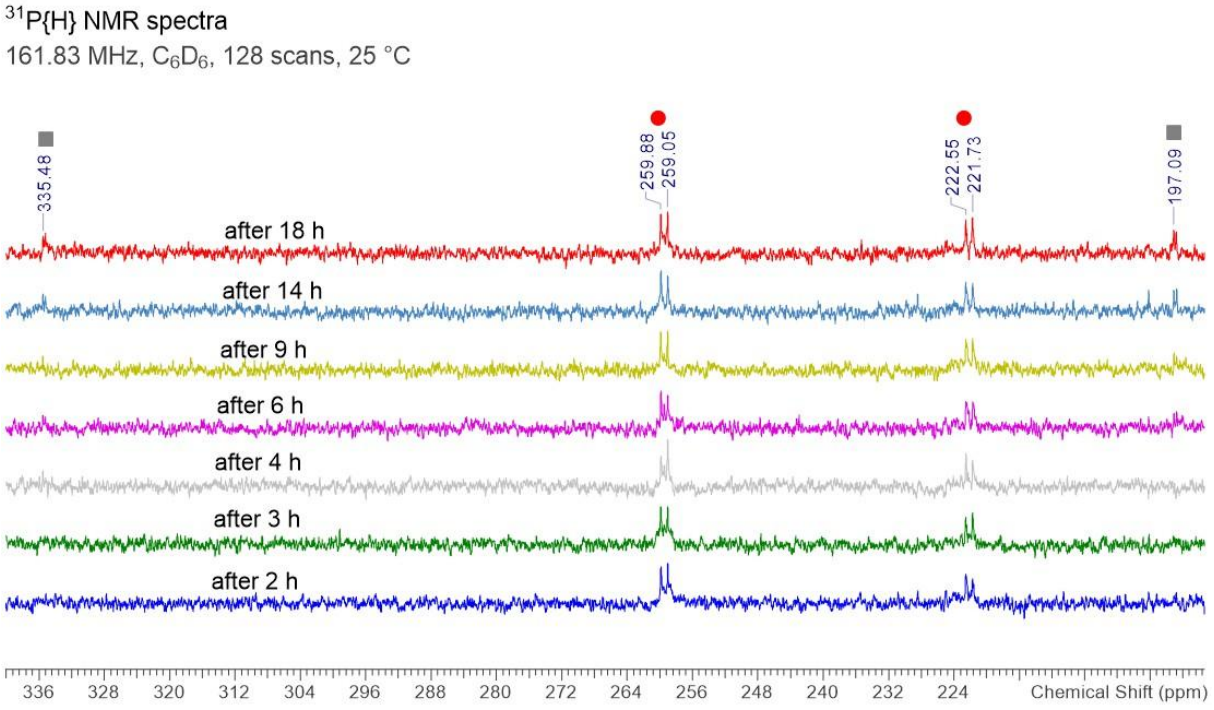

*Above spectra were recorded after the laser was stopped

Figure S35. CO_2 activation

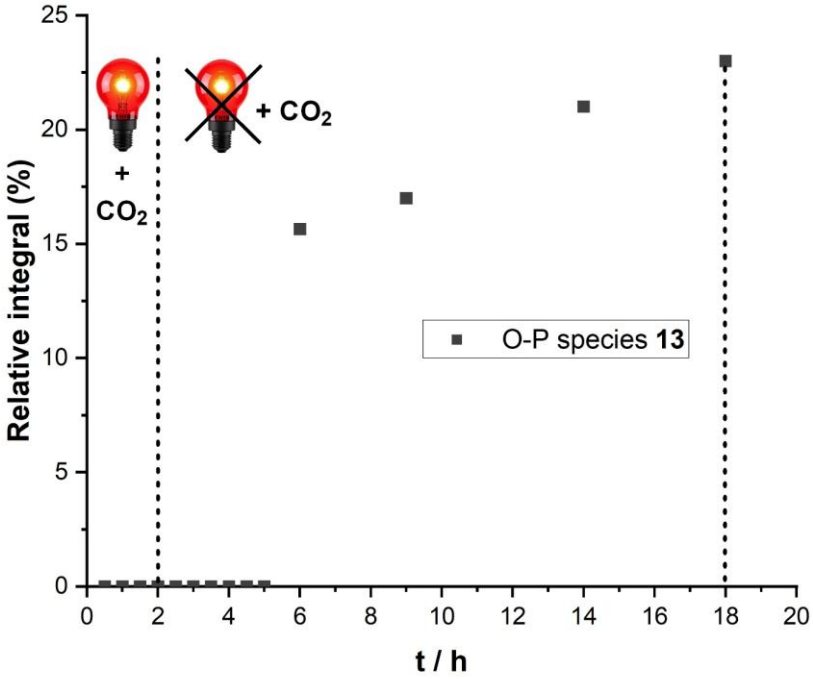

6.4 Spectroscopic Detection of CO by IR and ^{13}C NMR

IR experiment

20 mg of the four-membered biradical $[TerNP]_2$ were dissolved in 0.5 mL of benzene in a J. Young NMR tube. The solution was degassed and subsequently exposed to CO_2. Upon complete color change from orange to red, a sample of the gas phase above the reaction mixture was taken and analyzed by IR gas-phase transmission spectroscopy (a). For comparison, an IR spectrum of pure CO_2 was recorded under identical conditions (b).

Figure S36. IR spectra showing CO detection: top, gas phase above the reaction mixture; bottom, pure CO_2 for reference.

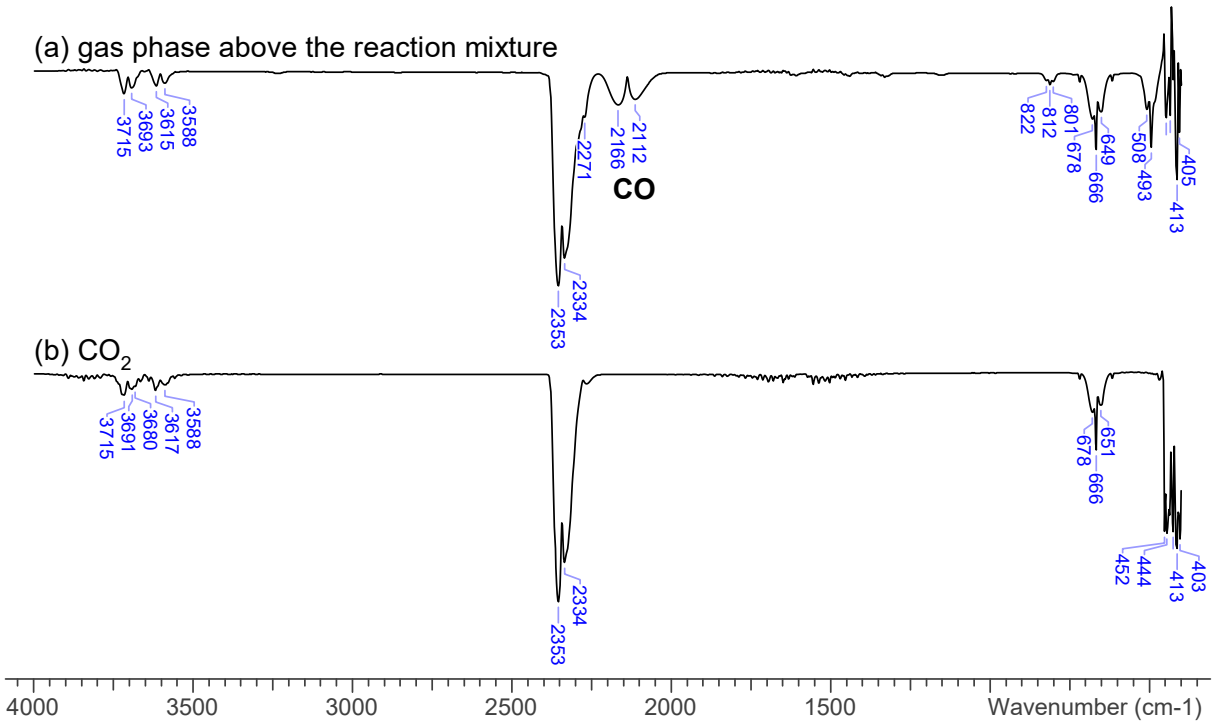

^{13}C NMR experiment

20 mg of the four-membered biradical $[TerNP]_2$ were dissolved in 0.5 mL of benzene in a J. Young NMR tube (blue: before CO_2 addition). The solution was degassed and subsequently exposed to CO_2 (red after CO_2 addition). The resulting NMR spectrum showed a CO resonance at 184.48 ppm and a CO_2 resonance at 125.76 ppm.

Figure S37. ^{13}C NMR spectra.

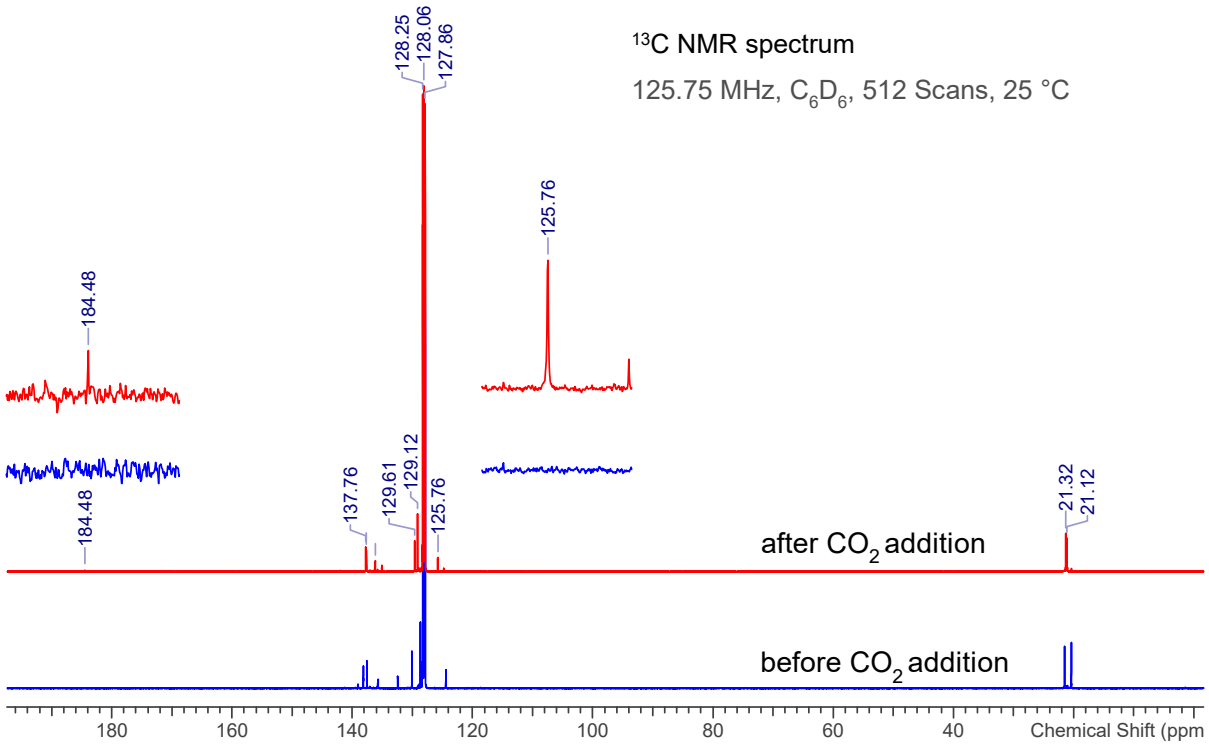

7 Computational details

7.1 General remarks

All quantum chemical calculations were performed using Gaussian16[4] and ORCA (versions 5.0.4 and 6.1.1).[5] The CREST[6,7] program was employed to explore conformational space and identify the lowest-energy conformers. Molecular structures and orbitals were visualized using GaussView, ChemCraft, and IBOView.

To gain further insight into the performance of DFT methods and to investigate the mechanism of the photochemical switching process, we carried out a series of DFT, DLPNO-CCSD(T), and CASSCF calculations. These calculations were first performed on a simplified model system (**2H**, note: we have used a different notation in the computational part, which is shown in the graphics), in which all organic substituents were replaced by hydrogen atoms. Subsequently, tselected computational methods were applied to the full system containing the terphenyl (Ter) substituents.

Structure optimizations employed the DFT functional PBE[8–10] in conjunction with Grimme's dispersion correction D3(BJ)[11,12] and the def2-TZVP basis set[13] (notation: PBE-D3BJ/def2-TZVP). The resolution-of-identity (RI) approximation was applied for the pure functional PBE, using Weigend's accurate Coulomb-fitting basis set (W06).[14] All structures were fully optimized and confirmed as minima or transition states by frequency analysis.

Chemical shifts and coupling constants were derived by the GIAO method[15–19] at the PBE-D3/def2-TZVP level of theory.[8–10,20] The calculated absolute shifts for ^{31}P nuclei ($\sigma_{calc,X}$) were referenced to the experimental absolute shift of 85% H_3PO_4 in the

gas phase ($\sigma_{ref,1}$ = 328.35 ppm),[21] using PH_3 ($\sigma_{ref,2}$ = 594.45 ppm) as a secondary standard:[22]

$$\begin{aligned} \delta_{calc,X} &= (\sigma_{ref,1} - \sigma_{ref,2}) - (\sigma_{calc,X} - \sigma_{calc,PH_3}) \\ &= \sigma_{calc,PH_3} - \sigma_{calc,X} - 266.1 \text{ ppm} \end{aligned}$$

At the PBE-D3BJ/def2-TZVP level of theory, σ_{calc,PH_3} amounts to +562.4283 ppm.[23]

Biradical character of these biradicals must be described by at least two determinants, as the frontier orbitals (HOMO and LUMO) are nearly degenerate. In the singlet ground state, the CASSCF(2,2) wave function is dominated by two configurations, 20 and 02, corresponding to the HOMO and LUMO being doubly occupied, respectively.

$$\Psi_{CAS(2,2)} \approx c_1|2,0> + c_2|0,2>$$

The biradical character β, which quantifies the open-shell contribution, is calculated as

$$\beta = \frac{2{c_2}^2}{{c_1}^2 + {c_2}^2}$$

For biradical 2H, β = 29% for both systems with **CN-Zirconocene** or **CN-Titanocene**.

More accurate electronic energies for optimized structures were computed by single-point DLPNO-CCSD(T)[24–27] calculations employing the def2-TZVP basis set and def2-TZVP/C correlation fitting basis (notation: DLPNO-CCSD(T)/def2-TZVP//PBE-D3BJ/def2-TZVP).[13,20] Thermodynamic quantities at this level of theory were calculated using the DLPNO-CCSD(T) single-point energy and the thermal corrections at the PBE-D3/def2-TZVP level of theory. The T_1 diagnostic was evaluated to ensure reliable results (empirically, CCSD(T) results are considered reliable if T_1 < 0.02).[28] Nonetheless, it should be noted that many of the species discussed here possess at least a small amount of multi-reference character (biradical character), so the use of single-reference methods always entails some loss of accuracy and should be regarded as an approximation!

Note that all computations were carried out for single, isolated molecules in the gas phase (ideal gas approximation). There may be significant differences between the gas phase and the condensed phase.

Note 2 that the substance numbers in this section differ from the manuscript.

7.2 Reaction mechanism

The reaction mechanism of isonitrile insertion was first investigated using a model system, where the **Ter** substituent was replaced by hydrogen. Several transition states were located on the PES using the Nudged Elastic Band (NEB) algorithm[29–33] implemented in ORCA[34] at the PBE-D3/def2-SVP level of theory. In total, two possible reaction pathways were identified: first, the isonitrile approaches from above the two P atoms, and second, when the isonitrile approaches directly to one P atom. All minima and TS structures of these reaction mechanisms were optimized at the PBE-D3/def2-TZVP level of theory and confirmed as minima or transition states by frequency analyses. Single-point calculations at the DLPNO-CCSD(T)/def2-TZVP//PBE-D3/def2-TZVP level of theory were carried out as described above for comparison.

[Discussion for Biradicals with CNR (R = methyl, phenyl, trichloromethyl, 2,4,6-Trichlorobenzene)]

The transformation of a four-membered biradical [P(μ-NTer)]$_2$ precursor with bis(2,4,6-trimethylphenyl)phenyl (Ter) into five-membered products upon addition of iso-cyanides has been investigated computationally. A range of substituents R in CNR was considered, where R = methyl, phenyl, trichloromethyl, or trichlorobenzene.

Two distinct mechanistic pathways for the approach of the isocyanide fragment to the biradical precursor were examined:

1. A symmetric, concerted approach, in which the isocyanide group (CN) is positioned above and between the two phosphorus atoms, interacting simultaneously with both centres.
2. A localized approach, in which the CN group is oriented perpendicularly toward a single phosphorus atom, interacting exclusively with that site, while the R group extends outward from the ring plane. The effect of the isocyanide substituent (R in CNR) on the reaction pathways and product stability was analyzed.

Both reaction mechanisms were designed to converge to the same five-membered product species, allowing for a direct comparison of the kinetic profiles and substituent effects. To assess the effect of basis set size on the computed energetics, single-point energy calculations at the def2-TZVP level were performed on geometries optimized at the def2-SVP level. In general, def2-TZVP calculations led to a systematic stabilization of all species, with absolute energies significantly lower than those obtained at the def2-SVP level. Importantly, the qualitative features of the reaction profiles — such as the relative ordering of intermediates and the preference for Path — remained consistent across both levels of theory. However, the def2-TZVP data showed reduced energy barriers in several key steps, most notably for TS2 and TS4, suggesting that the larger basis set provides a more reliable estimation of activation energies while preserving the overall mechanistic trends.

In pathway 1, the isocyanide approaches both phosphorus atoms at the same time, forming two P–C bonds simultaneously. This mechanism leads to a very stable product, but the second transition state (TS2) is very high, making the reaction quite challenging under standard conditions and probably requiring significant heating or alternative pathways in reality.

In contrast, pathway 2 follows a stepwise mechanism: the isocyanide first coordinates with one phosphorus atom, forming an intermediate, and then proceeds to the final ring closure via a second, much lower, transition state. This pathway shows a

significantly lower energy barrier overall and is therefore more likely to occur experimentally.

The calculated energy profiles for both reaction pathways were analyzed across a range of isocyanide substituents (R = Me, Ph, CCl_3, $PhCl_3$) using PBE/def2-SVP and PBE/def2-TZVP levels of theory (Table S26).

Overall, the data indicate a substantial influence of the R substituent on both the stability of intermediates and the height of transition state barriers. Electron-withdrawing and sterically bulky groups, such as CN-CCl_3 and CN-$PhCl_3$, consistently stabilize key intermediates (INT1, INT2) and lower the energies of transition states, particularly TS4 in Path 2. In contrast, the smaller CN-Me and CN-Ph substituents lead to higher energy intermediates and transition states, suggesting a less favourable transformation pathway.

A comparison between the two mechanistic routes reveals that Path 2 is generally more favourable than Path 1 in terms of activation energy. For most substituents, the highest transition state in Path 2 (TS4) lies significantly lower in energy than the corresponding TS2 in Path 1. Notably, for CN-CCl_3, TS4 reaches as low as −10.3 kJ/mol, while TS2 in Path 1 is substantially higher. Additionally, Path 2 shows a more stabilized intermediate (INT2) and an overall smoother energy profile.

Figure S38. Gibbs free energy of the reaction of **CN-Zirconocene** to **3H** (first pathway) at the PBE-D3/def2-TZVP level of theory (Blue) and single-point DLPNO-CCSD(T)/def2-TZVP//PBE-D3/def2-TZVP level of theory (Orange) (c° = 1 mol/L).

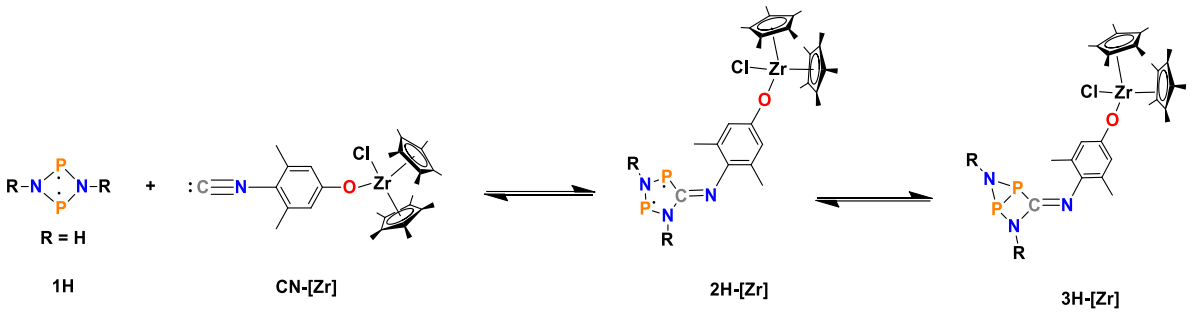

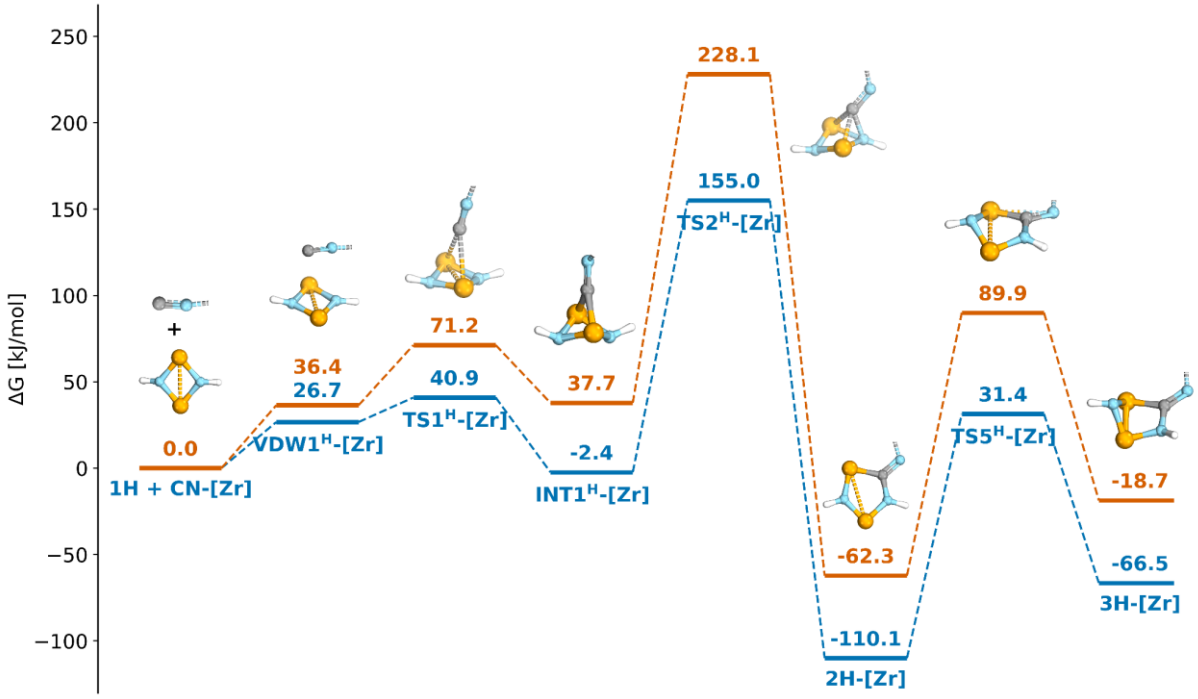

Figure S39. Gibbs free energy of the reaction of **CN-Zirconocene** to **3H** (second pathway) at the PBE-D3/def2-TZVP level of theory (Blue) and single-point DLPNO-CCSD(T)/def2-TZVP//PBE-D3/def2-TZVP level of theory (Orange) (c° = 1 mol/L).

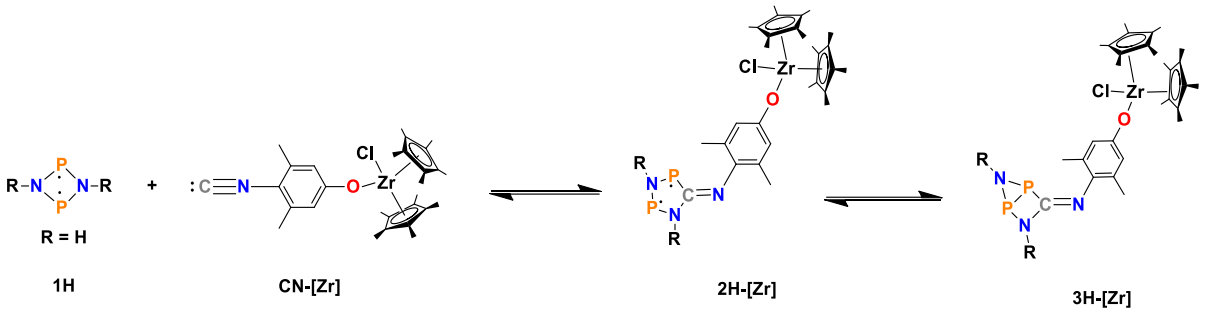

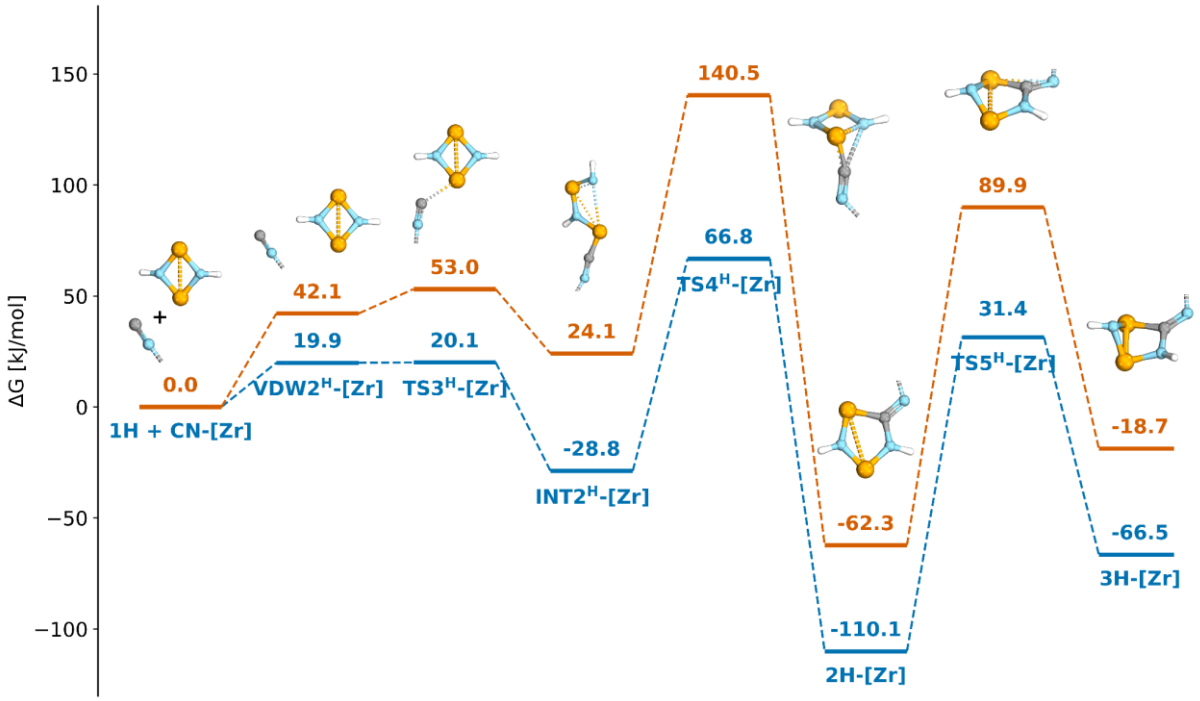

Figure 40. Gibbs free energy of the reaction of **CN-Titanocene** to **3H** (first pathway) at the PBE-D3/def2-TZVP level of theory (Blue) and single-point DLPNO-CCSD(T)/def2-TZVP//PBE-D3/def2-TZVP level of theory (Orange) (c° = 1 mol/L).

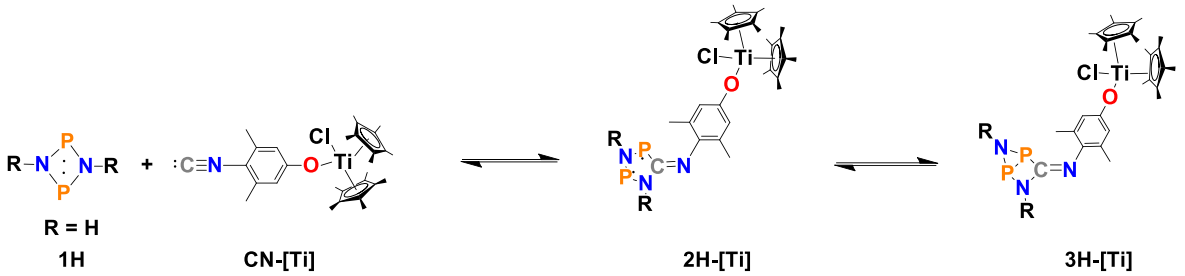

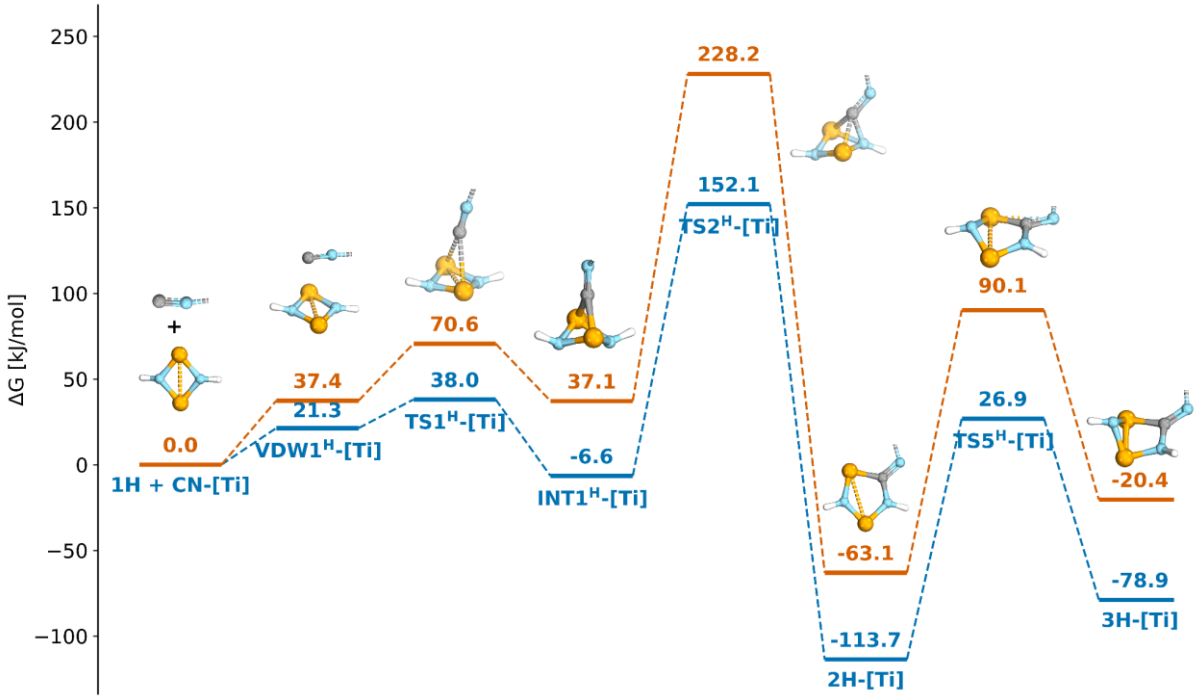

Figure S41. Gibbs free energy of the reaction of **CN-Titanocene** to **3H** (second pathway) at the PBE-D3/def2-TZVP level of theory (Blue) and single-point DLPNO-CCSD(T)/def2-TZVP//PBE-D3/def2-TZVP level of theory (Orange) (c° = 1 mol/L).

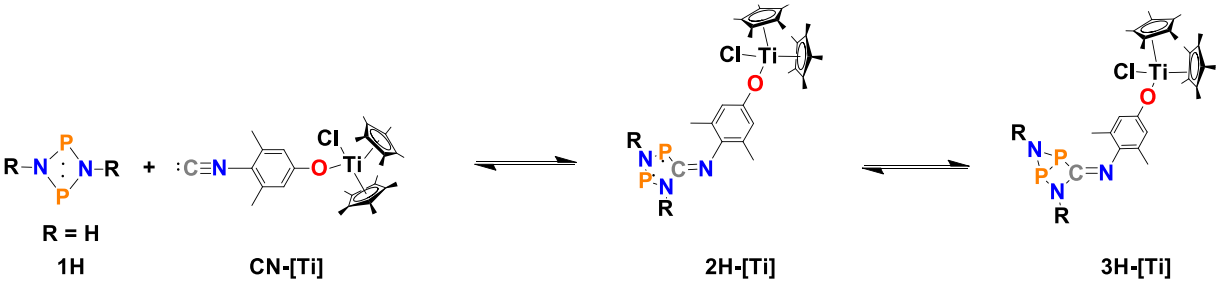

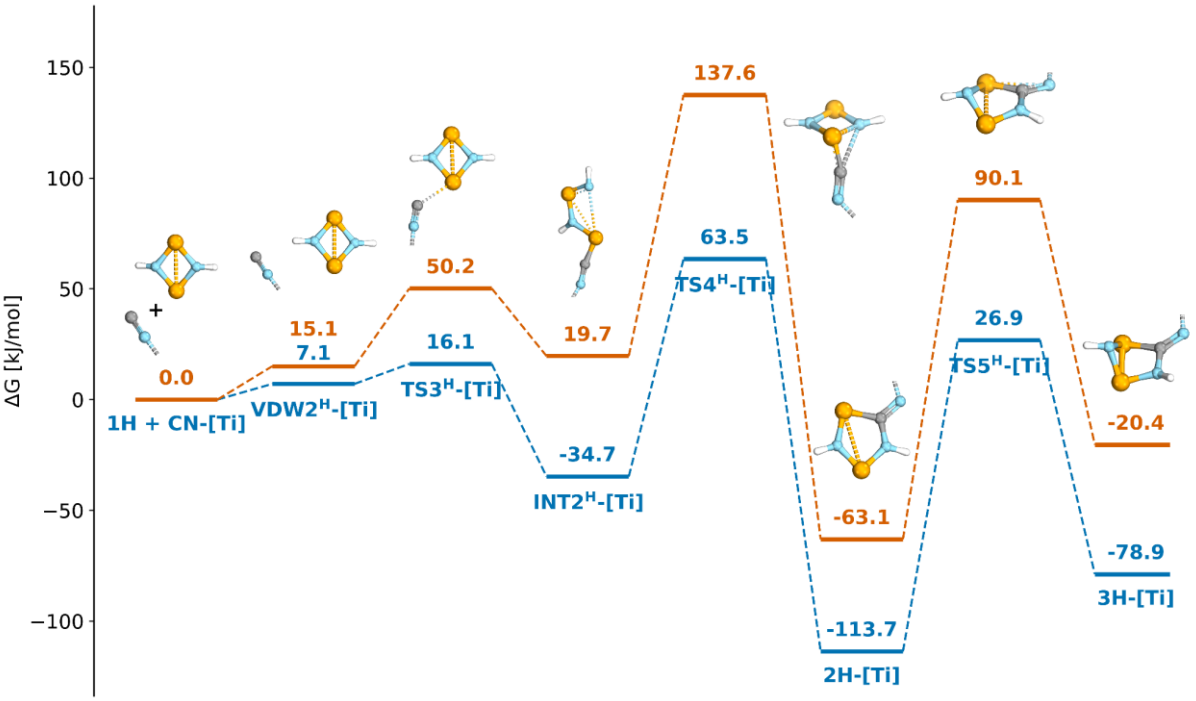

Figure S42. Gibbs free energy of the reaction of **CN-Methyl** to **2Ter** (first pathway) at the PBE-D3/def2-TZVP//PBE-D3/def2-SVP level of theory (Blue) and single-point DLPNO-CCSD(T)/def2-TZVP//PBE-D3/def2-SVP level of theory (Orange) (c° = 1 mol/L).

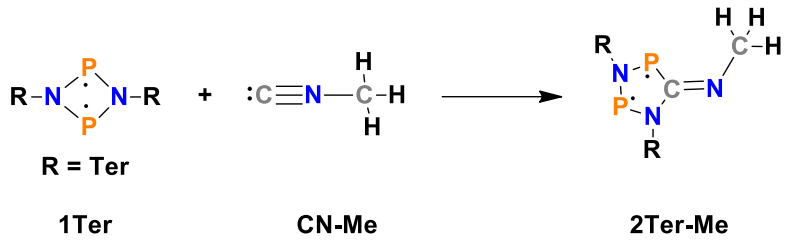

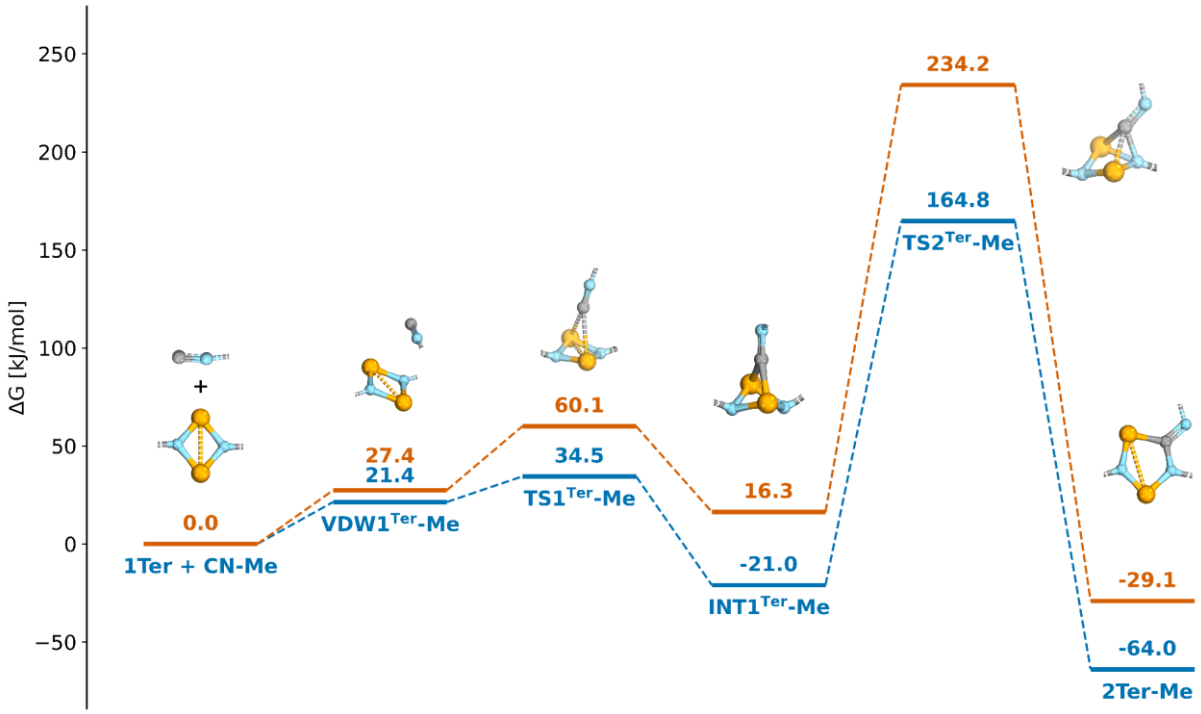

Figure S43. Gibbs free energy of the reaction of **CN-Methyl** to **2Ter** (second pathway) at the PBE-D3/def2-TZVP//PBE-D3/def2-SVP level of theory (Blue) and single-point DLPNO-CCSD(T)/def2-TZVP//PBE-D3/def2-SVP level of theory (Orange) (c° = 1 mol/L).

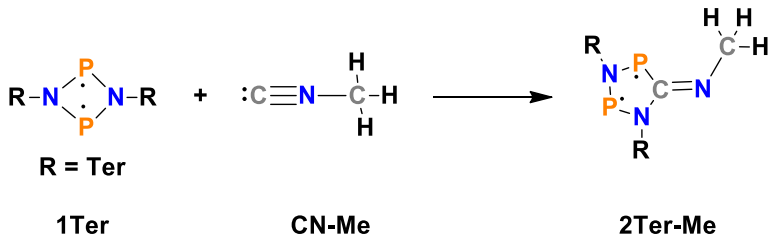

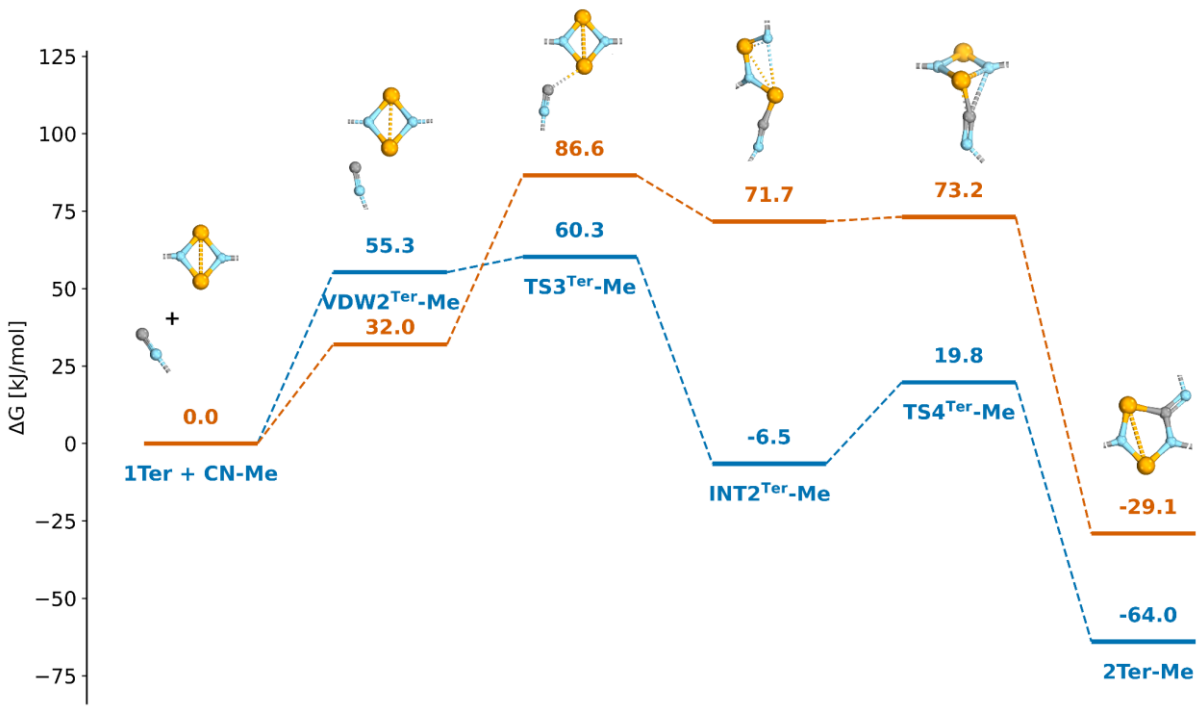

Figure 44. Gibbs free energy of the reaction of **CN-Trichloromethyl** to **2Ter** (first pathway) at the PBE-D3/def2-TZVP//PBE-D3/def2-SVP level of theory (Blue) and single-point DLPNO-CCSD(T)/def2-TZVP//PBE-D3/def2-SVP level of theory (Orange) (c° = 1 mol/L).

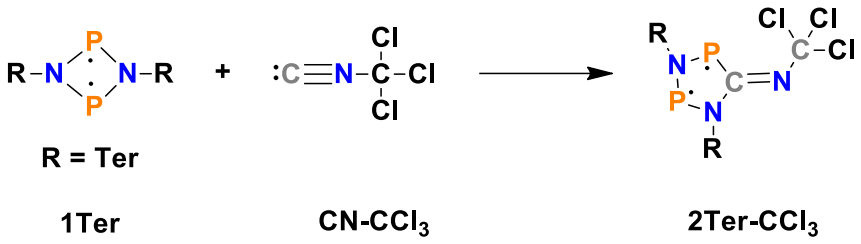

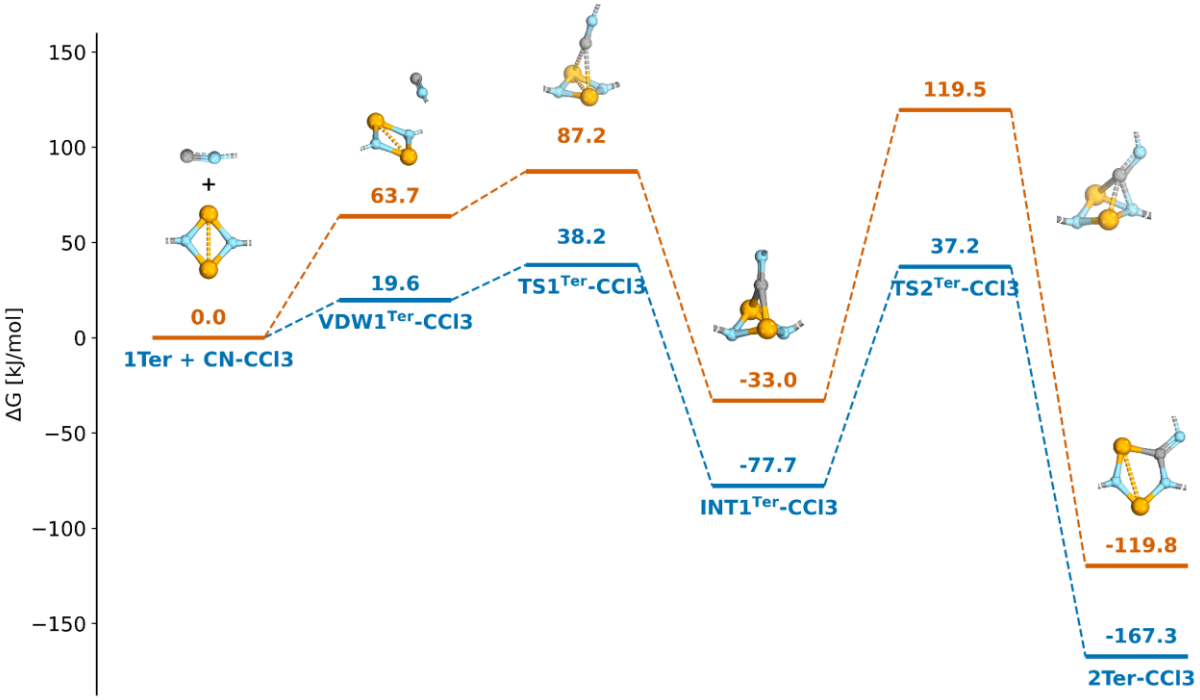

Figure S45. Gibbs free energy of the reaction of **CN-Trichloromethyl** to **2Ter** (second pathway) at the PBE-D3/def2-TZVP//PBE-D3/def2-SVP level of theory (Blue) and single-point DLPNO-CCSD(T)/def2-TZVP//PBE-D3/def2-SVP level of theory (Orange) (c° = 1 mol/L).

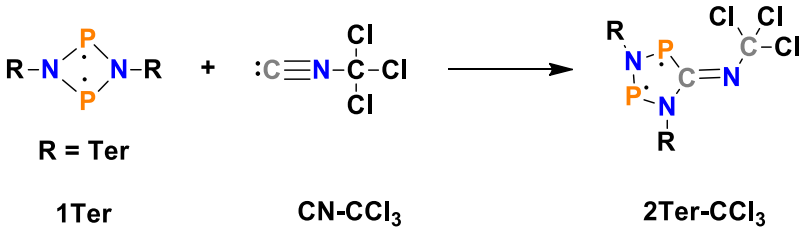

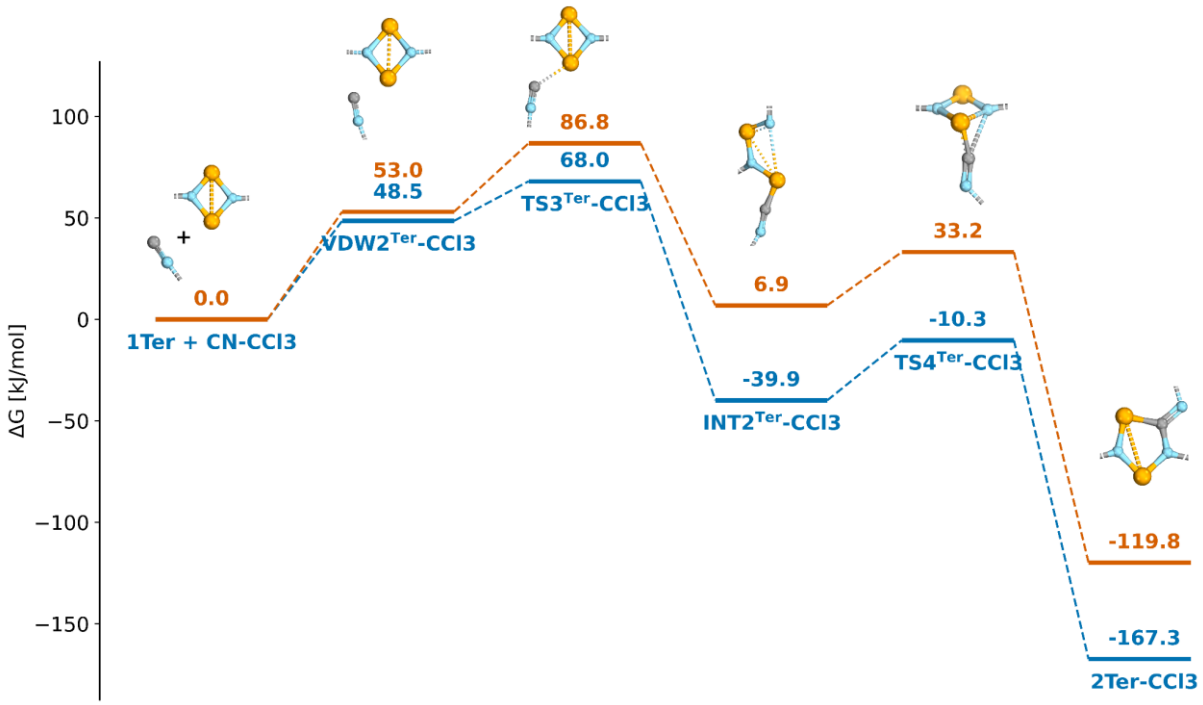

Figure S46. Gibbs free energy of the reaction of **CN-Benzene** to **2Ter** (first pathway) at the PBE-D3/def2-TZVP//PBE-D3/def2-SVP level of theory (Blue) and single-point DLPNO-CCSD(T)/def2-TZVP//PBE-D3/def2-SVP level of theory (Orange) (c° = 1 mol/L).

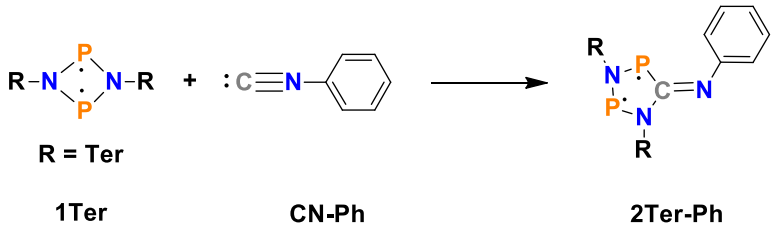

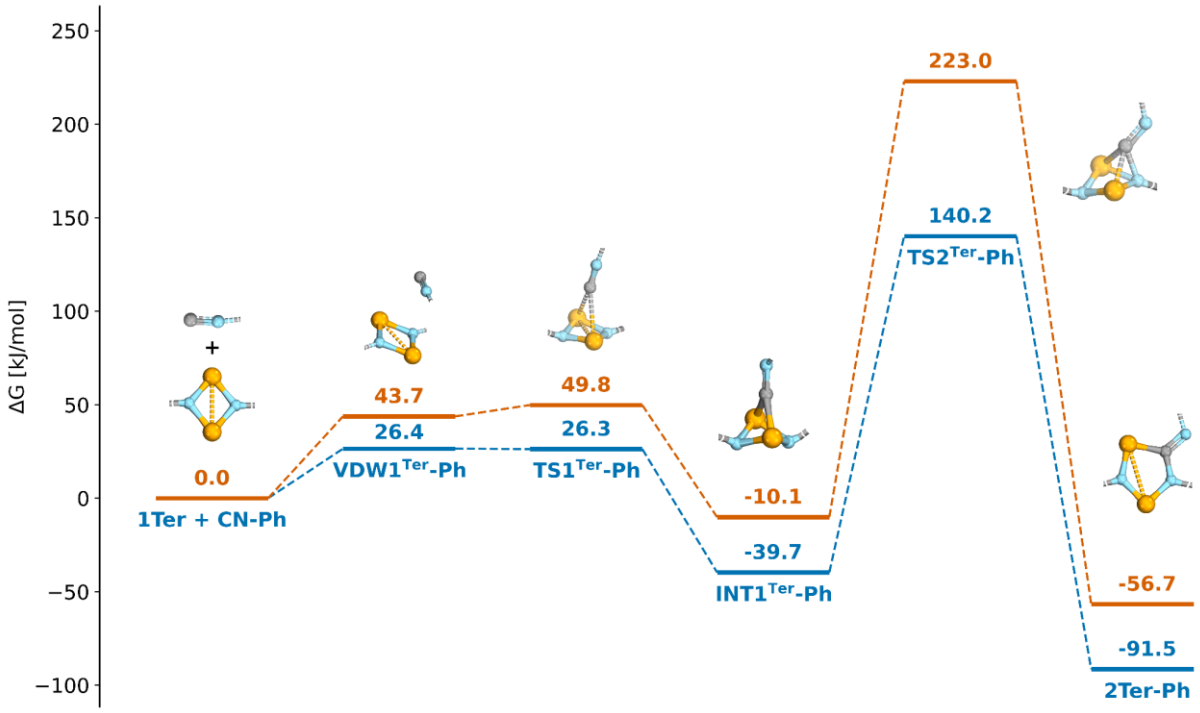

Figure S47. Gibbs free energy of the reaction of **CN-Benzene** to **2Ter** (second pathway) at the PBE-D3/def2-TZVP//PBE-D3/def2-SVP level of theory (Blue) and single-point DLPNO-CCSD(T)/def2-TZVP//PBE-D3/def2-SVP level of theory (Orange) (c° = 1 mol/L).

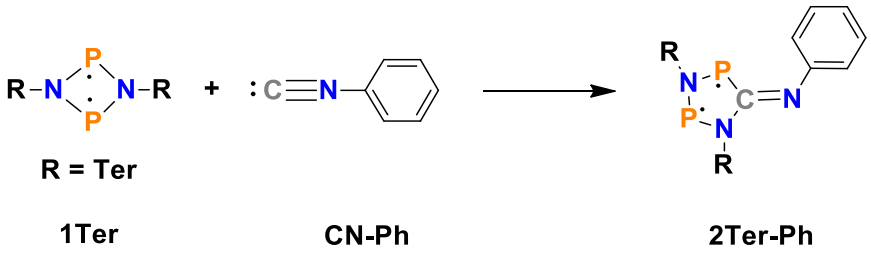

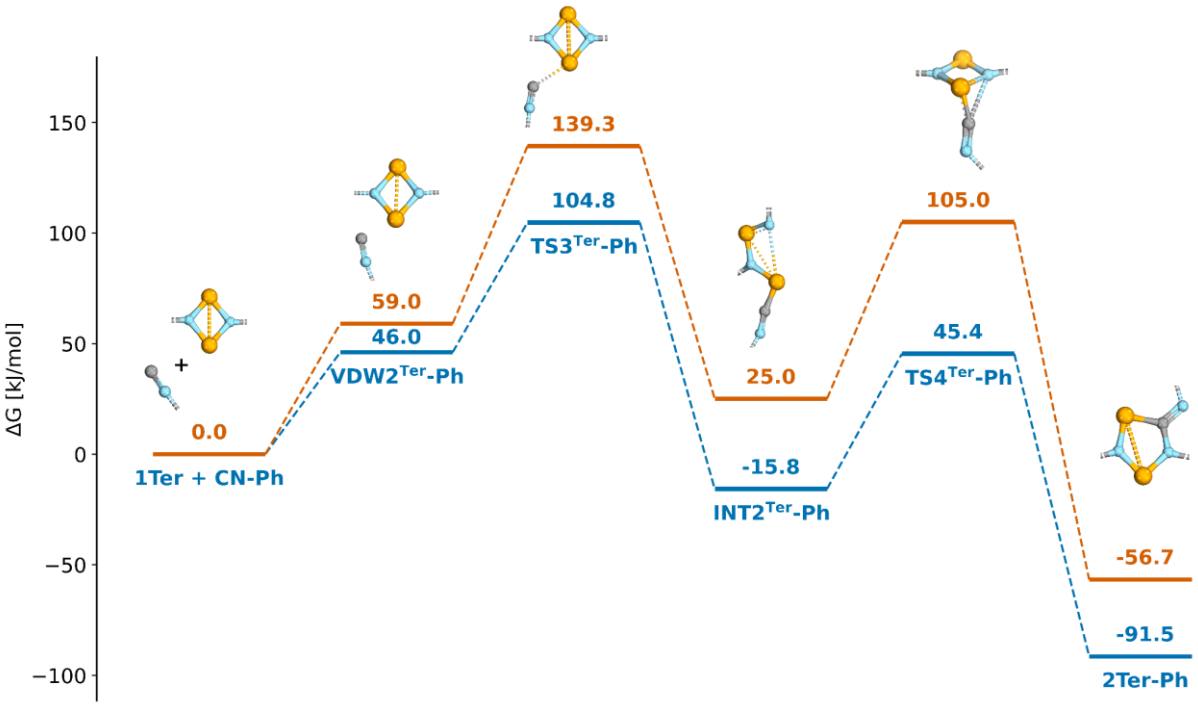

Figure S48. Gibbs free energy of the reaction of **CN-Trichlorobenzene** to **2Ter** (first pathway) at the PBE-D3/def2-TZVP//PBE-D3/def2-SVP level of theory (Blue) and single-point DLPNO-CCSD(T)/def2-TZVP//PBE-D3/def2-SVP level of theory (Orange) (c° = 1 mol/L).

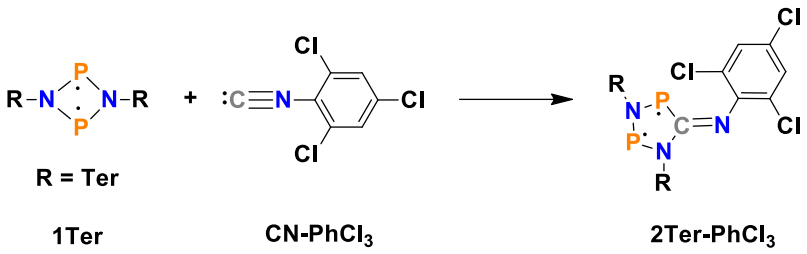

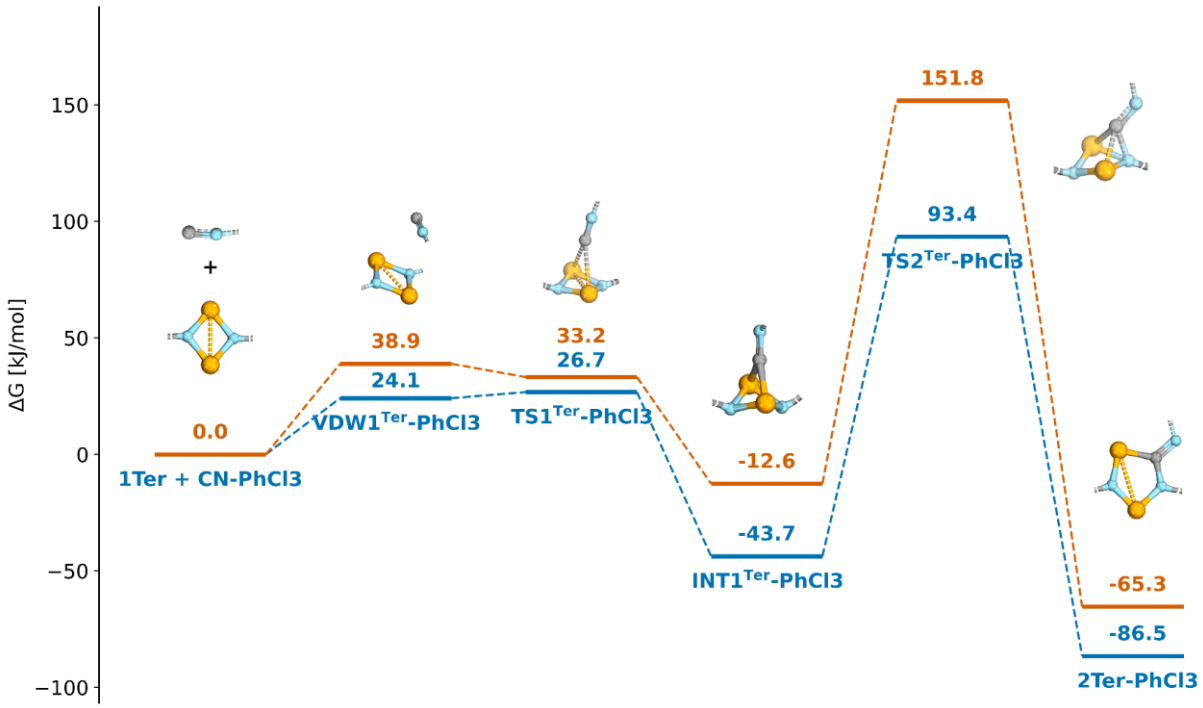

Figure S49. Gibbs free energy of the reaction of **CN-Trichlorobenzene** to **2Ter** (second pathway) at the PBE-D3/def2-TZVP//PBE-D3/def2-SVP level of theory (Blue) and single-point DLPNO-CCSD(T)/def2-TZVP//PBE-D3/def2-SVP level of theory (Orange) (c° = 1 mol/L).

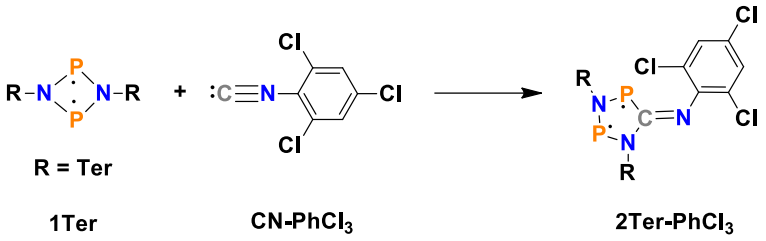

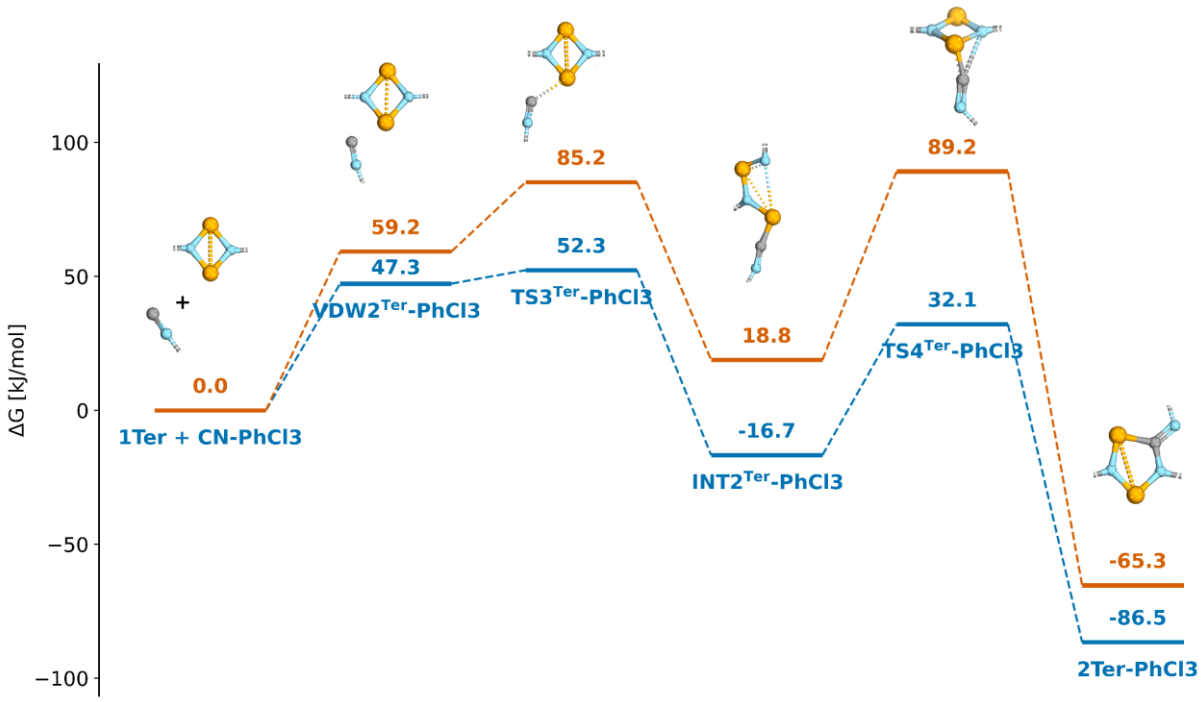

7.3 Calculated NMR data

Table S4. Calculated NMR shifts and coupling constants at PBE-D3/def2-TZVP of **CN-Zirconocene** for the model system with **H** sides.

Compound	δ_{P1}[ppm]	δ_{P2}[ppm]	J(P-P)[Hz]
1H	336.6	336.6	394
VWD1^{H}-[Zr]	335.2	320.5	393
VWD2^{H}-[Zr]	227.2	314.7	300
INT1^{H}-[Zr]	435.6	425.9	8
INT2^{H}-[Zr]	7.4	392	-29
2H-[Zr]	316.4	283.3	210
3H-[Zr]	-62.3	-146.3	-78

Table S5. Calculated NMR shifts and coupling constants at PBE-D3/def2-TZVP of **CN-Zirconocene** for the case with **Ter** sides.

Compound	δ_{P1}	δ_{P2}	J(P-P)
1Ter	305.2	305.5	336
VWD1^{Ter}-[Zr]	332.1	320.3	357
VWD2^{Ter}-[Zr]	333.6	337.1	395
INT1^{Ter}-[Zr]	364.4	353	-13
INT2^{Ter}-[Zr]	36.5	329.6	-8
2Ter-[Zr]	335.1	332.6	302
3Ter-[Zr]	-124.2	-4.3	-33

Table S6. Calculated NMR shifts and coupling constants at PBE-D3/def2-TZVP of **CN-Titanocene** for the model system with **H** sides.

Compound	δ_{P1}	δ_{P2}	J(P-P)
1H	336.6	336.6	394
VWD1^{H}-[Ti]	329.3	327.1	396
VWD2^{H}-[Ti]	331.7	331.9	373
INT1^{H}-[Ti]	435.5	428.9	8
INT2^{H}-[Ti]	391.4	5.1	-29
2H-[Ti]	316.3	282.5	209
3H-[Ti]	-61.5	-146.1	-78

Table S7. Calculated NMR shifts and coupling constants at PBE-D3/def2-TZVP of **CN-Titanocene** for the case with **Ter** sides.

Compound	δ_{P1}	δ_{P2}	J(P-P)
1Ter	305.2	305.5	336
VWD1^{Ter}-[Ti]	323.4	319.5	348
VWD2^{Ter}-[Ti]	320	315.3	371
INT1^{Ter}-[Ti]	345	333.6	-8
INT2^{Ter}-[Ti]	17.9	317.1	-9
2Ter-[Ti]	308.3	312.1	234
3Ter-[Ti]	-141	-17.7	-38

1.4 CASSCF computations on biradicals

In the following, the orbitals of the active spaces in CASSCF(2,2) computations of the entire reaction for **2H** + CN-**Titanocene** are illustrated (Figure S13 and Figure S14). For the **Zirconocene**-containing system, the CASSCF orbitals exhibit essentially the same characteristics; therefore, only the representative example for CN-**Titanocene** is presented.

Table 8. Most important configurations that contribute to the CASSCF(2,2)/def2-TZVP wave function of the reaction (|ci2|>0.01).

Compound	Configuration	C_I^2	Compound	Configuration	C_I^2
VWD1^{H}-[Ti]	20	0.87444	**VWD2^{H}-[Ti]**	20	0.87852
	02	0.12556		02	0.12148
TS1^{H}-[Ti]	20	0.90386	**TS3^{H}-[Ti]**	20	0.88015
	02	0.09614		02	0.11985
INT1^{H}-[Ti]	20	0.99575	**INT2^{H}-[Ti]**	20	0.99098
	02	0.00425		02	0.00902
TS2^{H}-[Ti]	20	0.97944	**TS4^{H}-[Ti]**	20	0.99126
	02	0.02056		02	0.00874
2H-[Ti]	20	0.85660	**2H-[Ti]**	20	0.85660
	02	0.14340		02	0.14340
TS5-[Ti]	20	0.98599	**TS5-[Ti]**	20	0.98599
	02	0.01401		02	0.01401
3H-[Ti]	20	0.85660	**3H-[Ti]**	20	0.85660
	02	0.14340		02	0.14340

Figure S50. CASSCF(2,2)/def2-TZVP//PBE-D3/def2-TZVP orbitals (isovalue = 0.03) of the reaction (first pathway).

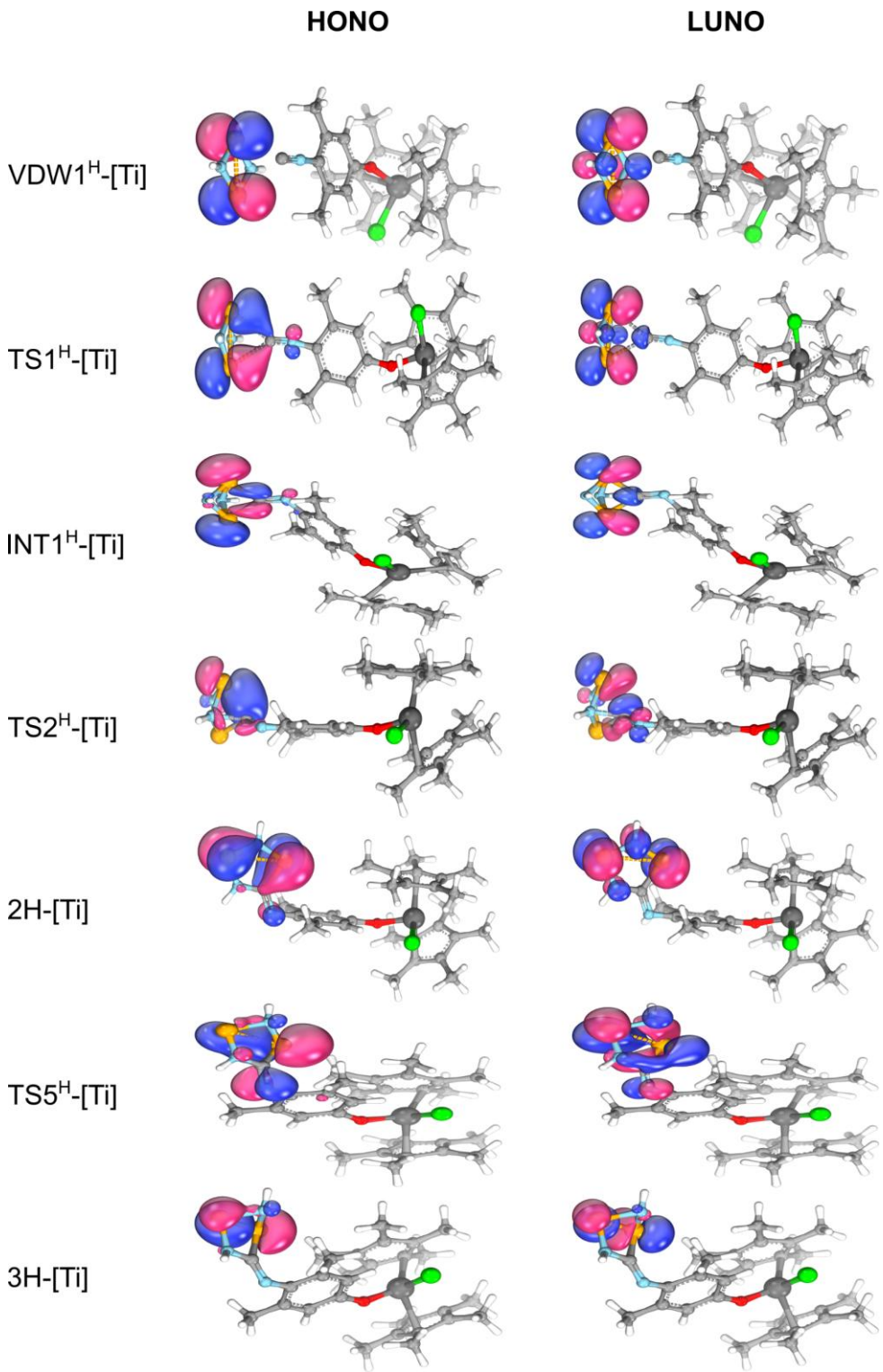

Figure S51. CASSCF(2,2)/def2-TZVP//PBE-D3/def2-TZVP orbitals (isovalue = 0.03) of the reaction (second pathway).

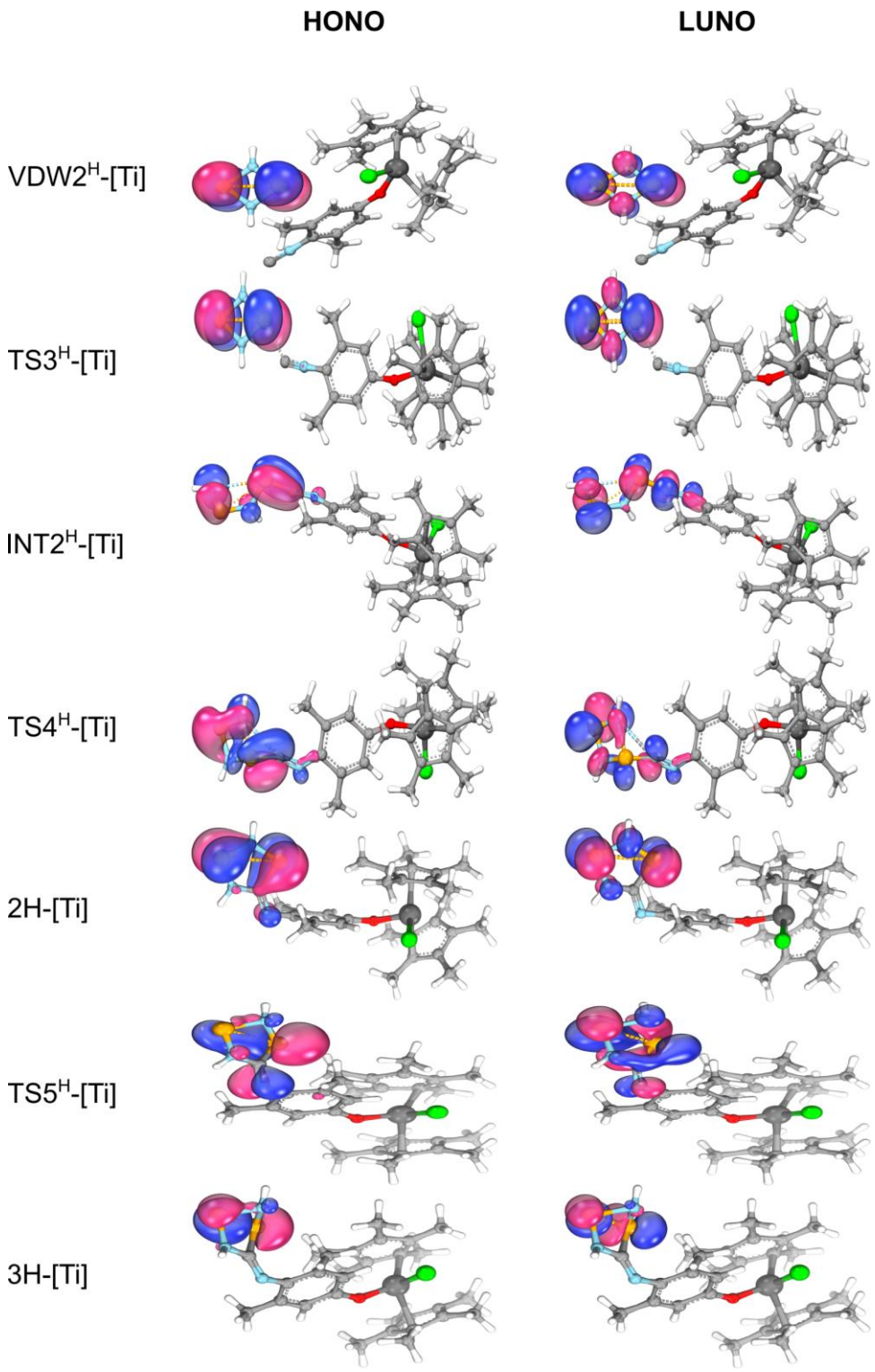

The active-space orbitals (HONO and LUNO) obtained from the CASSCF(2,2) calculations for the Ti/Zr-biradical and Ti/Zr-housane species bearing the Terphenyl substituent are illustrated in Figures S52-55 and compared with the corresponding Kohn–Sham orbitals (HOMO and LUMO).

Figure S52. CASSCF(2,2)/def2-TZVP//PBE-D3/def2-TZVP active-space orbitals (HONO, LUNO) and corresponding Kohn–Sham orbitals (HOMO, LUMO) of the **Zr-biradical** (isovalue = 0.03).

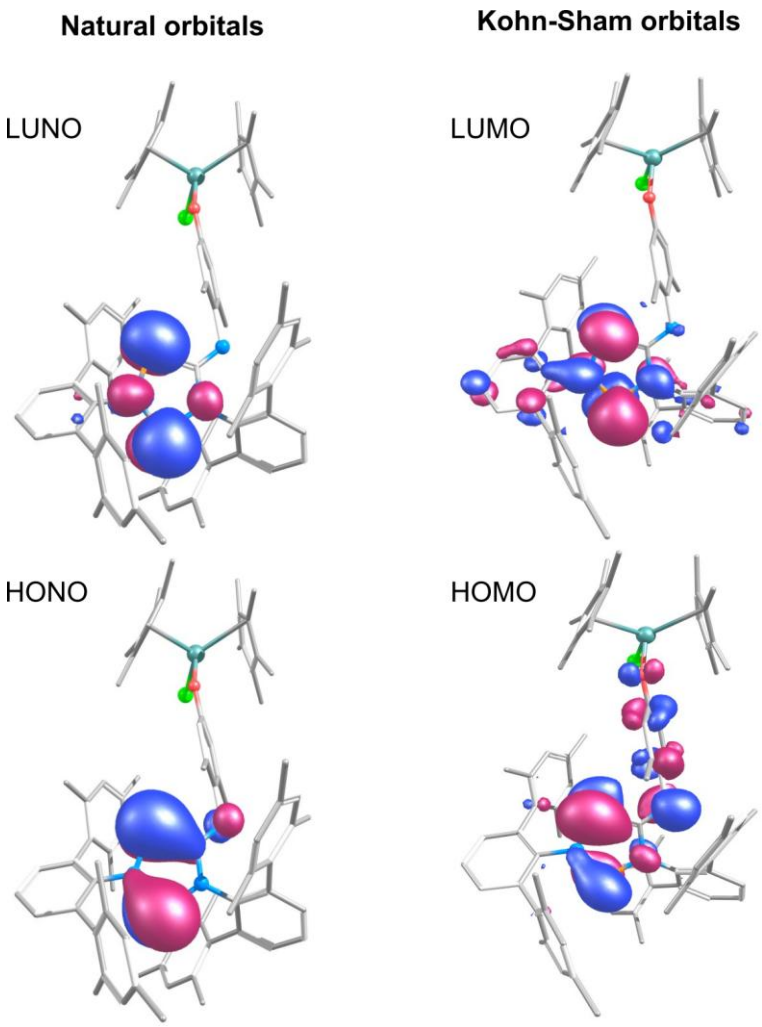

Figure S53. CASSCF(2,2)/def2-TZVP//PBE-D3/def2-TZVP active-space orbitals (HONO, LUNO) and corresponding Kohn–Sham orbitals (HOMO, LUMO) of the **Zr-housane** (isovalue = 0.03).

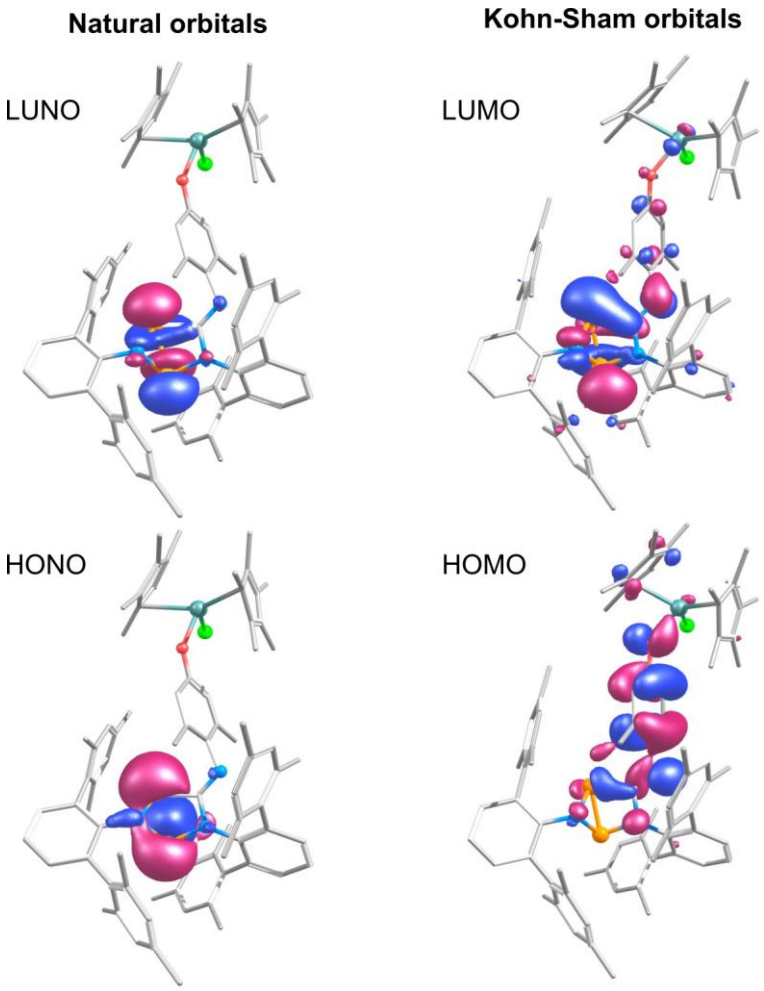

Figure S54. CASSCF(2,2)/def2-TZVP//PBE-D3/def2-TZVP active-space orbitals (HONO, LUNO) and corresponding Kohn–Sham orbitals (HOMO, LUMO) of the **Ti-biradical** (isovalue = 0.03).

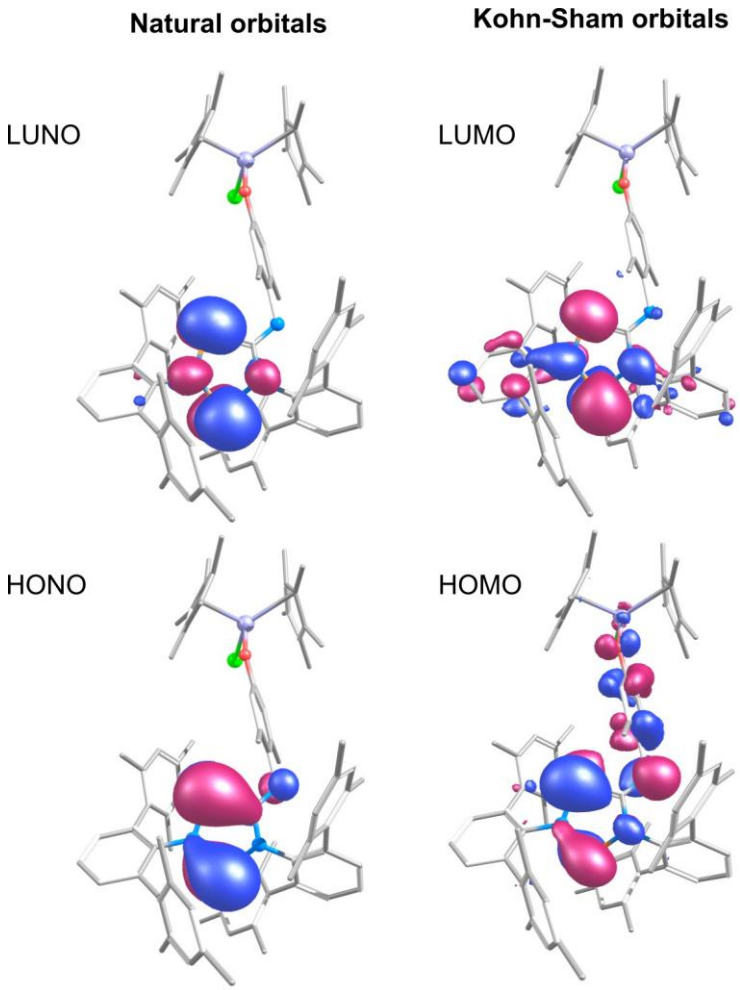

Figure S55. CASSCF(2,2)/def2-TZVP//PBE-D3/def2-TZVP active-space orbitals (HONO, LUNO) and corresponding Kohn–Sham orbitals (HOMO, LUMO) of the **Ti-housane** (isovalue = 0.03).

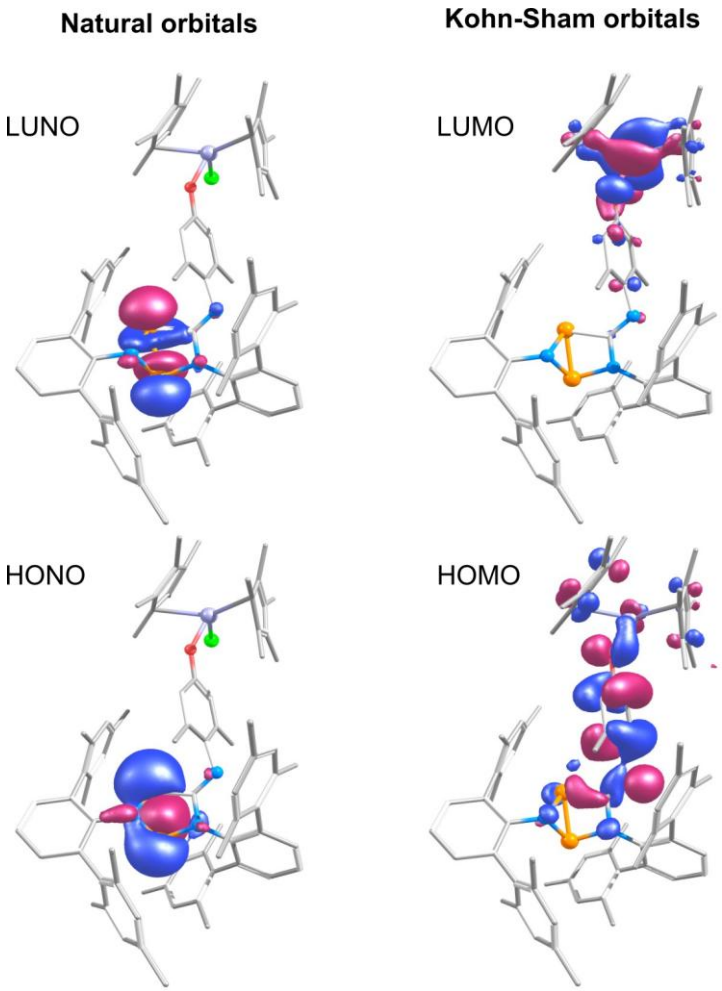

1.5 CASSCF computations on Tetraradicals

The delocalized and localized orbitals included in the CASSCF(4,4) active spaces for the Zr/Ti- Tetraradical and Zr/Ti- BisHousane systems are illustrated, and their occupation numbers are provided.

Figure S56. CASSCF(4,4)/def2-TZVP//PBE-D3/def2-TZVP orbitals (isovalue = 0.03) of the **Zr-Tetraradical**.

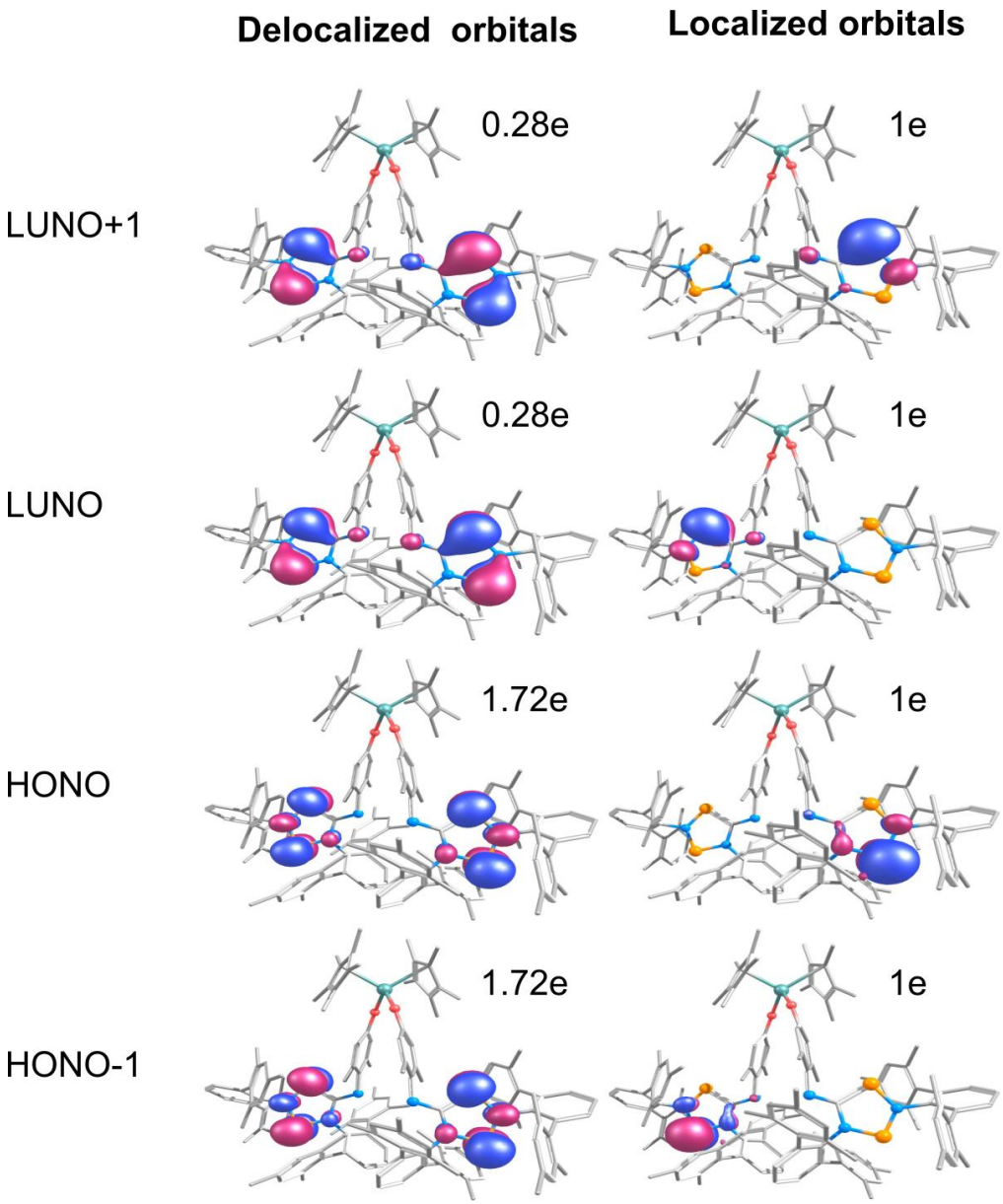

Figure S57. CASSCF(4,4)/def2-TZVP//PBE-D3/def2-TZVP orbitals (isovalue = 0.03) of the **Zr-BisHousane**.

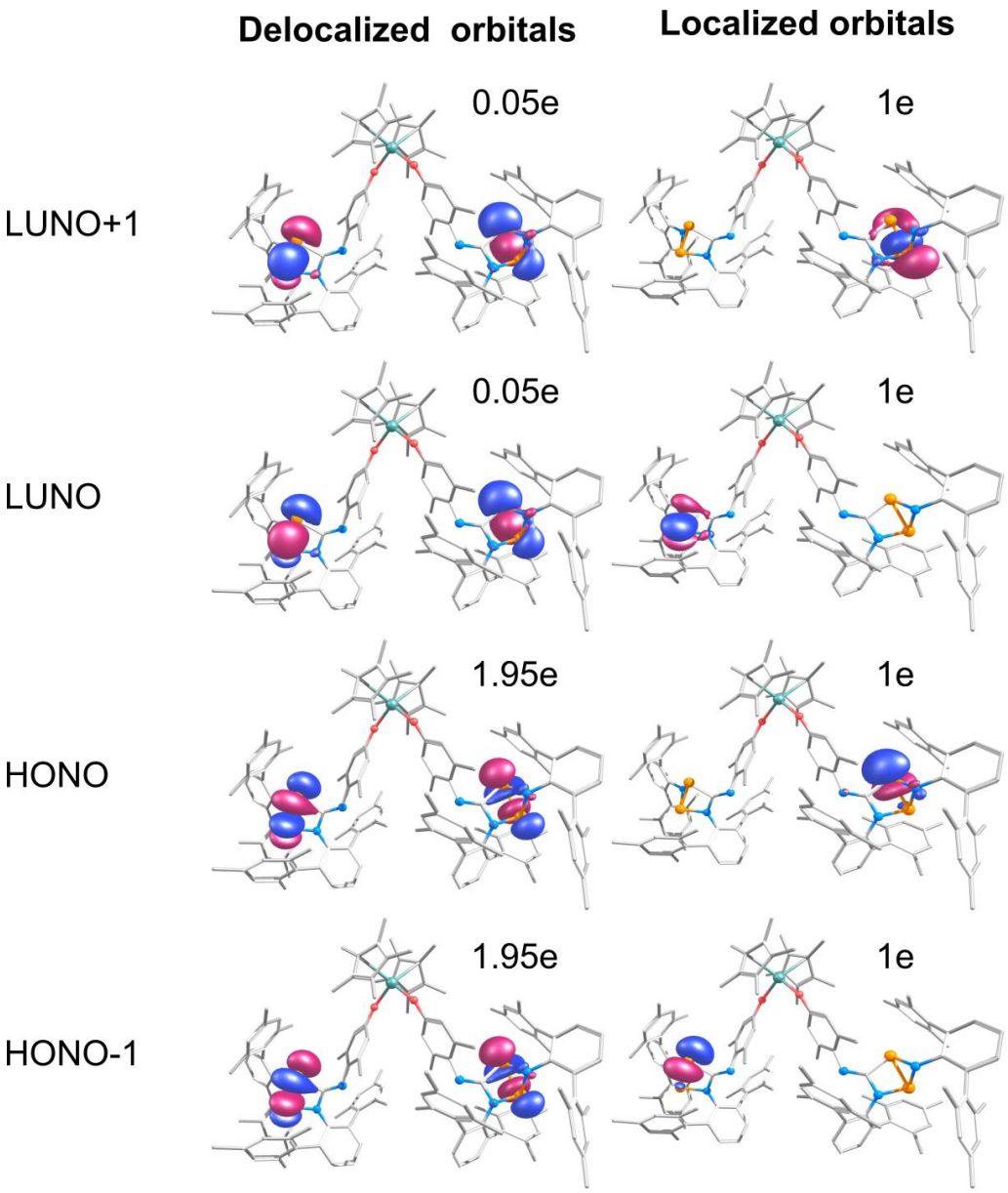

Figure S58. CASSCF(4,4)/def2-TZVP//PBE-D3/def2-TZVP orbitals (isovalue = 0.03) of the **Ti-Tetraradical**.

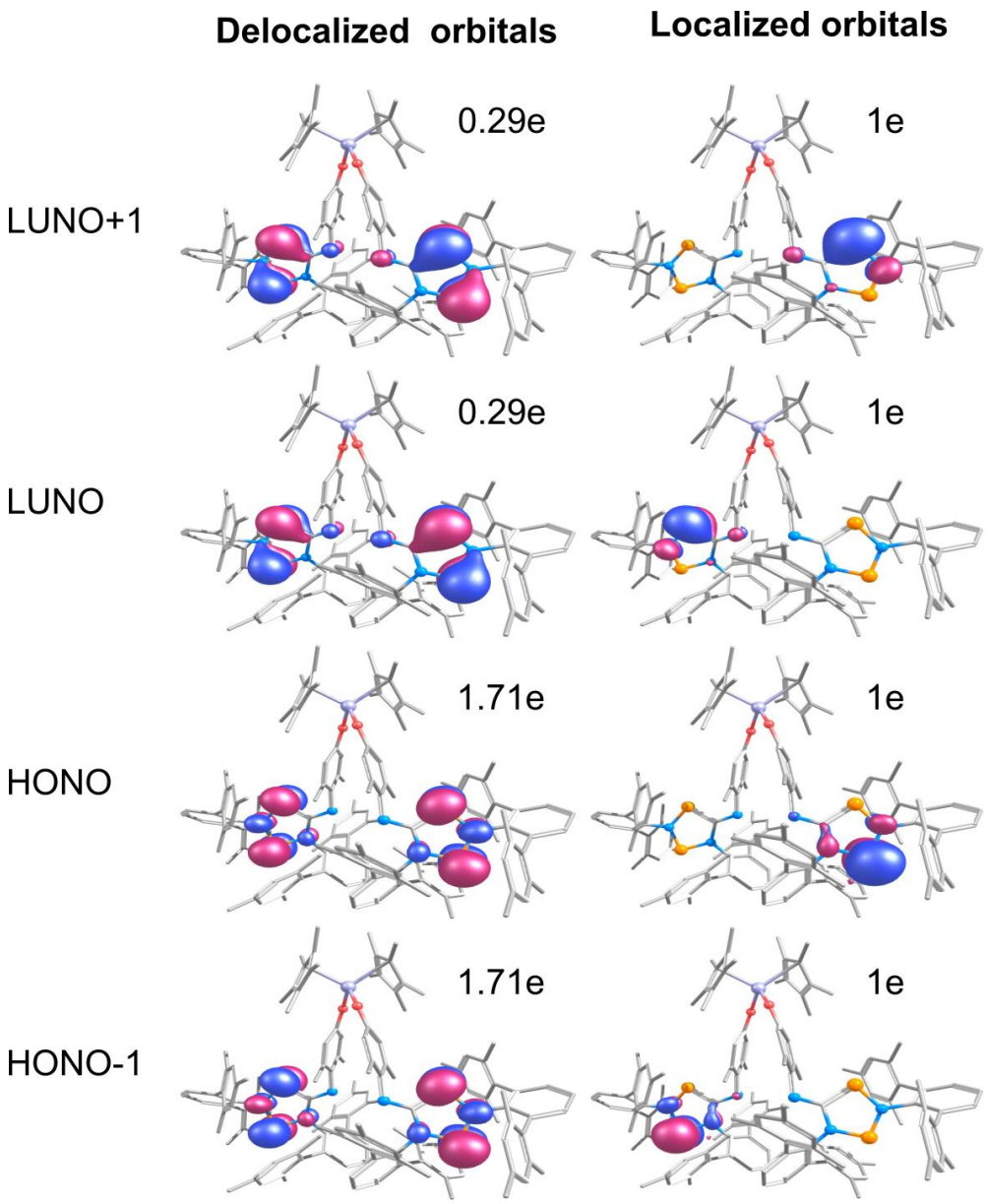

Figure S59. CASSCF(4,4)/def2-TZVP//PBE-D3/def2-TZVP orbitals (isovalue = 0.03) of the **Ti-BisHousane**.

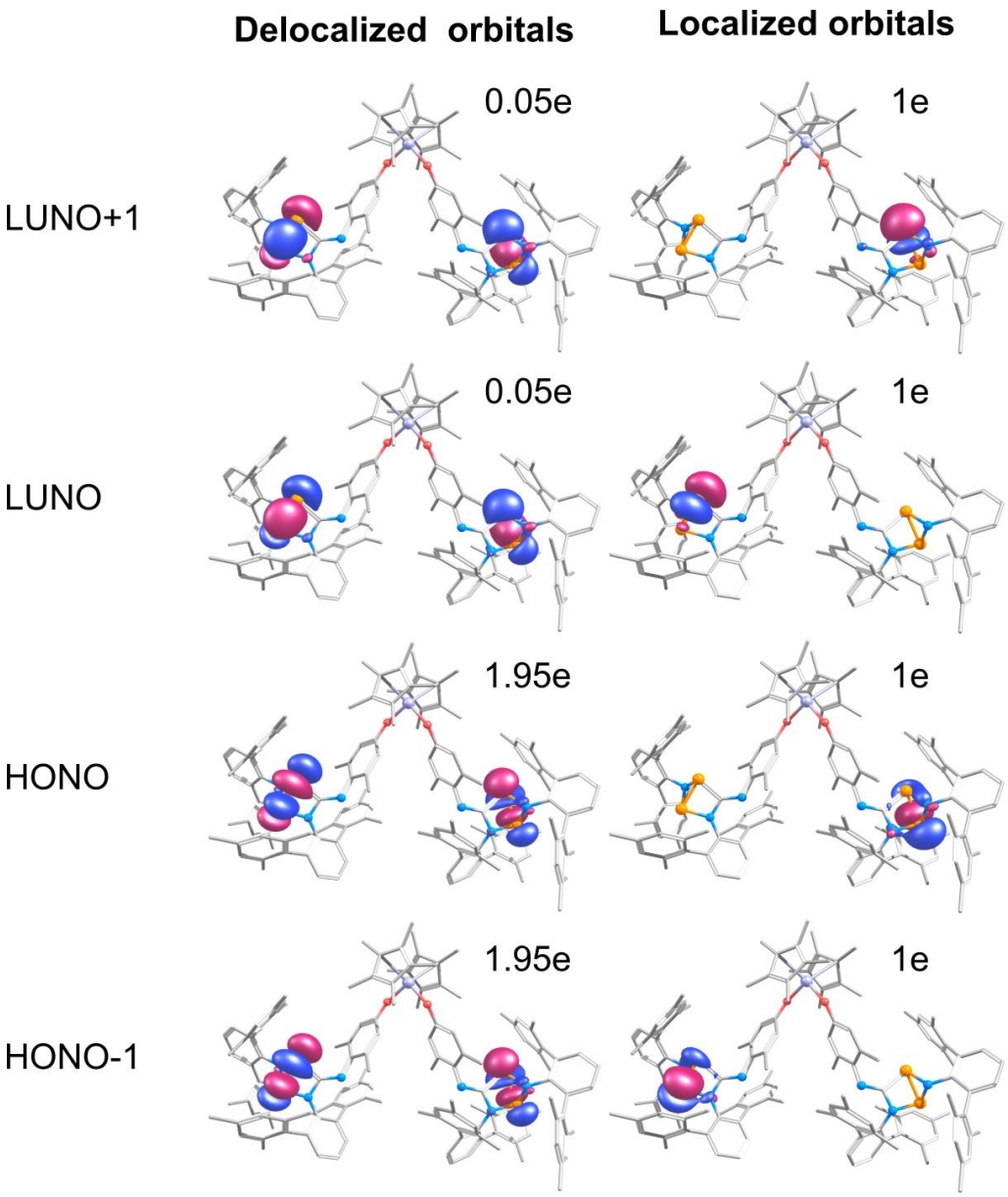

1.6 UV-Vis spectra on biradicals

Based on TD-DFT calculations, the lowest-energy electronic excitations in both the **Zr-biradical** and **Zr-housane** species (with **Ter** substituents) correspond primarily to **HOMO** → **LUMO** transitions. For the Zr-biradical, the calculated absorption occurs at 677.54 nm, which lies in the red region of the visible spectrum.

In contrast, for Zr-housane the excitation also involves electron density transfer from the HOMO to the LUMO but appears at a significantly shorter wavelength of 432.56 nm, corresponding to the blue–violet region of the spectrum. The corresponding molecular orbitals involved in these transitions and the calculated spectra are shown in Figure S23.

Figure S60. Calculated UV-Vis spectra for **Zr-biradical** and **Zr-housane** with **Ter** side groups (PBE0-D3BJ/def2-TZVP in Gaussian 16), electron density transfer: red → blue.

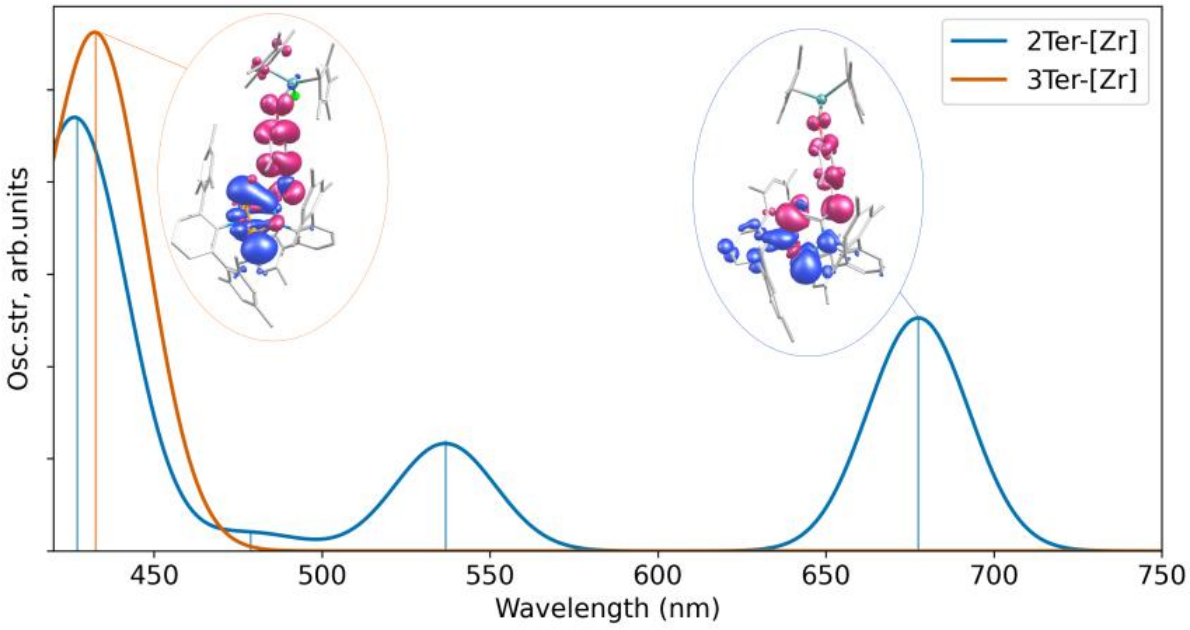

For the model system with **H** substituents, TD-DFT calculations show that the lowest-energy excitation of the **Zr-biradical** corresponds to a **HOMO–1** → **LUMO** transition at 531.88 nm, which lies in the green region of the visible spectrum, whereas the **Zr-housane** species exhibits a **HOMO** → **LUMO** transition at 430.24 nm in the blue–violet region of the visible spectrum (Figure S24).

Figure S61. Calculated UV-Vis spectra for **Zr-biradical** and **Zr-housane** with **H** side groups (PBE0-D3BJ/def2-TZVP in gaussian 16), electron density transfer: red → blue.

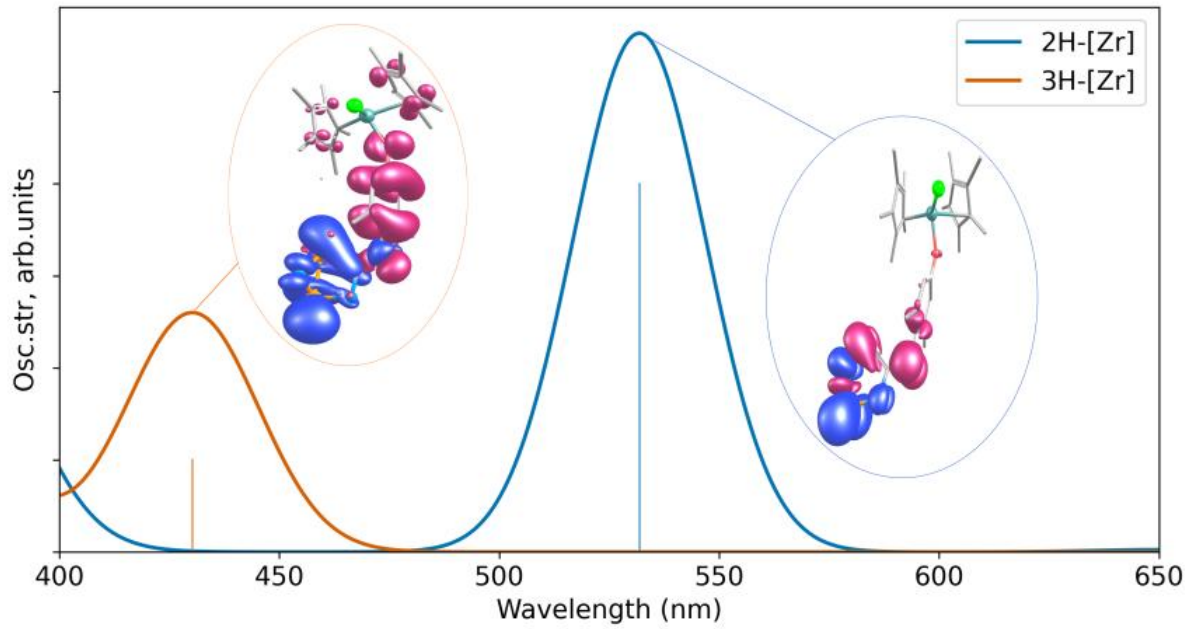

TD-DFT calculations indicate that the lowest-energy excitations of both the **Ti-biradical** and **Ti-housane** (with **Ter** substituents) correspond to **HOMO → LUMO** transitions, with calculated absorptions at 687.48 nm and 506.27 nm, which lie in the red and green regions of the visible spectrum, respectively (Figure S25).

Figure S62. Calculated UV-Vis spectra for **Ti-biradical** and **Ti-housane** with **Ter** side groups (PBE0-D3BJ/def2-TZVP in gaussian 16), electron density transfer: red → blue.

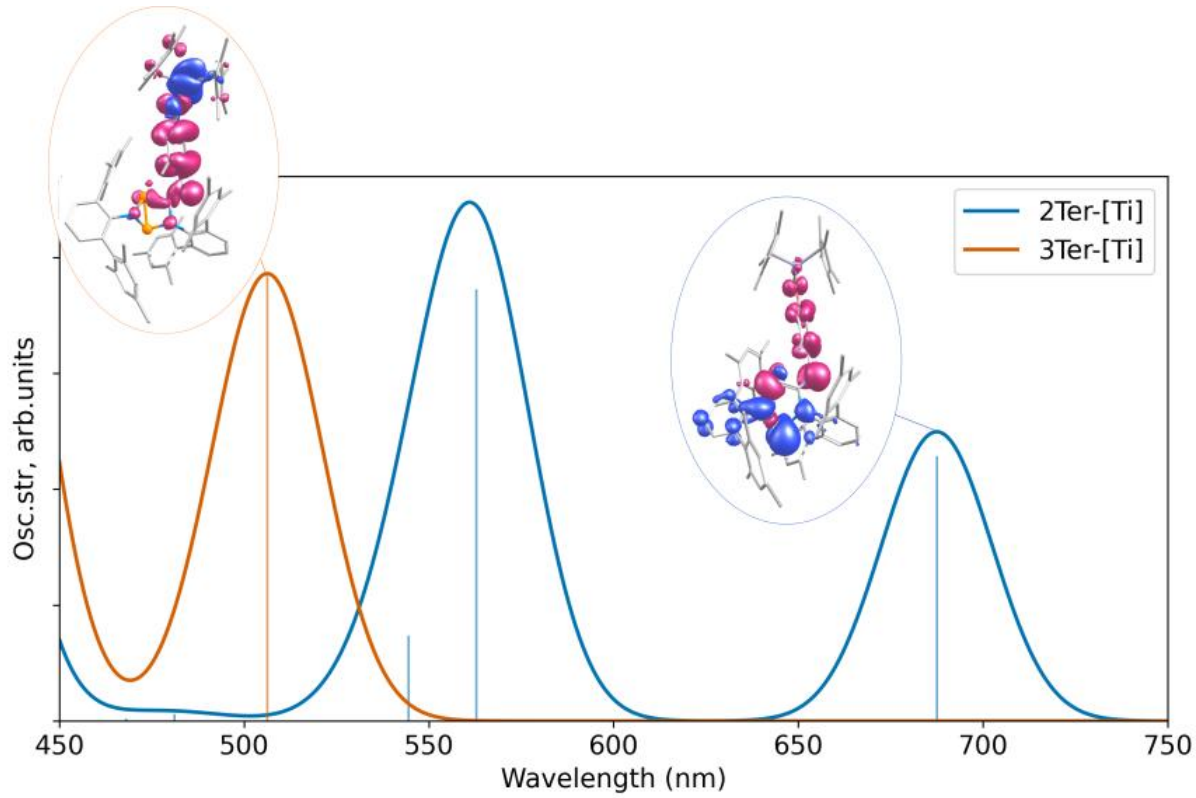

For the model system with H substituents, TD-DFT calculations show that the lowest-energy excitation of the **Ti-biradical** corresponds to a **HOMO–1 → LUMO** transition at 532.84 nm, which lies in the green region, whereas the **Ti-housane** species exhibits a **HOMO → LUMO** transition at 503.17 nm in the green region of the visible spectrum (Figure S26).

Figure S63. Calculated UV-Vis spectra for **Ti-biradical** and **Ti-housane** with **H** side groups (PBE0-D3BJ/def2-TZVP in gaussian 16), electron density transfer: red → blue.

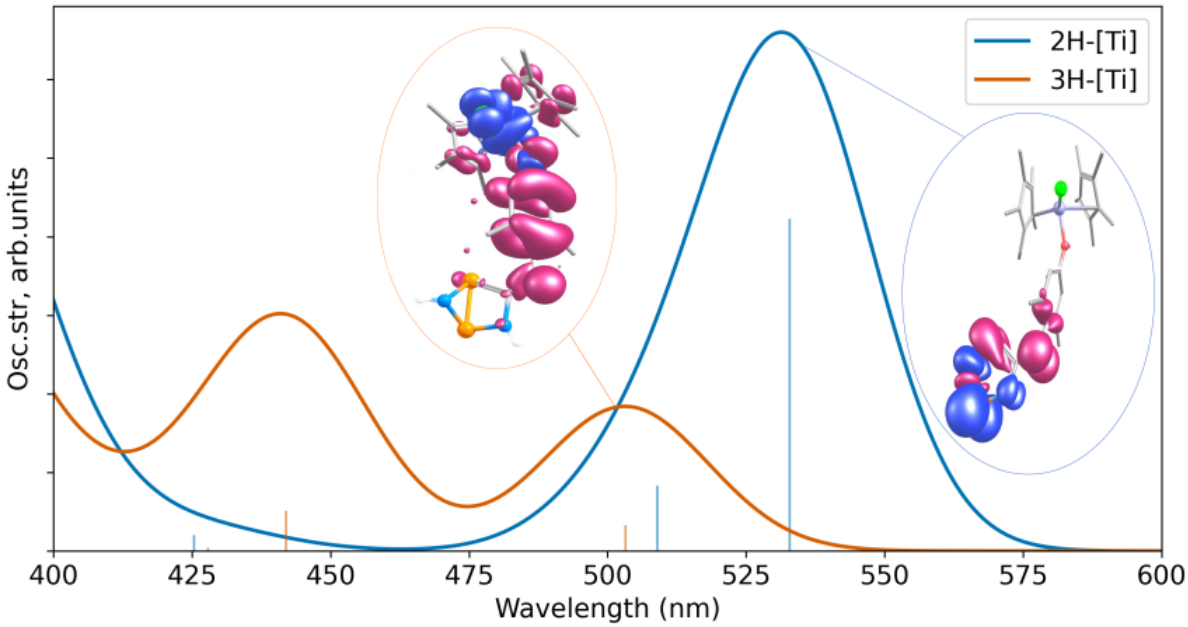

1.7 UV-Vis spectra on tetraradicals

TD-DFT calculations on the **Zr-Tetraradical** and **Zr-BisHousane** indicate that the lowest-energy excitations in both species correspond primarily to **HOMO → LUMO** transitions. The Zr-Tetraradical exhibits a calculated absorption at 609.47 nm in the red region of the visible spectrum, whereas the Zr-BisHousane absorbs at 447.69 nm in the blue–violet region. Analysis of the corresponding NTOs shows that the excitations, dominated by the largest coefficients, involve primarily HOMO → LUMO electron density transfer, and the calculated spectra are shown in Figure S27.

Figure S64. Calculated UV-Vis spectra for **Zr-Tetraradical** and **Zr-BisHousane** (PBE0-D3BJ/def2-TZVP in gaussian 16), electron density transfer: red → blue.

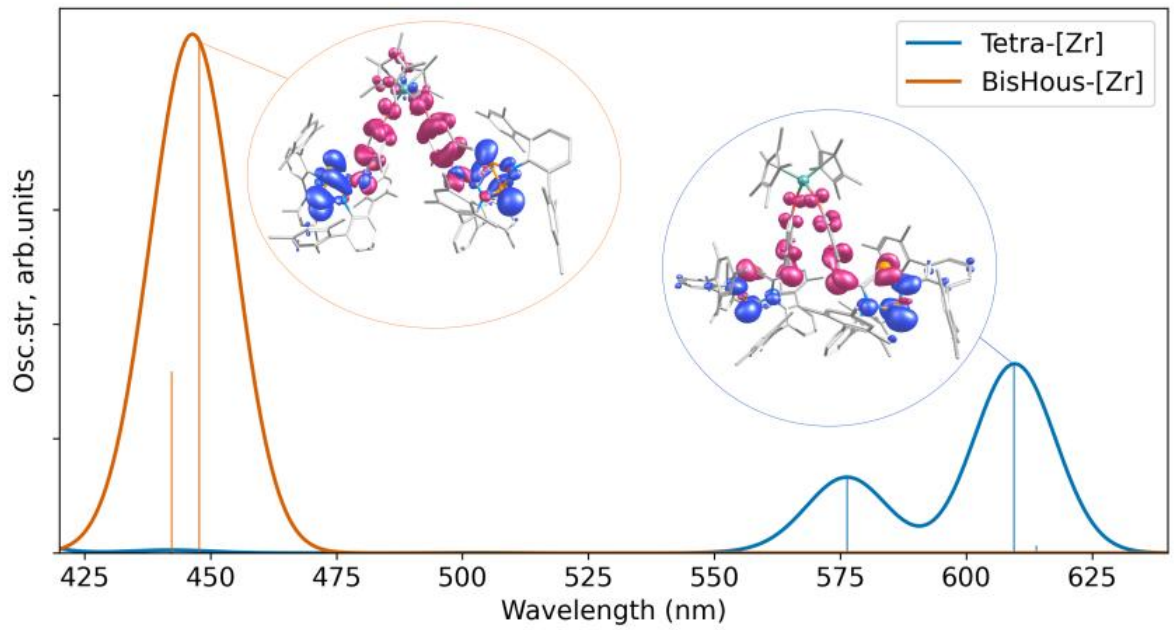

TD-DFT calculations on the **Ti-tetraradical** and **Ti-BisHousane** indicate that the lowest-energy excitations correspond primarily to **HOMO** → **LUMO** transitions. The Ti-Tetraradical absorbs at 629.66 nm in the red region, whereas the Ti-BisHousane absorbs at 517.53 nm in the blue–violet region. Analysis of the NTOs shows that these excitations, dominated by the largest coefficients, involve primarily HOMO → LUMO electron density transfer (Figure S28).

Figure S65. Calculated UV-Vis spectra for Ti-Tetraradical and Ti-BisHousane (PBE0-D3BJ/def2-TZVP in gaussian 16), electron density transfer: red → blue.

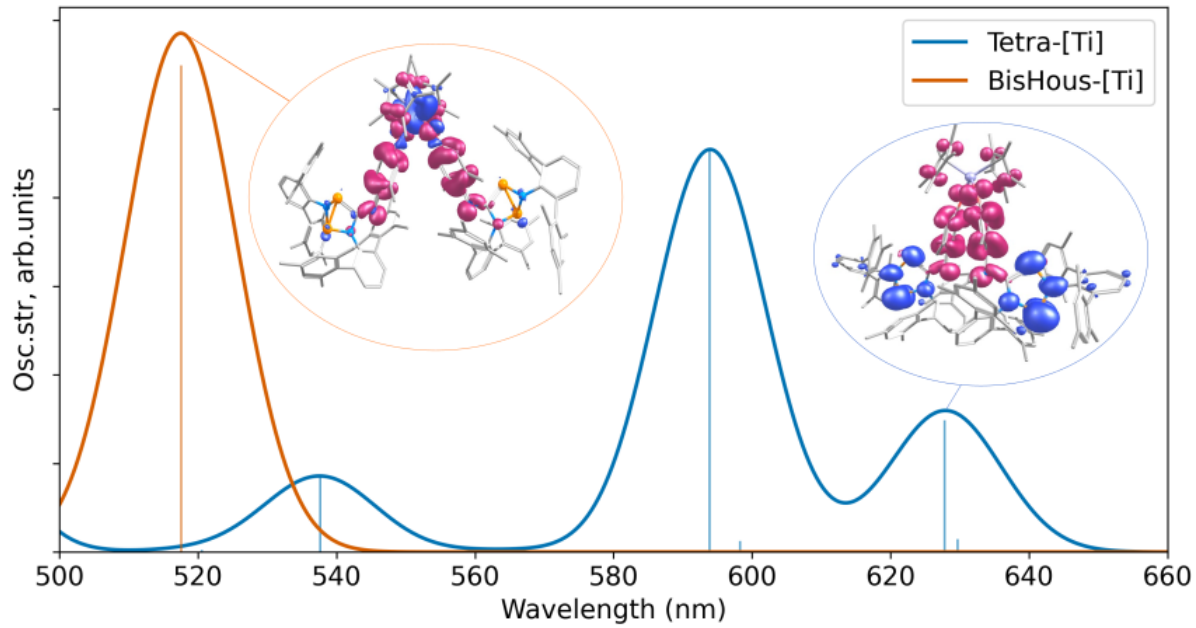

1.8 CO_2 addition

Figure S66. Gibbs free energy profile for the **CO_2** addition to **1Ter** (four-membered ring biradical) calculated at the PBE-D3/def2-TZVP level of theory.

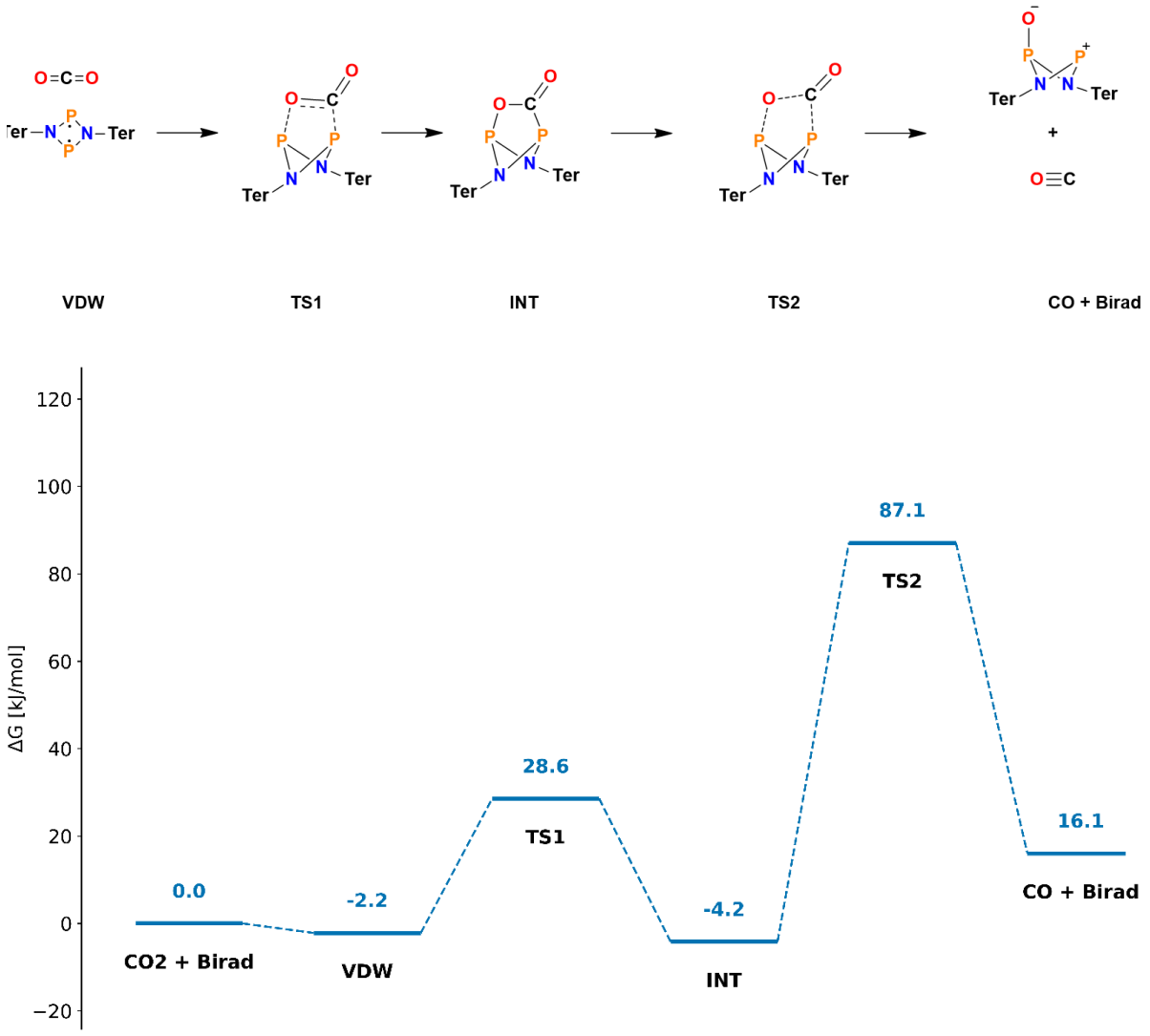

Table S9. Relative and absolute energies for the **CO_2** addition to **1Ter**

	PBE-D3BJ/def2-TZVP			DLPNO-CCSD(T)/def2-TZVP//PBE-D3BJ/def2-TZVP				
Points	G° [Hartree]	ΔG° [KJ/mol] (p° = 1 atm)	ΔG° [KJ/mol] (c° = 1 mol/L)	E_CCSD(T) [Hartree]	G-E(el)	G° [Hartree]	ΔG° [KJ/mol] (p° = 1 atm)	ΔG° [KJ/mol] (c° = 1 mol/L)
CO2 + 4mem (Ter sides)	-2837.2486	0.00	0.00	-2835.21	0.73	-2834.4776	0.00	0.00
VDW	-2837.2464	5.74	-2.17	-2835.22	0.75	-2834.4649	33.20	25.29
TS1	-2837.2347	36.47	28.56	-2835.20	0.75	-2834.4424	92.25	84.34
INT	-2837.2472	3.76	-4.15	-2835.22	0.75	-2834.4689	22.77	14.86
TS2	-2837.2124	95.02	87.11	-2835.19	0.75	-2834.4368	107.04	99.13
Product + Co	-2837.2425	16.05	16.05	-2835.21	0.73	-2834.4771	1.22	1.22
VDW (Product with Co)	-2837.2320	43.64	43.64					

Figure S67. Gibbs free energy profile for the **CO_2** addition to **Ti-mono-biradical** (four-membered ring biradical) calculated at the PBE-D3/def2-TZVP level of theory (c° = 1 mol/L).

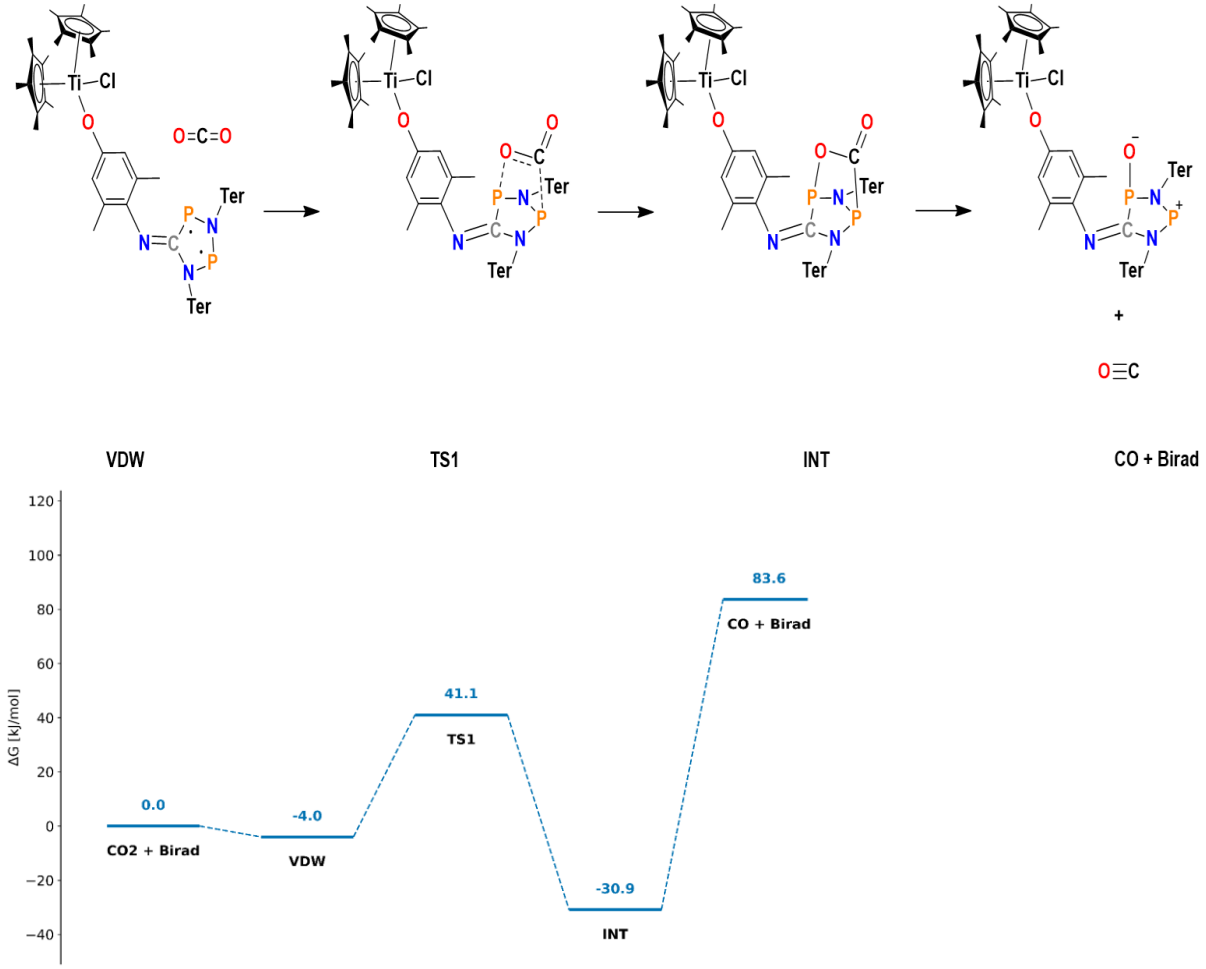

Table S10. Relative and absolute energies for the **CO_2** addition to **Ti-mono-biradical**

	PBE-D3BJ/def2-TZVP		
Points	G° [Hartree]	ΔG° [KJ/mol] (p° = 1 atm)	ΔG° [KJ/mol] (c° = 1 mol/L)
5mem (Ter sides and CN-Ti) + CO2	-5403.0484	0.00	0.00
VDW	-5403.0469	3.90	-4.01
TS1	-5403.0298	48.99	41.08
INT	-5403.0572	-22.98	-30.89
TS2	-	-	-
Product + Co	-5403.0166	83.64	83.64
VDW (Product with Co)	-5403.0074	107.61	107.61

Figure S68. Gibbs free energy profile for the **CO_2** addition to **Zr-mono-biradical** (four-membered ring biradical) calculated at the PBE-D3/def2-TZVP level of theory (c° = 1 mol/L).

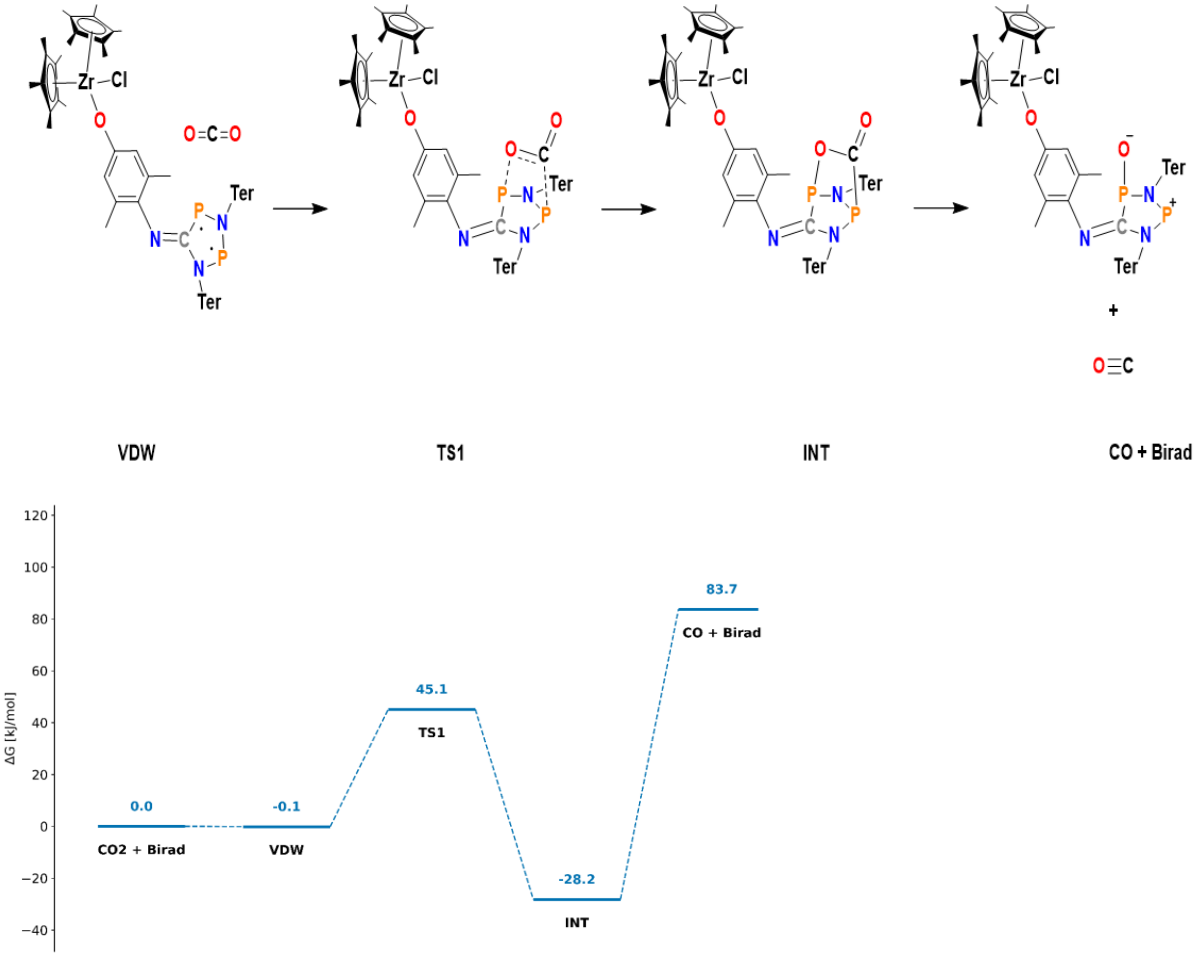

Table S11. Relative and absolute energies for the **CO_2** addition to **Ti-mono-biradical**

	PBE-D3BJ/def2-TZVP		
Points	G° [a.u.]	ΔG° [KJ/mol] (p° = 1 atm)	ΔG° [KJ/mol] (c° = 1 mol/L)
5mem (Ter sides and CN-Zr) + CO_2	-4600.9093	0.00	0.00
VDW	-4600.9063	7.79	-0.12
TS1	-4600.8891	53.05	45.14
INT	-4600.9170	-20.31	-28.22
TS2	-	-	-
Product + Co	-4600.8774	83.68	83.68
VDW (Product with Co)	-4600.8677	109.23	109.23

Figure S69. Gibbs free energy profile for the reaction of **CO_2** addition to model system **2H-[Zr]** (five-membered ring biradical) calculated at the PBE-D3/def2-TZVP level of theory (c° = 1 mol/L).

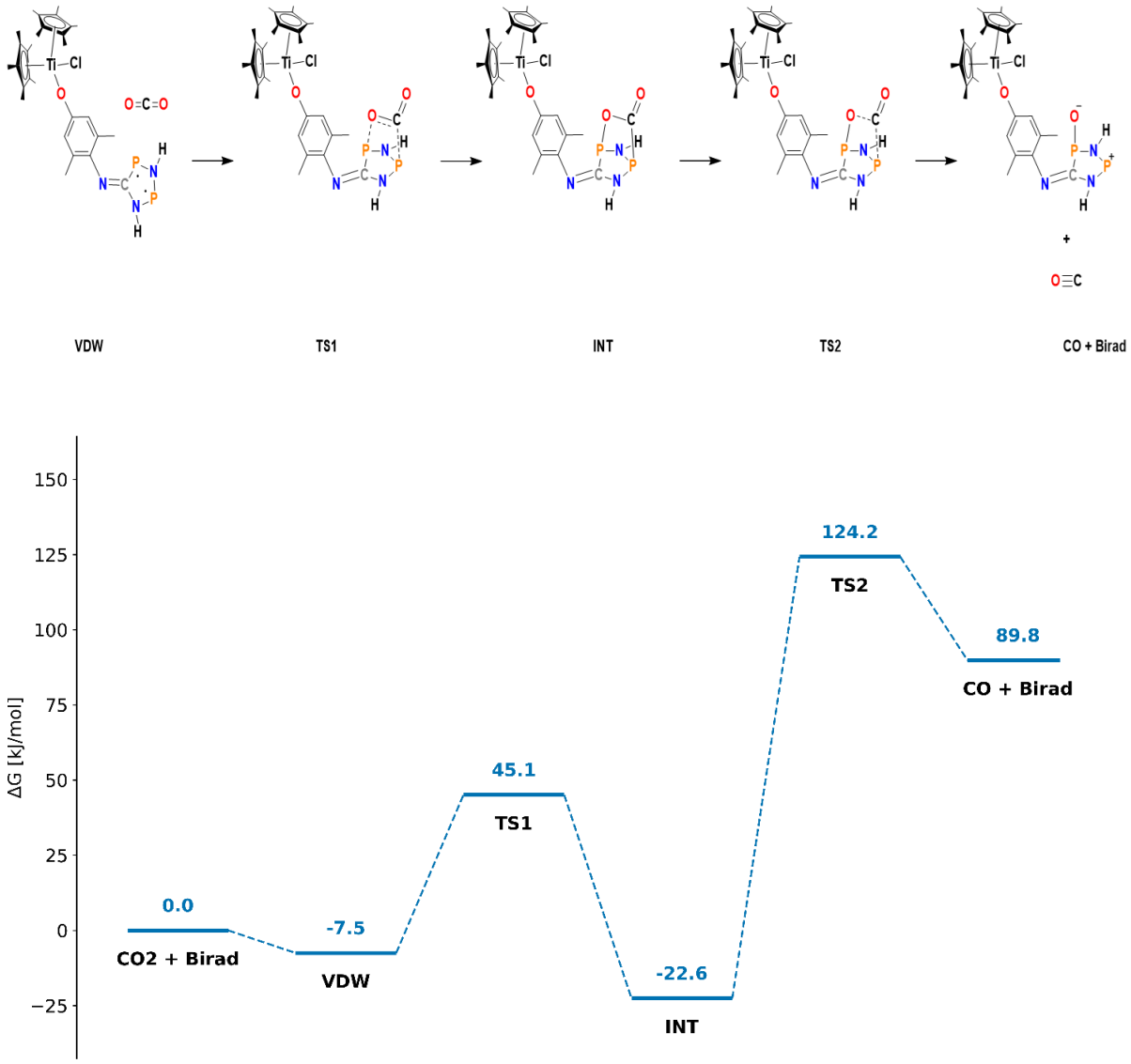

Table S12. Relative and absolute energies for the **CO_2** addition to **2H-[Ti]**

	PBE-D3BJ/def2-TZVP			DLPNO-CCSD(T)/def2-TZVP//PBE-D3BJ/def2-TZVP				
Points	G° [Hartree]	ΔG° [KJ/mol] (p° = 1 atm)	ΔG° [KJ/mol] Solution phase (c° = 1 mol/L)	E_CCSD(T) [Hartree]	G-E(el)	G° [Hartree]	ΔG° [KJ/mol] (p° = 1 atm)	ΔG° [KJ/mol] Solution phase (c° = 1 mol/L)
5mem (H sides and CNTi) + CO2	-3547.3498	0.00	0.00	-3544.99722	0.53548	-3544.46174	0.00	0.00
VDW	-3547.3497	0.41	-7.50	-3545.00230	0.55153	-3544.45077	28.80	20.89
TS1	-3547.3296	52.97	45.06	-3544.97382	0.55434	-3544.41948	110.96	103.05
INT	-3547.3554	-14.68	-22.59	-3545.01839	0.55603	-3544.46236	-1.63	-9.54
TS2	-3547.2995	132.15	124.24					
Product + Co	-3547.3156	89.85	89.85					
VDW (Product with Co)	-3547.3070	112.43	112.43	-3544.95939	0.54639	-3544.41300	127.97	127.97

Figure S70. Gibbs free energy profile for the reaction of **CO_2** addition to **2H-[Zr]** (five-membered ring biradical) calculated at the PBE-D3/def2-TZVP level of theory.

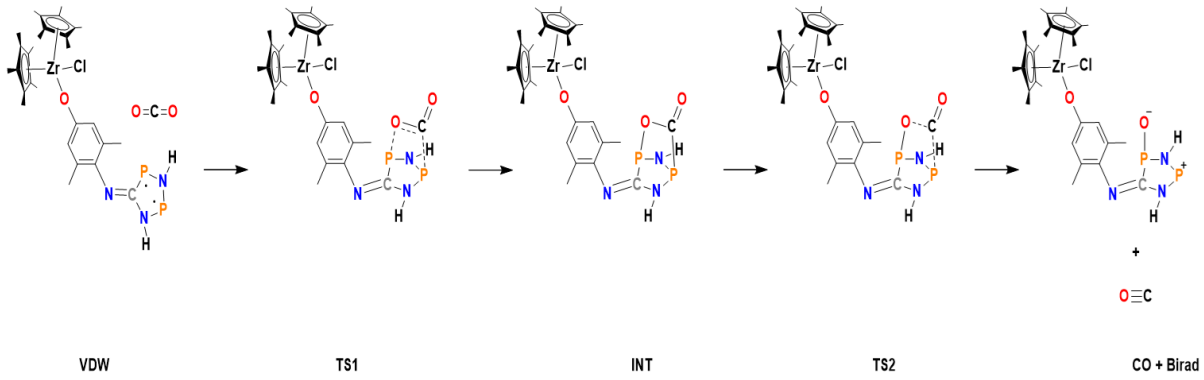

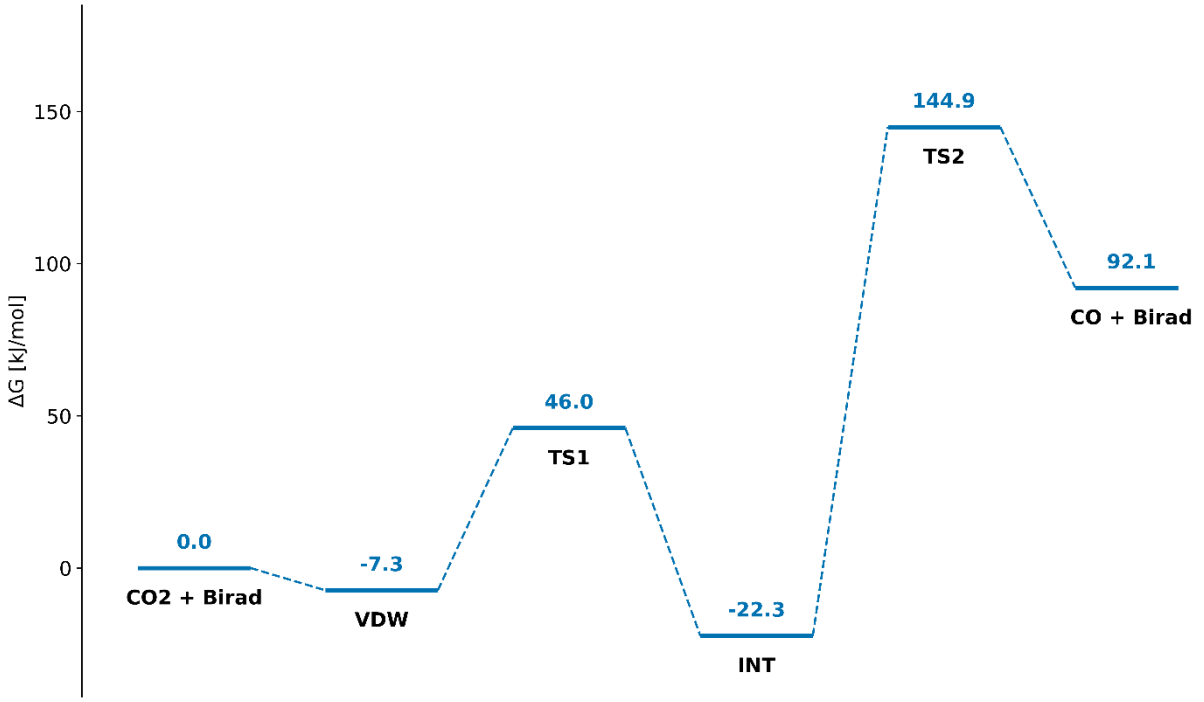

Table S13. Relative and absolute energies for the **CO_2** addition to **2H-[Zr]**

	PBE-D3BJ/def2-TZVP			DLPNO-CCSD(T)/def2-TZVP//PBE-D3BJ/def2-TZVP				
Points	G° [Hartree]	ΔG° [KJ/mol] (p° = 1 atm)	ΔG° [KJ/mol] Solution phase (c° = 1 mol/L)	E_CCSD(T) [Hartree]	G-E(el)	G° [Hartree]	ΔG° [KJ/mol] (p° = 1 atm)	ΔG° [KJ/mol] Solution phase (c° = 1 mol/L)
5mem (H sides and CNZr) + CO2	-2745.2111	0.00	0.00	-2743.11864	0.53314	-2742.58549	0.00	0.00
VDW	-2745.2109	0.56	-7.35	-2743.12349	0.54919	-2742.57430	29.40	21.49
TS1	-2745.1905	53.90	45.99	-2743.09474	0.55223	-2742.54251	112.86	104.95
INT	-2745.2166	-14.40	-22.31	-2743.13943	0.55374	-2742.58569	-0.50	-8.41
TS2	-2745.1529	152.84	144.93					
Product + Co	-2745.1760	92.08	92.08					
VDW (Product with Co)	-2745.1674	114.69	114.69	-2743.08000	0.54426	-2742.53574	130.64	130.64

1.9 Summary of calculated data

Table S14. Summary of calculated data for **model systems** with **H** sides, including electronic energies, thermal corrections, chemical shifts, total nuclear spin-spin coupling, and biradical character. (Opt. method: PBE-D3/def2-TZVP)

Compound	E_{tot}[a]	E^{tc}[b]	$E_{CCSD(T)}$[c]	T_1	δ (P1) [ppm]	δ (P2) [ppm]	J (P-P) [HZ]	β
CN-[Ti]	-2566.2956	0.5128	-2564.2788	0.013	-	-	-	-
CN-[Zr]	-1764.1544	0.5097	-1762.3997	0.011	-	-	-	-
1H	-793.0526	0.0044	-792.3374	0.012	336.6307	336.6464	393.85	25 %
2H-[Ti]	-3359.4145	0.5449	-3356.6649	0.015	316.2856	282.5210	209.145	29%
2H-[Zr]	-2557.2734	0.5425	-2554.7863	0.01	316.4262	283.2575	209.784	29%
3H-[Ti]	-3359.3971	0.5441	-3356.6479	0.014	-61.4647	-146.1407	-77.8701	3%
3H-[Zr]	-2557.2560	0.5417	-2554.7689	0.012	-62.3327	-146.3357	-78.0209	3%
VDW1^{H}-[Ti]	-3359.3571	0.5411	-3356.6229	0.014	329.2569	327.1467	395.898	25%
VDW2^{H}-[Ti]	-3359.3622	0.5384	-3356.6286	0.014	331.6815	331.8722	373.266	24%
VDW1^{H}-[Zr]	-2557.2162	0.5375	-2554.7437	0.011	335.2349	320.5272	392.998	25%
VDW2^{H}-[Zr]	-2557.2171	0.5358	-2554.7398	0.011	227.1617	314.6746	300.319	24%
INT1^{H}-[Ti]	-3359.3721	0.5431	-3356.6250	0.014	435.4594	428.9304	8.02425	1%
INT2^{H}-[Ti]	-3359.3786	0.5389	-3356.6274	0.015	391.4021	5.1196	-28.934	2%
INT1^{H}-[Zr]	-2557.2313	0.5415	-2554.7471	0.012	435.5871	425.9167	8.23299	1%
INT2^{H}-[Zr]	-2557.2369	0.5370	-2554.7479	0.013	7.3584	392.0186	-29.2549	2%
TS1^{H}-[Ti]	-3359.3527	0.5407	-3356.6098	0.014	-	-	-	19%
TS2^{H}-[Ti]	-3359.3090	0.5404	-3356.5495	0.014	-	-	-	4%
TS3^{H}-[Ti]	-3359.3587	0.5383	-3356.6152	0.014	-	-	-	24%
TS4^{H}-[Ti]	-3359.3407	0.5384	-3356.5820	0.015	-	-	-	2%
TS5^{H}-[Ti]	-3359.3594	0.5432	-3356.6049	0.015	-	-	-	3%
TS1^{H}-[Zr]	-2557.2116	0.5382	-2554.7311	0.011	-	-	-	19%
TS2^{H}-[Zr]	-2557.1676	0.5377	-2554.6709	0.012	-	-	-	4%
TS3^{H}-[Zr]	-2557.2172	0.5360	-2554.7358	0.011	-	-	-	24%
TS4^{H}-[Zr]	-2557.1994	0.5360	-2554.7025	0.013	-	-	-	1%
TS5^{H}-[Zr]	-2557.2179	0.5409	-2554.7267	0.013	-	-	-	3%

[a] Total SCF energy in a.u.; [b] thermal correction to Gibbs energy in a.u. (298 K unless stated otherwise); [c] single-point DLPNO-CCSD(T)/def2-TZVP energy. The point group (PG) for the 4-membered biradical (1H) is D_2, and C_1 for all other species.

Table S15. Summary of calculated data for **biradical** with **Ter** sides, including electronic energies, thermal corrections, chemical shifts, total nuclear spin-spin coupling, and biradical character. (Single-point PBE-D3/def2-TZVP)

Compound	E_{tot}[a]	E^{tc}[b]	δ (P1) [ppm]	δ (P2) [ppm]	J (P-P) [HZ]
CN-[Zr]	-1764.1513	0.51015	-	-	-
CN-[Ti]	-2566.2925	0.51348	-	-	-
1Ter	-2649.5100	0.74203	305.5435	256.3288	335.619
2Ter-[Ti]	-5215.8480	1.29156	308.2554	312.1449	233.564
2Ter-[Zr]	-4413.7067	1.28907	335.0989	332.6151	302.235
3Ter-[Ti]	-5215.8364	1.29206	-141.0017	-17.6889	-38.1194
3Ter-[Zr]	-4413.6954	1.28931	-124.2454	-4.2838	-33.1574
VDW1^{Ter}-[Ti]	-5215.8160	1.28641	323.4416	319.4928	348.461
VDW2 ^{Ter} -[Ti]	-5215.8065	1.28742	319.9744	315.2738	370.848
VDW1 ^{Ter} -[Zr]	-4413.6754	1.28259	332.1419	320.3170	357.412
VDW2 ^{Ter} -[Zr]	-4413.6655	1.28403	333.6302	337.1059	395.177
INT1 ^{Ter} -[Ti]	-5215.8109	1.28790	345.0032	333.6338	-8.33506
INT2 ^{Ter} -[Ti]	-5215.8218	1.28742	17.8706	317.0721	-8.69311
INT1 ^{Ter} -[Zr]	-4413.6917	1.28520	345.0032	333.6338	-8.33506
INT2 ^{Ter} -[Zr]	-4413.6806	1.28496	17.8706	317.0721	-8.69311
TS1 ^{Ter} -[Ti]	-5215.8109	1.28684	-	-	-
TS2 ^{Ter} -[Ti]	-5215.7551	1.28673	-	-	-
TS3 ^{Ter} -[Ti]	-5215.8030	1.28509	-	-	-
TS5 ^{Ter} -[Ti]	-5215.8045	1.29013	-	-	-
TS1 ^{Ter} -[Zr]	-4413.6696	1.28565	-	-	-
TS5 ^{Ter} -[Zr]	-4413.6631	1.28727	-	-	-

[a] Total SCF energy in a.u.; [b] thermal correction to Gibbs energy in a.u. (298 K unless stated otherwise); The point group (PG) for the 4-membered biradical (1Ter) is D_2, and C_1 for all other species.

Table S16. Summary of calculated data for **Tetraradical** and **BisHousane**, including electronic energies, thermal corrections, and occupation numbers. (Opt. method: PBE-D3/def2-TZVP)

Compound	E_{tot}[a]	E^{tc}[b]	n_{occ} (LUNO)[c]	n_{occ} (LUNO+1) [d]
Zr-Linker	-1781.4385	0.64185	-	-
Ti-Linker	-2583.5795	0.64581	-	-
Zr-Tetraradical	-7080.5712	2.19905	0.28	0.28
Ti-Tetraradical	-7882.7114	2.20146	0.29	0.29
Zr-BisHousane	-7882.6773	2.19439	0.05	0.05
Ti-BisHousane	-7080.5350	2.19534	0.05	0.05

[a] Total SCF energy in a.u.; [b] thermal correction to Gibbs energy in a.u. (298 K unless stated otherwise); [c]occupation number for LUNO; [d]occupation number for LUNO+1. The point group (PG) for the four-membered ring biradical (1Ter) is D_2, and C_2 for all other species.

Table S17. Summary of calculated data for **biradical** with **Ter** sides and **CN-R (R= Methyl, Phenyl, Trichloromethyl, Trichlorobenzene)**, including electronic energies, thermal corrections. (Single-point PBE-D3/def2-TZVP)

Compound	E_{tot}[a]	E^{tc}[b]	$E_{CCSD(T)}$[c]	T_1
CN-Me	-132.5985	0.01962	-132.4828	0.015
CN-CCl_3	-1510.8704	-0.01557	-1509.8306	0.013
CN-Ph	-324.1748	0.06582	-323.8540	0.012
CN-$PhCl_3$	-1702.4754	0.03144	-1701.2285	0.012
VDW_1^{Ter}-Me	-2782.1131	0.78564	-2779.3590	0.011
VDW_2^{Ter}-Me	-2782.0998	0.78524	-2779.3569	0.012
VDW_1^{Ter}-CCl_3	-4160.3908	0.75553	-4156.6981	0.011
VDW_2^{Ter}-CCl_3	-4160.3784	0.75412	-4156.7008	0.011
VDW_1^{Ter}-Ph	-2973.6909	0.83525	-2970.7275	0.011
VDW_2^{Ter}-Ph	-2973.6835	0.83527	-2970.7217	0.011
VDW_1^{Ter}-$PhCl_3$	-4351.9935	0.80209	-4348.1051	0.011
VDW_2^{Ter}-$PhCl_3$	-4351.9846	0.80192	-4348.0971	0.011
INT_1^{Ter}-Me	-2782.1331	0.78958	-2779.3672	0.012
INT_2^{Ter}-Me	-2782.1243	0.78623	-2779.3427	0.011
INT_1^{Ter}- CCl_3	-4160.4300	0.75772	-4156.7372	0.012
INT_2^{Ter}- CCl_3	-4160.4133	0.75535	-4156.7196	0.012
INT_1^{Ter}-Ph	-2973.7193	0.83845	-2970.7512	0.012
INT_2^{Ter}-Ph	-2973.7070	0.83531	-2970.7347	0.012
INT_1^{Ter}-$PhCl_3$	-4352.0242	0.80693	-4348.1295	0.012
INT_2^{Ter}-$PhCl_3$	-4352.0108	0.80378	-4348.1144	0.012
TS_1^{Ter}-Me	-2782.1084	0.78592	-2779.3469	0.011
TS_1^{Ter}-CCl_3	-4160.3815	0.75334	-4156.6870	0.011
TS_1^{Ter}-Ph	-2973.6906	0.83487	-2970.7248	0.011
TS_1^{Ter}-$PhCl_3$	-4351.9935	0.80307	-4348.1082	0.011

Compound	E_{tot}[a]	E^{tc}[b]	$E_{CCSD(T)}$[c]	T_1
TS_2^{Ter}-Me	-2782.0603	0.78747	-2779.2821	0.012
TS_2^{Ter}-CCl_3	-4160.3876	0.75902	-4156.6804	0.013
TS_2^{Ter}-Ph	-2973.6505	0.83814	-2970.6621	0.013
TS_2^{Ter}-$PhCl_3$	-4351.9716	0.80656	-4348.0665	0.012
TS_3^{Ter}-Me	-2782.0967	0.78405	-2779.3349	0.011
TS_3^{Ter}-CCl_3	-4160.3727	0.75594	-4156.6897	0.011
TS_3^{Ter}-Ph	-2973.6573	0.83153	-2970.6874	0.014
TS_3^{Ter}-$PhCl_3$	-4351.9831	0.80235	-4348.0877	0.011
TS_4^{Ter}-Me	-2782.1121	0.78405	-2779.3400	0.012
TS_4^{Ter}-CCl_3	-4160.4024	0.75577	-4156.7100	0.012
TS_4^{Ter}-Ph	-2973.6838	0.83535	-2970.7043	0.012
TS_4^{Ter}-$PhCl_3$	-4351.9914	0.80295	-4348.0868	0.012
2Ter-Me	-2782.1495	0.78952	-2779.3844	0.013
2Ter-CCl_3	-4160.4644	0.75796	-4156.7704	0.012
2Ter-Ph	-2973.7388	0.83821	-2970.7687	0.013
2Ter-$PhCl_3$	-4352.0404	0.80678	-4348.1494	0.012

[a] Total SCF energy in a.u.; [b] thermal correction to Gibbs energy in a.u. (298 K unless stated otherwise); [c] single-point DLPNO-CCSD(T)/def2-TZVP energy. The point group (PG) for the 4-membered biradical (**1Ter**) is D_2, and C_1 for all other species.

Table S18. Summary of calculated data for the *experimental* biradical (PBE-D3/def2-TZVP): ST gaps, formation energies, beta values and occupation numbers of the LUNOs.

	Ti-Biradical	Zr-Biradical	Ti-Mono Housane	Zr-Mono Housane
β[a]	31%	31%	5%	5%
ΔG[b]	-53.83	-50.92	-22.19	-20.70
ΔE(S-T)[c]	87.97	87.94	182.14	214.91
n[d](LUNO)	0.31	0.31	0.05	0.05

[a] Biradical character; [b] Gibbs energy for the reaction shown below in KJ/mol ($c°$ = 1 mol/L); [c] singlet-triplet gap in KJ/mol; [d] occupation number (LUNO).

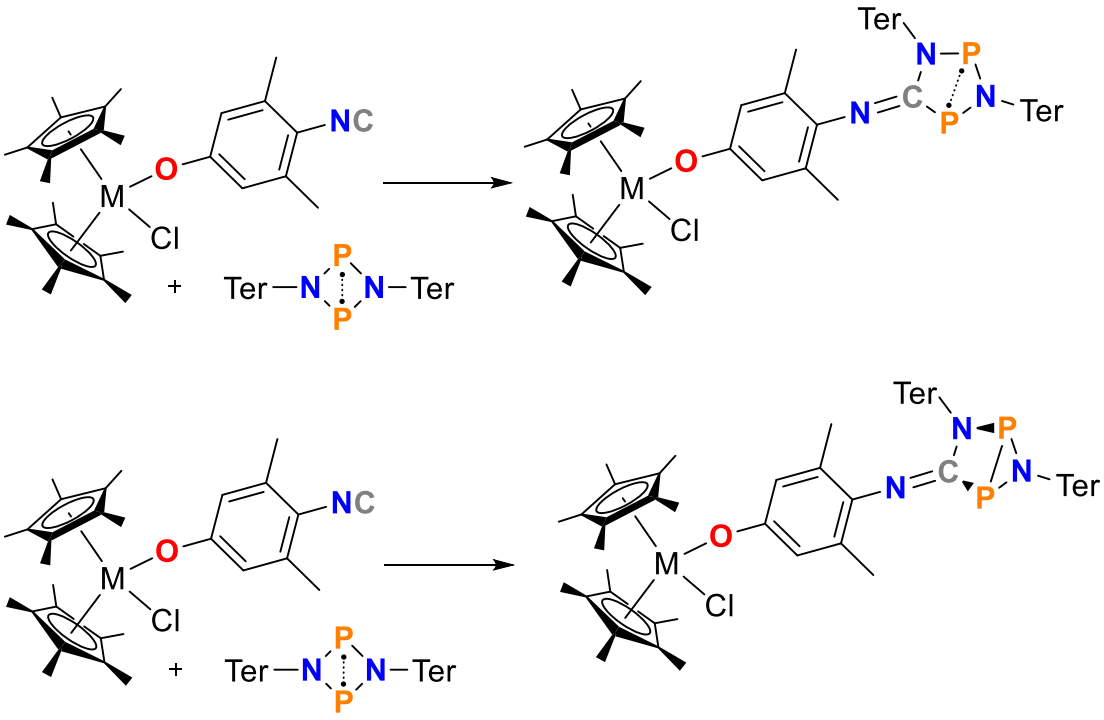

Table S19. Summary of calculated data for the *experimental* tetraradical [bis-biradical] (PBE-D3/def2-TZVP): ST/SQ gaps, formation energies, and occupation numbers of the LUNOs.

	Ti-Tetraradical	Zr-Tetraradical	Ti-Di Housane	Zr-Di Housane
ΔG[a]	-122.84	-119.76	-44.83	-36.84
ΔE(S-T)[b]	108.53	109.19	165.96	199.93
ΔE(S-Q)[c]	198.99	200.36	375.09	418.29
n[d](LUNO)	0.29	0.28	0.05	0.05
n[e](LUNO+1)	0.29	0.28	0.05	0.05

[a] Gibbs energy for the reaction shown below in KJ/mol ($c°$ = 1 mol/L); [b] singlet-triplet gap in KJ/mol; [c] singlet-quintet gap in KJ/mol; [d] occupation number (LUNO); [e] occupation number (LUNO+1).

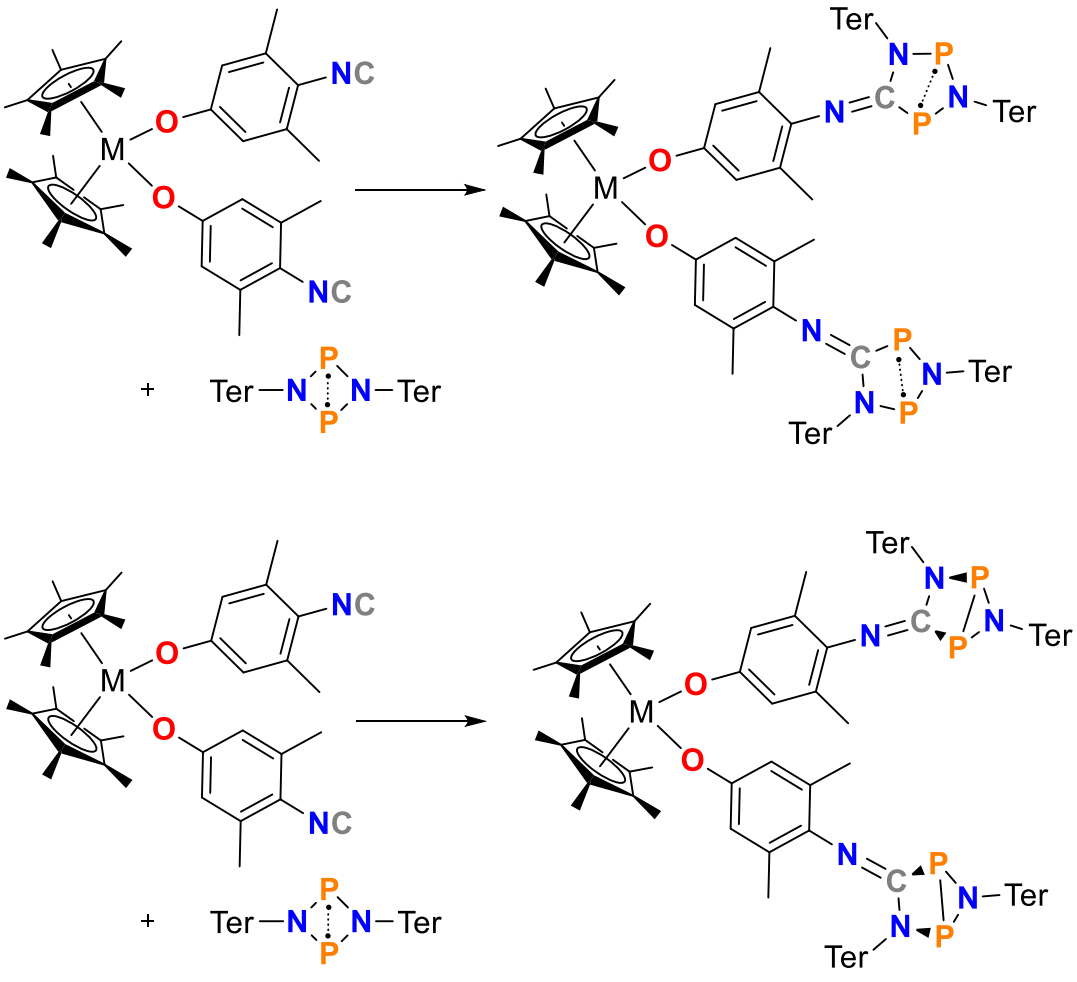

8 References

[1] T. Beweries, R. Kuzora, U. Rosenthal, A. Schulz, A. Villinger, *Angew. Chem. Int. Ed.* **2011**, *50*, 8974–8978.

[2] P. Fritz, H. AlHamwi, A. Villinger, D. Michalik, J. Bresien, F. Reiß, T. Beweries, A. Schulz, *Chem. – A Eur. J.* **2024**, *30*, e202402415.

[3] P. H. M. Budzelaar, **2006**.

[4] M. J. Frisch, G. W. Trucks, H. B. Schlegel, G. E. Scuseria, M. A. Robb, J. R. Cheeseman, G. Scalmani, V. Barone, B. Mennucci, G. A. Peterson, H. Nakatsuji, M. Caricato, X. Li, H. P. Hratchian, A. F. Izmaylov, J. Bloino, G. Zheng, J. L. Sonnenberg, M. Hada, M. Ehara, K. Toyota, R. Fukuda, J. Hasegawa, M. Ishida, T. Nakajima, Y. Honda, O. Kitao, H. Nakai, T. Vreven, J. A. Montgomery Jr., J. E. Peralta, F. Ogliaro, M. Bearpark, J. J. Heyd, E. Brothers, K. N. Kudin, V. N. Staroverov, T. Keith, R. Kobayashi, J. Normand, K. Raghavachari, A. Rendell, J. C. Burant, S. S. Iyengar, J. Tomasi, M. Cossi, N. Rega, J. M. Millam, M. Klene, J. E. Know, J. B. Cross, V. Bakken, C. Adamo, J. Jaramillo, R. Gomperts, R. E. Stratmann, O. Yazyev, A. J. Austin, R. Cammi, C. Pomelli, J. W. Ochterski, R. L. Martin, K. Morokuma, V. G. Zakrezewski, G. A. Voth, P. Salvador, J. J. Dannenberg, S. Dapprich, A. D. Daniels, O. Farkas, J. B. Foresman, J. V. Ortiz, J. Cioslowski, D. J. Fox, *Gaussian 09, Revision E.01*, Gaussian Inc., Wallingford CT, **2013**.

[5] F. Neese, *Wiley Interdiscip. Rev. Comput. Mol. Sci.* **2022**, e1606.

[6] S. Grimme, F. Bohle, A. Hansen, P. Pracht, S. Spicher, M. Stahn, *J. Phys. Chem. A* **2021**, *125*, 4039–4054.

[7] P. Pracht, F. Bohle, S. Grimme, *Phys. Chem. Chem. Phys.* **2020**, *22*, 7169–7192.

[8] J. P. Perdew, K. Burke, M. Ernzerhof, *Phys. Rev. Lett.* **1996**, *77*, 3865–3868.

[9] J. P. Perdew, K. Burke, M. Ernzerhof, *Phys. Rev. Lett.* **1997**, *78*, 1396–1396.

[10] C. Adamo, V. Barone, *J. Chem. Phys.* **1999**, *110*, 6158–6170.

[11] S. Grimme, J. Antony, S. Ehrlich, H. Krieg, *J. Chem. Phys.* **2010**, *132*, 154104.

[12] S. Grimme, S. Ehrlich, L. Goerigk, *J. Comput. Chem.* **2011**, *32*, 1456–1465.

[13] F. Weigend, R. Ahlrichs, *Phys. Chem. Chem. Phys.* **2005**, *7*, 3297.

[14] F. Weigend, *Phys. Chem. Chem. Phys.* **2006**, *8*, 1057.

[15] F. London, *J. Phys. le Radium* **1937**, *8*, 397–409.

[16] R. McWeeny, *Phys. Rev.* **1962**, *126*, 1028–1034.

[17] R. Ditchfield, *Mol. Phys.* **1974**, *27*, 789–807.

[18] K. Wolinski, J. F. Hinton, P. Pulay, *J. Am. Chem. Soc.* **1990**, *112*, 8251–8260.

[19] J. R. Cheeseman, G. W. Trucks, T. A. Keith, M. J. Frisch, *J. Chem. Phys.* **1996**, *104*, 5497–5509.

[20] A. Hellweg, C. Hättig, S. Höfener, W. Klopper, *Theor. Chem. Acc.* **2007**, *117*, 587–597.

[21] C. J. Jameson, A. De Dios, A. Keith Jameson, *Chem. Phys. Lett.* **1990**, *167*, 575–582.

[22] C. van Wüllen, *Phys. Chem. Chem. Phys.* **2000**, *2*, 2137–2144.

[23] W. Deng, J. R. Cheeseman, M. J. Frisch, *J. Chem. Theory Comput.* **2006**, *2*, 1028–1037.

[24] C. Riplinger, F. Neese, *J. Chem. Phys.* **2013**, *138*, 034106.

[25] D. G. Liakos, Y. Guo, F. Neese, *J. Phys. Chem. A* **2020**, *124*, 90–100.

[26] D. G. Liakos, M. Sparta, M. K. Kesharwani, J. M. L. L. Martin, F. Neese, *J. Chem. Theory Comput.* **2015**, *11*, 1525–1539.

[27] C. Riplinger, P. Pinski, U. Becker, E. F. Valeev, F. Neese, *J. Chem. Phys.* **2016**, *144*, 024109.

[28] C. J. Cramer, *Essentials of Computational Chemistry: Theories and Models*, John Wiley & Sons, Ltd, Chichester, UK, **2004**.

[29] G. Mills, H. Jónsson, G. K. Schenter, *Surf. Sci.* **1995**, *324*, 305–337.

[30] H. Jónsson, G. Mills, K. W. Jacobsen, in *Class. Quantum Dyn. Condens. Phase Simulations*, WORLD SCIENTIFIC, **1998**, pp. 385–404.

[31] G. Henkelman, H. Jónsson, *J. Chem. Phys.* **2000**, *113*, 9978–9985.

[32] G. Henkelman, B. P. Uberuaga, H. Jónsson, *J. Chem. Phys.* **2000**, *113*, 9901–9904.

[33] E. Maras, O. Trushin, A. Stukowski, T. Ala-Nissila, H. Jónsson, *Comput. Phys. Commun.* **2016**, *205*, 13–21.

[34] V. Ásgeirsson, B. O. Birgisson, R. Bjornsson, U. Becker, F. Neese, C. Riplinger, H. Jónsson, *J. Chem. Theory Comput.* **2021**, *17*, 4929–4945.